https://doi.org/10.5194/egusphere-2026-2949
Preprint. Discussion started: 15 September 2026

TAlkEaSy: the Total Alkalinity Earth System Model v1.0 for exploring climate, redox and ocean chemistry over geologic time

Xiyuan Chen[1] & Timothy M. Lenton[1]

[1]Global Systems Institute and Geography Department, University of Exeter, Exeter, EX4 4QE, United Kingdom

Correspondence to: Xiyuan Chen (xc342@exeter.ac.uk) and Timothy M. Lenton (T.M.Lenton@exeter.ac.uk)

Abstract. Here, we present the TAlkEaSy (Total Alkalinity Earth System) model, a framework for exploring the coupling of changes in the major ion balance of the ocean, biogeochemical cycling and global temperature and for testing hypotheses against proxy records. The model incorporates: (1) dynamic biogeochemical cycles of major ions (Ca, Mg, S, Na, K, Cl) and C, O and nutrients (N, P); (2) a complete alkalinity system with major ions and dissolved inorganic carbon (DIC) species; (3) novel proxies of Mg, Ca and U stable isotopes, together with C, S and Sr isotopes. The motivation for developing TAlkEaSy was that few existing models incorporate complete biogeochemical cycles of carbon, oxygen, nutrient, and ocean major ions with carbonate chemistry, and they either rely on data-driven approaches, or have problems accurately predicting major ion concentrations over geologic time. This impedes mechanistic understanding of the interactions between Earth's climate, redox and ocean chemistry. TAlkEaSy is an extension of the COPSE model. We present the model configuration of TAlkEaSy and the functional forms, feedbacks, and parameterization of the biogeochemical processes included. The responses of TAlkEaSy to an idealised pulse injection of CO_2 or a step increase in degassing are evaluated, to differentiate the responses to abrupt perturbation and slower changes in forcing.

1 Introduction

Understanding the controls on climate, redox and ocean chemistry over Earth history is a critical part of understanding the co-evolution of life and the planet. They have been the target for biogeochemical box modelling for nearly half a century (Garrels and Lerman, 1981). This is motivated by proxy data and data-derived reconstructions of climate, redox and ocean chemistry over the Phanerozoic, which suggest significant variations relative to the present day. To summarise: atmospheric CO_2, related to global temperature, is characterized by a "double-hump"—with high values in the early Paleozoic and again in the Mesozoic (Foster et al., 2017; Witkowski et al., 2018). Atmospheric O_2, which is both a product of photosynthetic life and a constraint on aerobic life, increased markedly in the mid-Paleozoic with a corresponding oxygenation of the deep ocean (Lenton et al. 2016), and likely exhibited two subsequent peaks in the Carboniferous-Permian and the Cretaceous (Mills et al., 2023). Ocean major ion chemistry shows variations between 'calcite' and 'aragonite' seas, with secular variations in seawater concentrations of Ca ($[Ca^{2+}]_{sw}$), Mg ($[Mg^{2+}]_{sw}$), their ratio ($[Mg/Ca]_{sw}$) and S ($[SO_4^{2-}]_{sw}$) reconstructed from halite fluid inclusions (FI): $[Ca^{2+}]_{sw}$ shows two peaks in the mid-Paleozoic and Mesozoic and one trough in the Permian characterized by a "M" shape,

https://doi.org/10.5194/egusphere-2026-2949
Preprint. Discussion started: 15 September 2026

while $[Mg^{2+}]_{sw}$, $[Mg/Ca]_{sw}$ and $[SO_4^{2-}]_{sw}$ are the opposite "W" shape (Turchyn and DePaolo, 2019; Blättler, 2025). Going further back into the Precambrian world, largely model-based reconstructions of CO_2, O_2, major ion concentrations (also including Na ($[Na^+]_{sw}$), K ($[K^+]_{sw}$) and Cl ($[Cl^-]_{sw}$)) and ocean carbonate chemistry (including pH and DIC concentrations) suggest even larger variations from present day conditions (Halevy and Bachan, 2017; Krissansen-Totton et al., 2018; Guo and Korenaga, 2025). Biogeochemical cycles of carbon, oxygen, nutrient and ocean major ions are coupled (Fig. 1). The CO_2 level determines the thermodynamics of continental weathering rate and the input of nutrients, cations and anions into the ocean (Fig. 1). The O_2 level depends on both organic matter production and preservation, affected by carbon and sulphur cycles (Fig. 1). Ocean major ions of Mg, Ca, S, Na, K and Cl, with different biogeochemical cycles and residence times, together contribute to ocean total alkalinity concentration ($[TAlk]_{sw}$) to maintain charge balance (Fig. 1).

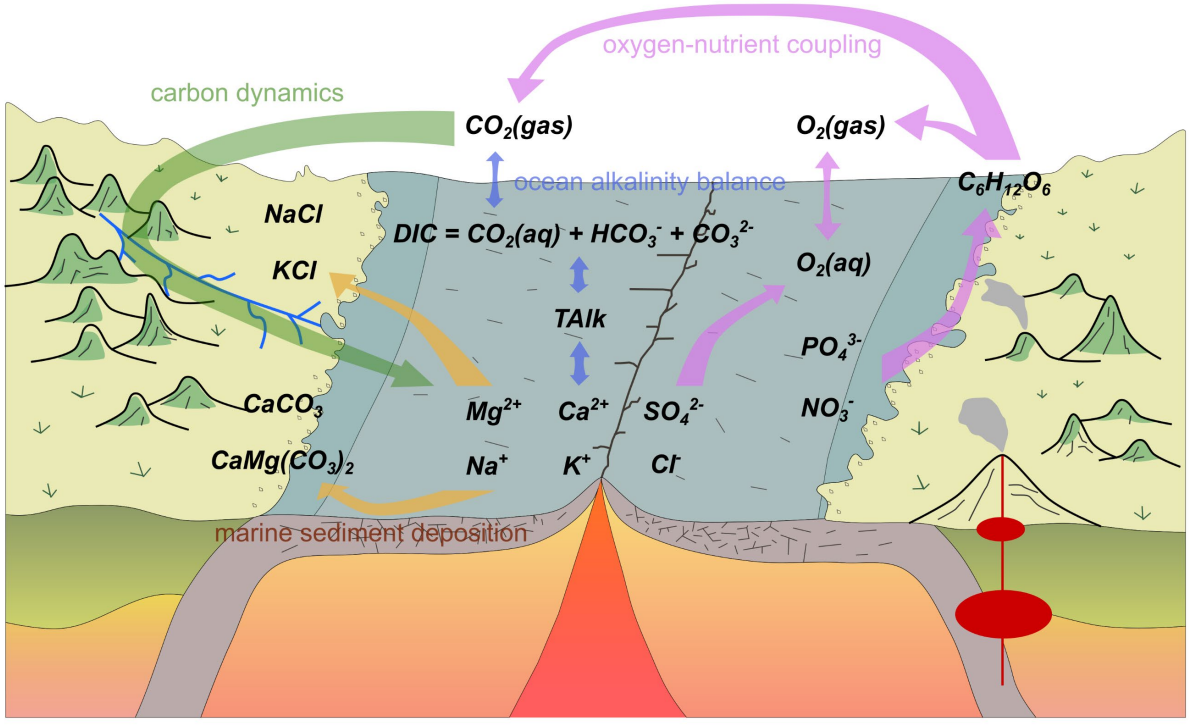

Figure 1: Global biogeochemical cycles of carbon, oxygen, nutrient, ocean major ions and alkalinity system.

To gain a quantitative, process-based understanding of variations in these variables over geologic time, a range of biogeochemical models have been developed, which are briefly reviewed in Section 1.1. In short, these models have tackled different subsets of variables with different approaches. These include inverse modelling approaches which use some data as inputs to predict other variables, and forwards modelling approaches that seek to predict variations in proxy data as a means of testing the model assumptions and associated mechanistic hypotheses. There has also been some development from minimal

https://doi.org/10.5194/egusphere-2026-2949
Preprint. Discussion started: 15 September 2026

box models to more complex spatially resolved models, especially to better capture climate and its effects on weathering processes, and to capture variation in ocean processes particularly between the deep ocean and shelf seas. Yet no model has given a convincing reconstruction of all the variables noted above when compared to available proxy data. Tackling some variables independently of others can, of course, be mechanistically justified. However, recent literature has highlighted previously underappreciated connections between ocean major ion chemistry and associated total alkalinity, and redox processes and overall Earth surface redox balance (Fakhraee et al., 2025; Evans et al., 2026). Meanwhile, existing models demonstrate that there is significant coupling between redox balance, involving oxygen, organic carbon and sulphur cycles, and long-term inorganic carbon cycling and climate (Bergman et al., 2004; Arvidson et al., 2006; Lenton et al., 2018; Maffre et al., 2025). This provides a key motivation for developing TAlkEaSy as an extension of the COPSE (Carbon, Oxygen, Phosphorus, Sulphur Evolution) model (Bergman et al., 2004; Lenton et al., 2018).

1.1 Review of previous models of long-term biogeochemical cycling

Over the last 45 years a range of models of long-term biogeochemical cycling have been developed, evolving from an initial focus on the carbon (C) cycle, to studying the oxygen (O) cycle, and ocean major ions and carbonate chemistry (Kemeny et al., 2025). Here we summarise them following this development history (Table 1).

The first models of the long-term carbon cycle used prescribed carbon ($\delta^{13}C$) and sulphur ($\delta^{34}S$) isotope data, in a data-driven approach termed inverse modelling, to calculate global carbon and sulphur reservoirs changes and related fluxes (Garrels and Lerman, 1981, 1984). The later GEOCARB model continued this inverse approach utilising $\delta^{13}C$ data (Berner, 1991, 1994; Berner and Kothavala, 2001). Other, subsequent models have taken a forwards modelling approach—having the model predict proxy data as a means of testing and refining its process-based representation. Some have incorporated more element cycles, feedback mechanisms and/or spatial resolution. An example of increased spatial resolution is the LOSCAR model (Table 1), which incorporates 1-dimensional sediment column and ocean grids to help evaluate the influence of diagenetic processes on the global carbon cycle (Zeebe, 2012a). Ca and Si processes have been added to LOSCAR (Komar and Zeebe, 2011, 2016; Isson and Planavsky, 2018), but the model does not incorporate a complete representation of ocean major ion systems. Some other works make long timescale predictions of carbon and pH, but without a complete alkalinity system (Krissansen-Totton et al., 2018).

A different strand of biogeochemical box models consider the organic carbon cycle and atmospheric O_2 over the Phanerozoic, by combining C, O and S cycles together, initially using the inverse, data-driven approach (Kump and Garrels, 1986; Berner, 1987; Kump, 1989). A logical next step was to couple models of the inorganic and organic carbon cycles to consider the coupled evolution of atmospheric CO_2 and O_2. This started with the COPSE model (Bergman et al., 2004), which also pioneered a forward modelling approach, coupling models of P, N and O_2 cycles (Lenton and Watson, 2000a, 2000b) with GEOCARB's representation of the inorganic carbon cycle. COPSE predicted CO_2, O_2, $[Ca^{2+}]_{sw}$, $[SO_4^{2-}]_{sw}$, $\delta^{13}C$ and $\delta^{34}S$ (Bergman et al., 2004) but did not include other major ions. COPSE has been used to explore the effects of seafloor and terrestrial weathering (Mills et al., 2014a, 2014b), land plant colonization (Lenton et al., 2016), dissolved organic carbon (DOC)

https://doi.org/10.5194/egusphere-2026-2949
Preprint. Discussion started: 15 September 2026

reservoir oxidation (Shields et al., 2019), and bifurcations in biogeochemical cycles (Handoh and Lenton, 2003; Li et al., 2025, 2026). However, the difficulty of predicting $[Ca^{2+}]_{sw}$ without other major cations led to prescribing $[Ca^{2+}]_{sw}$ in the updated model (Lenton et al., 2018). Meanwhile, GEOCARBSULF coupled the CO_2 and O_2 cycles in an inverse data-driven approach prescribing $\delta^{13}C$ and $\delta^{34}S$ (Berner, 2006a, 2006b, 2009; Royer et al., 2014). The GEOCARBSULFOR model adopts elements of COPSE and removes the prescription of $\delta^{34}S$ (Krause et al., 2018, 2022).

A spatially-resolved modelling approach began with GEOCLIM (Donnadieu et al., 2004; Arndt et al., 2011; Goddéris et al., 2014, 2017), which includes C, O, P, and N cycles and interpolates general circulation model (GCM) output of temperature and runoff in different palaeographic configurations at different CO_2 levels to drive a 2-dimensional model of the land surface and weathering processes (Donnadieu et al., 2004; Arndt et al., 2011; Goddéris et al., 2014, 2017). The SCION model combines the COPSE and GEOCLIM models to evaluate the effects of changing continental configuration and paleogeography, and global plant biomass (Mills et al., 2021, 2025; Gurung et al., 2022; Merdith et al., 2025). Meanwhile, ocean spatial resolution has been introduced in the CANOPS model (1-dimensional ocean) (Ozaki et al., 2011, 2022), which includes cycles of C, O, N, P, S and the CH_4 system, and has been applied to the Precambrian (Ozaki et al., 2019). The GENIE model, characterized by a 3-dimensional ocean grid framework, incorporates C, O and P in the initial version (Ridgwell et al., 2007), and then adds Fe and S and diagenetic modules (van de Velde et al., 2021). Although some GENIE versions include Ca and its isotopes, the Ca isotopic system works as a passive proxy for tracing ocean acidification and diagenesis (Fantle and Ridgwell, 2020; Adloff et al., 2021). The recently introduced EONS model, incorporating 1-D ocean column(s), simulates C, O, N, P cycling over the past 4 billion years, emphasizing the roles of the biosphere (Horne and Goldblatt, 2024). Other models combine equations and feedbacks from some of the above models to predict global CO_2 and O_2 states, with additional variables like Fe^{2+}, Fe^{3+}, H_2S (Alcott et al., 2019, 2022; Zhao et al., 2023, 2024; Zhong et al., 2025).

The modelling of ocean major ion cycles, began with the BLAG model, incorporating C, Ca and Mg cycles and predicting CO_2, global mean surface temperature (GMST), $[Mg^{2+}]_{sw}$ and $[Ca^{2+}]_{sw}$ (Berner et al., 1983). A version of the GEOCARB model included ocean Ca, Mg and S cycling, emphasizing the effects of sulfuric acid weathering on $[Mg^{2+}]_{sw}$, $[Ca^{2+}]_{sw}$ and $[SO_4^{2-}]_{sw}$ over the Phanerozoic (Berner, 2004). Other models focusing on ocean major ions choose to input drivers like CO_2 and temperature to calculate crucial fluxes like continental weathering (Hardie, 1996; Demicco et al., 2005). Some models incorporate novel proxies like stable Ca ($\delta^{44}Ca$) and Mg ($\delta^{26}Mg$) isotopes, to constrain global Ca and Mg fluxes (Farkaš et al., 2007; Higgins and Schrag, 2015). Recently, some models have sought to simulate ocean major ion cycles and pH evolution over Earth history (Halevy and Bachan, 2017; Guo and Korenaga, 2025), but they lack the organic O, S and nutrient cycles.

Models coupling C, O and ocean major ion cycles with carbonate chemistry are rare. In previous models, either complete ocean major ion cycles are lacking, or the nutrient cycle is lacking (Lasaga et al., 1985; Hansen and Wallmann, 2003; Bergman et al., 2004; Maffre et al., 2025). The only previous model which incorporates C, O, nutrient, ocean major ion cycles and carbonate chemistry is MAGic (Arvidson et al., 2006, 2013). The MAGic model calculates marine carbonate burial flux using the record of $[Mg/Ca]_{sw}$ (Arvidson et al., 2006, 2013). This approach should necessarily provide a good fit to $[Ca^{2+}]_{sw}$

https://doi.org/10.5194/egusphere-2026-2949
Preprint. Discussion started: 15 September 2026

and $[Mg/Ca]_{sw}$ data. However, the predictions of $[Mg^{2+}]_{sw}$ and $[SO_4^{2-}]_{sw}$ fit data poorly (Arvidson et al., 2006, 2013; Kemeny et al., 2025). This suggests that MAGic has some weaknesses in its feedbacks, reactions or parameterizations at least for the Mg and S cycles.

Table 1: Review of biogeochemical models.

Model name	Biogeochemical cycle	Prescribed data	Main output	Reference
Works focusing on carbon cycle				
/	C, S	$\delta^{13}C$	reservoirs (C, S), $\delta^{34}S$	Garrels and Lerman, 1981
/	C, S	$\delta^{34}S$	reservoirs (C, S), $\delta^{13}C$	Garrels and Lerman, 1984
GEOCARB	C	$\delta^{13}C$	CO_2, GMST	Berner, 1991, 1994, 2001
LOSCAR	C, P	/	CO_2, $[TAlk]_{sw}$, $[DIC]_{sw}$, pH, CCD	Zeebe, 2012a
	C, Si	/	CO_2, $[TAlk]_{sw}$, $[DIC]_{sw}$, $[H_4SiO_4]_{sw}$, pH	Isson and Planavsky, 2018
/	C	/	CO_2, GMST, pH	Krissansen-Totton et al., 2018
Works focusing on carbon and oxygen cycles				
/	C, O, S	$\delta^{13}C$, $\delta^{34}S$	reservoirs (C, O, S)	Kump and Garrels, 1986
/	C, O, S	$\delta^{13}C$, $\delta^{34}S$	reservoirs (C, O, S)	Berner, 1987
/	C, O, S, Sr	$\delta^{13}C$, $\delta^{34}S$, $^{87}Sr/^{86}Sr$	reservoirs (C, O, S, Sr)	Kump, 1989
GEOCARBSULF	C, O, S	$\delta^{13}C$, $\delta^{34}S$, $^{87}Sr/^{86}Sr$	CO_2, GMST, O_2	Berner 2006a, 2006b
	C, O, S	GMST, $\delta^{13}C$, $\delta^{34}S$, $^{87}Sr/^{86}Sr$	CO_2, O_2	Royer et al., 2014
	C, O, S	$\delta^{13}C$, $\delta^{34}S$, $^{87}Sr/^{86}Sr$	CO_2, O_2	Zhang et al., 2018
COPSE	C, O, S, P, N, Sr	$[Ca^{2+}]_{sw}$	CO_2, GMST, O_2, $[NO_3^-]_{sw}$, $[PO_4^{3-}]_{sw}$, $[SO_4^{2-}]_{sw}$, $\delta^{13}C$, $\delta^{34}S$, $^{87}Sr/^{86}Sr$	Mills et al., 2017; Lenton et al., 2018; Shields et al., 2019; Tostevin and Mills, 2020
GEOCARBSULFOR	C, O, S, P, N, Sr	$[Ca^{2+}]_{sw}$, $\delta^{13}C$	CO_2, GMST, O_2, $[NO_3^-]_{sw}$, $[PO_4^{3-}]_{sw}$, $[SO_4^{2-}]_{sw}$, $\delta^{34}S$, $^{87}Sr/^{86}Sr$	Krause et al., 2018; 2022; 2024
GEOCLIM	C, O, P, N, S	/	CO_2, O_2, GMST, $[NO_3^-]_{sw}$, $[PO_4^{3-}]_{sw}$, $[SO_4^{2-}]_{sw}$, $[TAlk]_{sw}$, $[DIC]_{sw}$, pH	Arndt et al., 2011;
	C, O, P, N, S, Sr	/	CO_2, O_2, GMST, $[NO_3^-]_{sw}$, $[PO_4^{3-}]_{sw}$, $[SO_4^{2-}]_{sw}$, $[TAlk]_{sw}$, $[DIC]_{sw}$, pH, $\delta^{13}C$, $^{87}Sr/^{86}Sr$	Goddéris et al., 2014, 2017;
SCION	C, O, P, N, S, Sr	$[Ca^{2+}]_{sw}$	CO_2, GMST, O_2, $[NO_3^-]_{sw}$, $[PO_4^{3-}]_{sw}$, $[SO_4^{2-}]_{sw}$, $\delta^{13}C$, $\delta^{34}S$, $^{87}Sr/^{86}Sr$	Mills et al., 2021; 2025; Merdith et al., 2025
CANOPS	C, O, P, N, S	$[Ca^{2+}]_{sw}$	CO_2, GMST, O_2, $[NO_3^-]_{sw}$, $[PO_4^{3-}]_{sw}$, $[SO_4^{2-}]_{sw}$,	Ozaki et al., 2022
GENIE	C, O, P	/	CO_2, GMST, O_2, $[PO_4^{3-}]_{sw}$, $[TAlk]_{sw}$, $[DIC]_{sw}$, pH, $\delta^{13}C$	Ridgwell et al., 2007; Holden et al., 2013
	C, O, P, S, Fe	/	CO_2, GMST, O_2, $[PO_4^{3-}]_{sw}$, $[SO_4^{2-}]_{sw}$, $[H_2S]_{sw}$, $[Fe^{2+}]_{sw}$, $[Fe^{3+}]_{sw}$, $[TAlk]_{sw}$, $[DIC]_{sw}$, pH, $\delta^{13}C$, $\delta^{34}S$, $\delta^{56}Fe$	van de Velde et al., 2021
EONS	C, O, P, N	/	CO_2, GMST, O_2, $[NO_3^-]_{sw}$, $[PO_4^{3-}]_{sw}$, $[TAlk]_{sw}$, $[DIC]_{sw}$, pH	Horne and Goldblatt, 2024
/	C, O, P	/	CO_2, GMST, O_2, $[PO_4^{3-}]_{sw}$, $\delta^{13}C$	Alcott et al., 2019; 2022
/	C, O, P, S, Fe	/	CO_2, GMST, O_2, $[PO_4^{3-}]_{sw}$, $[SO_4^{2-}]_{sw}$, $[H_2S]_{sw}$, $[Fe^{2+}]_{sw}$, $[Fe^{3+}]_{sw}$, $\delta^{13}C$	Zhao et al., 2023, 2024; Zhong et al., 2025
Works focusing on ocean major ions and chemistry				
BLAG	C, Ca, Mg	/	CO_2, GMST, $[Mg^{2+}]_{sw}$, $[Ca^{2+}]_{sw}$, pH	Berner et al., 1983
GEOCARB	C, Ca, Mg, S	$\delta^{13}C$	$[Mg^{2+}]_{sw}$, $[Ca^{2+}]_{sw}$, $[SO_4^{2-}]_{sw}$	Berner, 2004
LOSCAR	C, Ca	/	CO_2, $[Ca^{2+}]_{sw}$, $[TAlk]_{sw}$, $[DIC]_{sw}$, $\delta^{13}C$, $\delta^{44}Ca$	Komar and Zeebe, 2016
/	C, Ca, Sr	/	CO_2, GMST, $[Ca^{2+}]_{sw}$, pH, $\delta^{13}C$, $^{87}Sr/^{86}Sr$	Wallmann, 2001
/	Ca, Mg, S, Na, K	CO_2	$[Mg^{2+}]_{sw}$, $[Ca^{2+}]_{sw}$, $[Na^+]_{sw}$, $[K^+]_{sw}$, $[SO_4^{2-}]_{sw}$	Demicco et al., 2005
/	C, Ca, Mg	CO_2, $[Mg/Ca]_{sw}$, $\delta^{44}Ca$, $^{87}Sr/^{86}Sr$,	$[Mg^{2+}]_{sw}$, $[Ca^{2+}]_{sw}$, $[DIC]_{sw}$, pH, $\delta^{44}Ca$,	Farkaš et al., 2007
/	C, Mg, Ca	/	CO_2, $[Mg^{2+}]_{sw}$, $[Ca^{2+}]_{sw}$, $\delta^{26}Mg$	Higgins and Schrag, 2015

https://doi.org/10.5194/egusphere-2026-2949
Preprint. Discussion started: 15 September 2026

/	C, Mg, Na, K, Cl	CO_2, $[SO_4^{2-}]_{sw}$,	$[Mg^{2+}]_{sw}$, $[Ca^{2+}]_{sw}$, $[Na^+]_{sw}$, $[K^+]_{sw}$, $[Cl^-]_{sw}$, $[TAlk]_{sw}$, $[DIC]_{sw}$, pH	Halevy and Bachan, 2017
/	C, Mg, Na,	$[K^+]_{sw}$, $[SO_4^{2-}]_{sw}$, $[Cl^-]_{sw}$,	CO_2, GMST, $[Mg^{2+}]_{sw}$, $[Ca^{2+}]_{sw}$, $[Na^+]_{sw}$, $[Fe^{2+}]_{sw}$, $[DIC]_{sw}$, pH	Guo and Korenaga, 2025
Works focusing on carbon, oxygen, ocean major ions and chemistry				
LABEGA	C, O, Ca, Mg, S	$\delta^{13}C$, $\delta^{34}S$	CO_2, GMST, O_2, $[Mg^{2+}]_{sw}$, $[Ca^{2+}]_{sw}$, pH	Lasaga et al., 1985
/	C, O, Ca, Mg, S, Sr	$\delta^{13}C$, $\delta^{34}S$, $^{87}Sr/^{86}Sr$	CO_2, GMST, O_2, $[Mg^{2+}]_{sw}$, $[Ca^{2+}]_{sw}$, $[SO_4^{2-}]_{sw}$	Hansen and Wallmann, 2003
COPSE	C, O, S, P, N, Ca	/	CO_2, GMST, O_2, $[NO_3^-]_{sw}$, $[PO_4^{3-}]_{sw}$, $[Ca^{2+}]_{sw}$, $[SO_4^{2-}]_{sw}$, $\delta^{13}C$, $\delta^{34}S$	Bergman et al., 2004
MAGic	C, O, N, P, Ca, Mg, S, Na, K, Cl	$[Mg/Ca]_{sw}$	CO_2, O_2, $[NO_3^-]_{sw}$, $[PO_4^{3-}]_{sw}$, $[Mg^{2+}]_{sw}$, $[Ca^{2+}]_{sw}$, $[Na^+]_{sw}$, $[K^+]_{sw}$, $[SO_4^{2-}]_{sw}$, $[Cl^-]_{sw}$	Arvidson et al., 2006; 2013
GEOCLIM	C, O, P, Ca, Sr	/	CO_2, O_2, $[PO_4^{3-}]_{sw}$, $[Ca^{2+}]_{sw}$, $\delta^{13}C$, $^{87}Sr/^{86}Sr$	Maffre et al., 2025
TAlkEaSy	C, O, N, P, Mg, Ca, Na, K, S, Cl, Sr, U	/	CO_2, O_2, $[NO_3^-]_{sw}$, $[PO_4^{3-}]_{sw}$, $[Mg^{2+}]_{sw}$, $[Ca^{2+}]_{sw}$, $[Na^+]_{sw}$, $[K^+]_{sw}$, $[SO_4^{2-}]_{sw}$, $[Cl^-]_{sw}$, $\delta^{13}C$, $\delta^{34}S$, $^{87}Sr/^{86}Sr$, $\delta^{26}Mg$, $\delta^{44}Ca$, $\delta^{238}Mg$,	This model

1.2 Motivation and aims

This review of previous long-term biogeochemical models, reveals three aims that motivated the formulation of a new model: (i) coupling global carbon, oxygen, nutrient and ocean major ion cycles; (ii) incorporating both conservative cations and anions and DIC species contributions to ocean alkalinity balance and carbonate chemistry; (iii) updating the model proxy tracers, especially the novel stable isotopes and their dynamic fractionation mechanisms.

We started with COPSE as a foundation because it has complete C, O and nutrient cycles which have been adopted by others. The new TAlkEaSy (Total Alkalinity Earth System) model makes three key innovations: (1) it is the first forward biogeochemical model which incorporates dynamic cycles of C, O, P, N, Ca, Mg, S, Na, K, Cl; (2) it has a complete ocean alkalinity system with major ions and DIC species and dynamic marine carbonate burial equations; (3) it combines new isotopic systems of stable Ca, Mg, U and classic proxies of $\delta^{13}C$, $\delta^{34}S$, and $^{87}Sr/^{86}Sr$.

In the following, section 2 describes the TAlkEaSy model including the coding language and the numerical solver. Section 3 undertakes sensitivity tests of the TAlkEaSy model. Section 4 considers future development of the model. Section 5 summarizes.

2 Model description

2.1 Overview

In this section, the TAlkEaSy model is introduced in the following logic: (i) the geochemical reservoirs, processes, fluxes, isotopes and their naming rules in the model; (ii) applied forcings; (iii) biogeochemical cycles and the functional forms of their fluxes and feedbacks; (iv) the ocean alkalinity-carbonate chemistry systems. In the main text, we only introduce new and updated equations. Existing equations and parameters inherited from COPSE are listed in Appendix Table A1, A2 and A3.

https://doi.org/10.5194/egusphere-2026-2949
Preprint. Discussion started: 15 September 2026

2.2 Geochemical reservoirs, processes, fluxes and isotopes

2.2.1 Reservoirs

In TAlkEaSy model, the core biogeochemical reservoirs include atmospheric CO_2 (***CO₂***) and O_2 (***AO₂***), oceanic DIC (***DIC***), O_2 (***MO₂***), nitrogen (***N***), phosphorus (***P***), Ca (***Ca***), Mg (***Mg***), S (***S***), Na (***Na***), K (***K***), Cl (***Cl***), and with sedimentary rock reservoirs of organic carbon (***ORG***), carbonate (***CARB***), pyrite (***PYR***), gypsum (***GYP***), halite (***NaCl***), sylvite (***KCl***). As passive tracers, Sr and U have reservoirs in the TAlkEaSy model but they are not involved in the system dynamics. The Sr cycle has ocean Sr (***OSr***) and sedimentary Sr (***SSr***) reservoirs. The U cycle has an ocean U reservoir (***U***). All reservoirs are labelled by their abbreviation in italic bold style. Their initial details and initial modern values are summarized in Table 2.

Table 2: Biogeochemical reservoirs in TAlkEaSy model.

Reservoir	Label	Initial value	Isotope
Atmosphere CO_2	***CO₂***	4.96×10^{16} mol	$\delta^{13}C$ = -8.5 ‰
Atmosphere O_2	***AO₂***	3.67×10^{16} mol	/
Ocean DIC	***DIC***	2.72×10^{18} mol	$\delta^{13}C$ = 0.0 ‰
Ocean O_2	***MO2***	3.50×10^{17} mol	/
Ocean nitrogen	***N***	4.35×10^{16} mol	/
Ocean phosphorus	***P***	3.10×10^{15} mol	/
Ocean calcium	***Ca***	1.40×10^{19} mol	$\delta^{44}Ca$ = 1.89 ‰
Ocean magnesium	***Mg***	7.20×10^{19} mol	$\delta^{26}Mg$ = -0.82 ‰
Ocean sulphur	***S***	3.97×10^{19} mol	$\delta^{34}S$ = 20.0 ‰
Ocean sodium	***Na***	6.61×10^{20} mol	/
Ocean potassium	***K***	1.49×10^{19} mol	/
Ocean chlorine	***Cl***	7.69×10^{20} mol	/
*Ocean strontium	***OSr***	1.20×10^{17} mol	$^{87}Sr/^{86}Sr$ = 0.709
*Ocean uranium	***U***	1.90×10^{13} mol	$\delta^{238}U$ = -0.39 ‰
Sedimentary organic carbon	***ORG***	1.25×10^{21} mol	$\delta^{13}C$ = -27.0 ‰
Sedimentary carbonate	***CARB***	5.00×10^{21} mol	$\delta^{13}C$ = 1.0 ‰
Sedimentary pyrite	***PYR***	1.80×10^{20} mol	$\delta^{34}S$ = -15.0 ‰
Sedimentary gypsum	***GYP***	2.00×10^{20} mol	$\delta^{34}S$ = 20.0 ‰
Sedimentary halite	***NaCl***	1.83×10^{20} mol	/
Sedimentary sylvite	***KCl***	2.00×10^{18} mol	/
*Sedimentary strontium	***SSr***	5.00×10^{18} mol	$^{87}Sr/^{86}Sr$ = 0.708

*Passive tracers, not involved in TAlkEaSy model dynamics

https://doi.org/10.5194/egusphere-2026-2949
Preprint. Discussion started: 15 September 2026

2.2.2 Processes

All biogeochemical processes and related flux calculations are based on specific chemical reaction equations, listed in Table 3.

Table 3: Basic biogeochemical reaction equations in the TAlkEaSy model.

Reaction	Chemical equation
Granite/Basalt weathering	$(Ca^{2+}, Mg^{2+}, Na^{+}, K^{+})SiO_3 + 2 \cdot CO_2 + H_2O \rightarrow (Ca^{2+}, Mg^{2+}, Na^{+}, K^{+}) + 2 \cdot HCO_3^{-} + SiO_2$
Carbonate weathering	$(Ca^{2+}, Mg^{2+})SiO_3 + CO_2 + H_2O \rightarrow (Ca^{2+}, Mg^{2+}) + 2HCO_3^{-} + SiO_2$
Oxidative weathering	$C_6H_{12}O_6 + 6 \cdot O_2 \rightarrow 6 \cdot CO_2 + 6 \cdot H_2O$
Terrestrial organic matter burial	$6 \cdot CO_2 + 6 \cdot H_2O \rightarrow C_6H_{12}O_6 + 6 \cdot O_2$
Pyrite weathering	$4 \cdot FeS_2 + 15 \cdot O_2 + 8 \cdot H_2O \rightarrow 2 \cdot Fe_2O_3 + 8 \cdot H_2SO_4$
Gypsum weathering	$CaSO_4 \rightarrow Ca^{2+} + SO_4^{2-}$
NaCl weathering	$NaCl \rightarrow Na^{+} + Cl^{-}$
KCl weathering	$KCl \rightarrow K^{+} + Cl^{-}$
Marine carbonate burial	$Ca^{2+} + 2 \cdot HCO_3^{-} \rightarrow CaCO_3 + CO_2 + H_2O$
Marine organic carbon burial	$6 \cdot CO_2 + 6 \cdot H_2O \rightarrow C_6H_{12}O_6 + 6 \cdot O_2$
Marine pyrite burial	$2 \cdot Fe_2O_3 + 8 \cdot H_2SO_4 \rightarrow 4 \cdot FeS_2 + 15 \cdot O_2 + 8 \cdot H_2O$
Marine gypsum burial	$Ca^{2+} + SO_4^{2-} \rightarrow CaSO_4$
Marine NaCl burial	$Na^{+} + Cl^{-} \rightarrow NaCl$
Marine KCl burial	$K^{+} + Cl^{-} \rightarrow KCl$
Secondary dolomitization	$Mg^{2+} + CaCO_3 \rightarrow Ca^{2+} + CaMg(CO_3)_2$
Seafloor weathering	$CaSiO_3 + CO_2 \rightarrow CaCO_3 + SiO_2$ $MgSiO_3 + CO_2 + Ca^{2+} \rightarrow CaCO_3 + SiO_2 + Mg^{2+}$ $Mg^{2+} + CaSiO_3 \rightarrow Ca^{2+} + MgSiO_3$
High-/low-temperature hydrothermal	$2 \cdot Na^{+} + CaSiO_3 \rightarrow Ca^{2+} + Na_2SiO_3$ $2 \cdot Na^{+} + CaSiO_3 + 2 \cdot HCO_3^{-} \rightarrow CaCO_3 + Na_2SiO_3 + CO_2 + H_2O$
Reverse weathering	$(Na^{+}, K^{+}) + 2HCO_3^{-} + SiO_2 \rightarrow (Na^{+}, K^{+})SiO_3 + 2CO_2 + H_2O$
Na cation exchange processes	$Na^{+}_{water} \rightarrow Na^{+}_{clay}$
Organic carbon degassing	$C_6H_{12}O_6 + 6 \cdot O_2 \rightarrow 6 \cdot CO_2 + 6 \cdot H_2O$
Carbonate degassing	$CaCO_3 + SiO_2 \rightarrow CaSiO_3 + CO_2$
Pyrite degassing	$4 \cdot FeS_2 + 15 \cdot O_2 + 8 \cdot H_2O \rightarrow 2 \cdot Fe_2O_3 + 8 \cdot H_2SO_4$
Gypsum carbon degassing	$CaSO_4 + H_2O + SiO_2 \rightarrow CaSiO_3 + H_2SO_4$

https://doi.org/10.5194/egusphere-2026-2949
Preprint. Discussion started: 15 September 2026

2.2.3 Mass balance

Following mass-balance theory, the source and sink fluxes of a specific element are combined in a budget differential equation. We summarize all the element budget equations in Table 4. Their stoichiometric coefficients follow the chemical formulae in Table 3. One reaction can be related to several elements and we differentiate the element flux using subscript labels (Table 4).

160

Table 4: Reservoir budget differential equations in TAlkEaSy model

Reservoir	Budget differential equation
CO₂	$\frac{dCO_2}{dt} = cdeg_C - 2 \cdot silw_C - carbw_C + odeg_C + oxidw_C - lob_C - airsea_C$
AO₂	$\frac{dAO_2}{dt} = lob_O - odeg_O - oxidw_O - \frac{15}{8} \cdot (pyrw_O + pyrdeg_O) - airsea_O$
DIC	$\frac{dDIC}{dt} = 2 \cdot silw_C + 2 \cdot carbw_C - mcbTotal_C - sfw_C - hydhT_C - mob_C + airsea_C$
MO₂	$\frac{dMO_2}{dt} = mob_O + \frac{15}{8} \cdot mpb_O + airsea_O$
N	$\frac{dN}{dt} = nfix_N - denit_N - mob_N$
P	$\frac{dP}{dt} = psea_P - mob_P - fepb_P - capb_P - hydhT_P - hydlT_P$
Ca	$\frac{dCa}{dt} = silw_{Ca} + carbw_{Ca} + gypw_{Ca} + hydhT_{Ca} + hydlT_{Ca} + dolosec_{Ca} - mgb_{Ca} - mcbTotal_{Ca} - sfw_{Ca}$
Mg	$\frac{dMg}{dt} = silw_{Mg} + carbw_{Mg} + sfw_{Mg} - hydhT_{Mg} - hydlT_{Mg} - dolosec_{Mg}$
S	$\frac{dS}{dt} = pyrw_S + pyrdeg_S + gypw_S + gypdeg_S - mpb_S - mgb_S$
Na	$\frac{dNa}{dt} = silw_{Na} + NaClw_{Na} + Exb_{Na} - NaClb_{Na} - Exr_{Na} - Exd_{Na} - hydhT_{Na} - rw_{Na}$
K	$\frac{dK}{dt} = silw_K + KClw_K - KClb_K - hydhT_K - rw_K$
Cl	$\frac{dCl}{dt} = NaClw_{Cl} + KClw_{Cl} - NaClb_{Cl} - KClb_{Cl}$
ORG	$\frac{dORG}{dt} = mob_C + lob_C - odeg_C - oxidw_C$
CARB	$\frac{dCARB}{dt} = mcbTotal_C + sfw_C + hydhT_C - cdeg_C - carbw_C$
PYR	$\frac{dPYR}{dt} = mpb_S - pyrw_S - pyrdeg_S$
GYP	$\frac{dGYP}{dt} = mgb_S - gypw_S - gypdeg_S$
NaCl	$\frac{dNaCl}{dt} = NaClb_{(Na,Cl)} - NaClw_{(Na,Cl)}$
KCl	$\frac{dKCl}{dt} = KClb_{(K,Cl)} - KClw_{(K,Cl)}$
OSr	$\frac{dOSr}{dt} = silw_{Sr} + carbw_{Sr} + hydhT_{Sr} + hydlT_{Sr} - mcbTotal_{Sr} - sfw_{Sr}$

https://doi.org/10.5194/egusphere-2026-2949
Preprint. Discussion started: 15 September 2026

SSr	$\frac{dSSr}{dt} = mcbTotal_{Sr} - carbw_{Sr} - metam_{Sr}$
U	$\frac{dU}{dt} = silw_U - hydhT_U - hydlT_U - anoxic_U - other_U$

2.2.4 Fluxes

Some biogeochemical processes are involved in several elements' budget equations. In the TAlkEaSy model, we use process labels and add subscripts to denote the specific element being considered in a given flux. All the processes and their baseline flux values are listed in Table 5.

Table 5: Fluxes and their baseline values in TAlkEaSy model

Flux process	Label	Baseline values
Inorganic carbon cycle		10^{12} mol C yr^{-1}
Silicate weathering C	$silw_C$	12.50
Granite weathering C	$granw_C$	10.00
Basalt weathering C	$basw_C$	2.50
Carbonate weathering C	$carbw_C$	8.00
Carbonate degassing C	$cdeg_C$	14.40
Seafloor weathering C	sfw_C	3.00
High-temperature hydrothermal C	$hydhT_C$	0.94
Marine carbonate total burial C	$mcbTotal_C$	18.46
Organic carbon cycle		10^{12} mol C yr^{-1}
Oxidative weathering C	$oxidw_C$	3.75
Land organic burial C	$lobw_C$	2.50
Marine organic burial C	mob_C	2.50
Organic matter degassing C	$odeg_C$	1.25
Nitrogen cycle		10^{12} mol N yr^{-1}
Nitrogen fixation N	$nfix_N$	8.67
Denitrification N	$denit_N$	8.60
Marine organic burial N	mob_C	0.07
Phosphorus cycle		10^{9} mol P yr^{-1}
Reactive weathering P	$phosw_P$	42.50
Land organic burial P	$pland_P$	2.50
Reactive weathering to ocean P	$psea_P$	40.00
Marine organic burial P	mob_P	10.00
Iron-sorbed burial P	$fepb_P$	10.00
Ca-bound burial P	$capb_P$	10.00
High-temperature hydrothermal P	$hydhT_P$	4.00

https://doi.org/10.5194/egusphere-2026-2949
Preprint. Discussion started: 15 September 2026

Low-temperature hydrothermal P	$hydlT_P$	6.00
Magnesium cycle		10^{11} mol Mg yr^{-1}
Silicate weathering Mg	$silw_{Mg}$	33.75
Granite weathering Mg	$granw_{Mg}$	25.00
Basalt weathering Mg	$basw_{Mg}$	8.75
Carbonate weathering Mg	$carbw_{Mg}$	32.00
High-temperature hydrothermal Mg	$hydhT_{Mg}$	14.25
Low-temperature hydrothermal Mg	$hydlT_{Mg}$	29.50
Seafloor weathering Mg	sfw_{Mg}	10.00
Calcium cycle		10^{11} mol Ca yr^{-1}
Silicate weathering Ca	$silw_{Ca}$	75.85
Granite weathering Ca	$granw_{Ca}$	60.10
Basalt weathering Ca	$basw_{Ca}$	15.75
Carbonate weathering Ca	$carbw_{Ca}$	48.00
Gypsum weathering Ca	$gypw_{Ca}$	20.00
High-temperature hydrothermal Ca	$hydhT_{Ca}$	14.25
Low-temperature hydrothermal Ca	$hydlT_{Ca}$	29.50
Secondary dolomitization Ca	$dolosec_{Ca}$	32.00
Seafloor weathering Ca	sfw_{Ca}	10.00
Marine gypsum Ca	mgb_{Ca}	25.00
Marine carbonate total burial Ca	$mcbTotal_{Ca}$	184.60
Sulphur-pyrite-gypsum cycle		10^{12} mol S yr^{-1}
Pyrite weathering S	$pyrw_S$	0.45
Pyrite degassing S	$pyrdeg_S$	0.25
Gypsum weathering S	$gypw_S$	2.00
Gypsum degassing S	$gypdeg_S$	0.50
Marine pyrite burial S	mpb_S	0.70
Marine gypsum burial S	mgb_S	2.50
Sodium cycle		10^{12} mol Na yr^{-1}
Silicate weathering Na	$silw_{Na}$	2.08
Granite weathering Na	$granw_{Na}$	2.00
Basalt weathering Na	$basw_{Na}$	0.08
NaCl weathering Na	$NaClw_{Na}$	1.00
High-temperature hydrothermal Na	$hydhT_{Na}$	1.08
Marine NaCl burial Na	$NaClb_{Na}$	1.00
Reverse weathering Na	rw_{Na}	1.00
Sediment boundary layer exchange Na	Exb_{Na}	5.00
Riverine exchange Na	Exr_{Na}	1.00
Deep sea exchange Na	Exd_{Na}	4.00
Potassium cycle		10^{12} mol K yr^{-1}

https://doi.org/10.5194/egusphere-2026-2949
Preprint. Discussion started: 15 September 2026

Silicate weathering K	$silw_K$	1.00
Granite weathering K	$granw_K$	0.98
Basalt weathering K	$basw_K$	0.02
KCl weathering K	$KClw_K$	0.05
Marine KCl burial K	$KClb_K$	0.05
Reverse weathering K	rw_K	0.20
High-temperature hydrothermal K	$hydhT_{Na}$	0.80
Chlorine cycle		10^{12} mol Cl yr^{-1}
NaCl weathering Cl	$NaClw_{Cl}$	1.00
KCl weathering Cl	$KClw_{Cl}$	0.05
Marine NaCl burial Cl	$NaClb_{Cl}$	1.00
Marine KCl burial Cl	$KClb_{Cl}$	0.05
Strontium cycle		10^{9} mol Sr yr^{-1}
Silicate weathering Sr	$silw_{Sr}$	18.50
Granite weathering Sr	$granw_{Sr}$	14.50
Basalt weathering Sr	$basw_{Sr}$	4.00
Carbonate weathering Sr	$carbw_{Sr}$	16.00
High-temperature hydrothermal Sr	$hydhT_{Sr}$	1.00
Low-temperature hydrothermal Sr	$hydlT_{Sr}$	5.00
Marine carbonate total burial Sr	$mcbTotal_{Sr}$	36.00
Seafloor weathering Sr	sfw_{Sr}	4.50
Sediment metamorphism Sr	$metam_{Sr}$	20.00
Uranium cycle		10^{6} mol U yr^{-1}
Silicate weathering U	$silw_U$	50.00
Granite weathering U	$granw_U$	40.00
Basalt weathering U	$basw_U$	10.00
Anoxic sink burial U	$anoxic_U$	6.00
Other sink burial U	$other_U$	34.00
High-temperature hydrothermal U	$hydhT_U$	3.00
Low-temperature hydrothermal U	$hydlT_U$	7.00

2.2.5 Isotopes

Geochemical isotopic systems can help to trace environmental conditions and mechanisms of key processes. TAlkEaSy includes stable carbon, sulphur, magnesium, calcium and uranium isotopic systems and the radioactive strontium isotope system. We summarize calculation equations, standard samples and abbreviations of all isotopic systems in Table 6. The isotopic budget equations and parameterizations for C and S are mostly inherited from the COPSE model (Lenton et al., 2018). Here, we list the new and updated equations of Mg, Ca, U and Sr in Table 7. Their related values and fractionation factors are described in section 2.4.

https://doi.org/10.5194/egusphere-2026-2949
Preprint. Discussion started: 15 September 2026

Table 6: Isotopic systems in the TAlkEaSy model

Isotopic element	Calculation equation	Standard sample	TAlkEaSy abbreviation
Stable C	$\delta^{13/12}C = \left[\left({}^{13_C}/_{12_C}\right)_{sample} / \left({}^{13_C}/_{12_C}\right)_{standard} - 1\right] \times 1000$	V-CDB	$\delta^{13}C$
Stable S	$\delta^{34/32}S = \left[\left({}^{34_S}/_{32_S}\right)_{sample} / \left({}^{34_S}/_{32_S}\right)_{standard} - 1\right] \times 1000$	V-CDT	$\delta^{34}S$
Stable Mg	$\delta^{26/24}Mg = \left[\left({}^{26_{Mg}}/_{24_{Mg}}\right)_{sample} / \left({}^{26_{Mg}}/_{24_{Mg}}\right)_{standard} - 1\right] \times 1000$	DSM-3	$\delta^{26}Mg$
Stable Ca	$\delta^{44/40}Ca = \left[\left({}^{44_{Ca}}/_{40_{Ca}}\right)_{sample} / \left({}^{44_{Ca}}/_{40_{Ca}}\right)_{standard} - 1\right] \times 1000$	NIST-SRM915a	$\delta^{44}Ca$
Stable U	$\delta^{238/235}U = \left[\left({}^{238_U}/_{235_U}\right)_{sample} / \left({}^{238_U}/_{235_U}\right)_{standard} - 1\right] \times 1000$	CRM-112A	$\delta^{238}U$
Radioactive Sr	${}^{87_{Sr}}/_{86_{Sr}} = \left[\left({}^{87_{Sr}}/_{86_{Sr}}\right)_{sample} / \left({}^{87_{Sr}}/_{86_{Sr}}\right)_{standard} - 1\right] \times 1000$	NIST-987	${}^{87}Sr/{}^{86}Sr$

Table 7: Isotopic budget equations of Mg, Ca and U in the TAlkEaSy model

Element	Isotopic budget equations
Mg	$\frac{d(Mg \cdot \delta^{26}Mg_{sw})}{dt} = granw_{Mg} \cdot \delta^{26}Mg_{granw} + basw_{Mg} \cdot \delta^{26}Mg_{basw} + carbw_{Mg} \cdot \delta^{26}Mg_{carbw} + sfw_{Mg} \cdot \delta^{26}Mg_{sfw} - hydhT_{Mg} \cdot (\delta^{26}Mg_{sw} + \Delta^{26}Mg_{hydhT-sw}) - hydlT_{Mg} \cdot (\delta^{26}Mg_{sw} + \Delta^{26}Mg_{hydlT-sw}) - dolosec_{Mg} \cdot (\delta^{26}Mg_{sw} + \Delta^{26}Mg_{dolosec-sw})$
Ca	$\frac{d(Ca \cdot \delta^{44}Ca_{sw})}{dt} = granw_{Ca} \cdot \delta^{44}Ca_{granw} + basw_{Ca} \cdot \delta^{44}Ca_{basw} + carbw_{Ca} \cdot \delta^{44}Ca_{carbw} + gypw_{Ca} \cdot \delta^{44}Ca_{gypw} + hydhT_{Ca} \cdot \delta^{44}Ca_{hydhT} + hydlT_{Ca} \cdot \delta^{44}Ca_{hydlT} + dolosec_{Ca} \cdot \delta^{44}Ca_{dolosec} - mgb_{Ca} \cdot (\delta^{44}Ca_{sw} + \Delta^{44}Ca_{mgb-sw}) - sfw_{Ca} \cdot (\delta^{44}Ca_{sw} + \Delta^{44}Ca_{sfw-sw}) - mcbPelagic_{Ca} \cdot (\delta^{44}Ca_{sw} + \Delta^{44}Ca_{mcbPelagic-sw}) - Shelfarag_{Ca} \cdot (\delta^{44}Ca_{sw} + \Delta^{44}Ca_{Shelfarag-sw}) - Shelfcalc_{Ca} \cdot (\delta^{44}Ca_{sw} + \Delta^{44}Ca_{Shelfcalc-sw})$
Sr	$\frac{d(Sr \cdot {}^{87}Sr/{}^{86}Sr_{sw})}{dt} = granw_{Sr} \cdot {}^{87}Sr/{}^{86}Sr_{granw} + basw_{Sr} \cdot {}^{87}Sr/{}^{86}Sr_{basw} + carbw_{Sr} \cdot {}^{87}Sr/{}^{86}Sr_{carbw} + hydhT_{Sr} \cdot {}^{87}Sr/{}^{86}Sr_{hydhT} + hydlT_{U} \cdot {}^{87}Sr/{}^{86}Sr_{hydlT} - mcbTotal_{Sr} \cdot {}^{87}Sr/{}^{86}Sr_{mcbTotal} - sfw_{Sr} \cdot {}^{87}Sr/{}^{86}Sr_{sfw} - metam_{Sr} \cdot {}^{87}Sr/{}^{86}Sr_{metam}$
U	$\frac{d(U \cdot \delta^{238}U_{sw})}{dt} = granw_{U} \cdot \delta^{238}U_{granw} + basw_{U} \cdot \delta^{238}U_{basw} + carbw_{U} \cdot \delta^{238}U_{carbw} - hydhT_{U} \cdot \delta^{238}hydhT_{U} - hydlT_{U} \cdot \delta^{238}hydlT_{U} - Anoxic_{U} \cdot (\delta^{238}U_{sw} + \Delta^{238}U_{Anoxic-sw}) - Other_{U} \cdot (\delta^{238}U_{sw} + \Delta^{238}U_{Other-sw})$

2.3 Forcing factors

Most forcing factors in the TAlkEaSy model are inherited from the COPSE model (Lenton et al. 2018), and are derived from independent geophysical and geochemical data or based on some hypotheses (Berner, 1994, 2006b; Bartdorff et al., 2008; Mills et al., 2014a, 2017; Royer et al., 2014; Lenton et al., 2016, 2018). New forcings are carbonate exposed and flooded areas, which are estimated and applied in a separate study (Chen et al., 2026). We summarize all forcing factors in Table 7.

Table 7: Nondimensional normalized forcing factors in the TAlkEaSy model

Label	Description	Reference
DEGASS	Degassing from metamorphic and subduction intensity	Mills et al., 2017
UPLIFT	Tectonic uplift	Berner, 2006b
PG	Paleogeography effect on runoff/weathering	Royer et al., 2014
EVO	Land plant evolution and colonization	Lenton et al., 2018
W	Land plant effect in enhancing weathering	Lenton et al., 2018

https://doi.org/10.5194/egusphere-2026-2949
Preprint. Discussion started: 15 September 2026

COAL	Coal deposition area	Bartdorff et al., 2008
CP_{land}	Ratio of carbon to phosphorus in buried terrestrial plant material	Lenton et al., 2018
$P_{selective}$	Selective enhancement of phosphorus weathering by biology	Lenton et al., 2016
PELAGIC	Ocean pelagic calcification	Berner, 1994
$\alpha_{gran,exposed}$	Granite exposed area	Mills et al., 2014a
$\alpha_{bas,exposed}$	Basalt exposed area	Mills et al., 2014a
$\alpha_{carb,exposed}$	Carbonate exposed area	Chen et al., 2026
$\alpha_{carb,flooded}$	Carbonate flooded area	Chen et al., 2026

2.4 Core biogeochemical cycles

Core biogeochemical cycles are those involved in long-term Earth system dynamics. In TAlkEaSy, they include C, O, N, P, S, Mg, Ca, Na, K and Cl. Next, we describe the processes involved in each cycle, providing equations where they are additional to or altered from the COPSE model (Lenton et al., 2018). The modern baseline values of each flux are represented by a comma and '0'.

2.4.1 Carbon

Global carbon reservoirs are divided into ***DIC***, ***CO_2***, ***ORG*** and ***CARB***. In TAlkEaSy, we split the atmosphere-ocean carbon reservoir into ***DIC*** and ***CO_2*** because this is helpful for future extension to dimensional atmospheric and oceanic grids. The separated ***DIC*** and ***CO_2*** reservoirs are connected by air-sea exchange. The related air-sea exchange equations and parameters are founded in the Henry's law and described in Appendix Table A1 and A3.

The incorporation of ocean major ion cycles adds or changes some functional forms in the global carbon cycle processes. We first illustrate inorganic C processes and then organic C.

In the inorganic C cycle, carbonate degassing ($cdeg_C$) provides the input of atmospheric CO_2, the level of which is regulated by silicate weathering ($silw_C$) over 1 million years timescales. In TAlkEaSy, $cdeg_C$ is promoted by *DEGASS*, *PELAGIC* and sedimentary carbonate reservoir size as in COPSE (Table A1) (Lenton et al., 2018). $silw_C$ is composed of granite ($granw_C$) and basalt weathering ($basw_C$) (Eq. (1)) (Mills et al., 2014a).

$$silw_{(C,Mg,Ca,Na,K,Sr,U)} = granw_{(C,Mg,Ca,Na,K,Sr,U)} + basw_{(C,Mg,Ca,Na,K,Sr,U)} \quad (1)$$

The controls on $granw_C$ and $basw_C$ are as in the COPSE model, which captures the influence of *UPLIFT*, *PG*, exposed areas and environmental factors including the effects of temperature, runoff and land plant vegetation on weathering rates (Eq. (2)-(3); Table A2) (Mills et al., 2014a; Lenton et al., 2018). The functional equations of $silw_C$, $granw_C$ and $basw_C$, are also applied to the elements Mg, Ca, Na, K, Sr and U (Eq. (2)-(3)), as they belong to the same biogeochemical process:

$$granw_{(C,Mg,Ca,Na,K,Sr,U)} = granw_{(C,Mg,Ca,Na,K,Sr,U)},0 \cdot UPLIFT \cdot PG \cdot f_{Tgran} \cdot f_{runoff} \cdot f_{biota} \cdot \alpha_{gran,exposed} \quad (2)$$

https://doi.org/10.5194/egusphere-2026-2949
Preprint. Discussion started: 15 September 2026

$$basw_{(\mathrm{C,Mg,Ca,Na,K,Sr,U})} = basw_{(\mathrm{C,Mg,Ca,Na,K,Sr,U})},0 \cdot PG \cdot f_{Tbas} \cdot f_{runoff} \cdot f_{biota} \cdot \alpha_{bas,exposed} \quad (3)$$

Carbonate weathering ($carbw_{\mathrm{C}}$) is similar to COPSE considering the effects from *UPLIFT*, *PG* and environmental affecting factors (Eq. (4); Table A2) but is updated by applying the forcing of carbonate exposed area ($\alpha_{carb,exposed}$), rather than the reservoir size. This update is reasonable as exposed area determines how much can be weathered of the underlying reservoir. The Eq. (4) is also applicable to Mg, Ca and Sr.

$$carbw_{(\mathrm{C,Mg,Ca,Sr})} = carbw_{(\mathrm{C,Mg,Ca,Sr})},0 \cdot UPLIFT \cdot PG \cdot g_{runoff} \cdot f_{biota} \cdot \alpha_{carb,exposed} \quad (4)$$

Seafloor weathering is crucial in the removal of carbon in ocean crust alteration and its functional form follows COPSE considering the influence of *DEGASS* and temperature kinetics ((Eq. (5)) (Mills et al., 2014b, 2021). Previous works and COPSE just consider the carbon flux by assuming the seafloor rock is Ca-silicate mineral and the product all precipitates as $CaCO_3$ (Mills et al., 2014b, 2021; Lenton et al., 2018). However, seafloor rock is rich in Mg^{2+} which cannot form carbonate directly and needs Ca^{2+} for compensation (Table 3) (Ligi et al., 2013). In all, seafloor weathering is a source of C and Ca but a sink for Mg.

$$sfw_{(\mathrm{C,Mg,Ca,Sr})} = sfw_{(\mathrm{C,Mg,Ca,Sr})},0 \cdot DEGASS \cdot e^{k_T^{sfw} \cdot \Delta T} \quad (5)$$

where $e^{k_T^{sfw}}$ is the kinetic temperature constant corresponding to the activation energy of the reaction around 0.0608, inherited from COPSE (Lenton et al., 2018). ΔT is the temperature relative to the modern global mean surface temperature (GMST) around 15°C (Appendix Table A2).

Recent works suggest that high-temperature hydrothermal processes (Lafay et al., 2017), also known as seawater-basalt reactions, are an important C sink. The MAGic model links the process to $[Na^+]_{sw}$ and $[K^+]_{sw}$ (Table 3) (Arvidson et al., 2006). In TAlkEaSy, the high-temperature hydrothermal C flux is calculated based on the corresponding Na and K fluxes according to their stoichiometries (Eq. (6)).

$$hydhT_{\mathrm{C}} = \frac{1}{2} \cdot (hydhT_{\mathrm{Na}} + hydhT_{\mathrm{K}}) \quad (6)$$

Different from some previous long timescale models, the calculation of marine total carbonate burial flux ($mcbTotal_{\mathrm{C}}$) in TAlkEaSy is based on ocean carbonate saturation state (Ω) (Eq. (7)) (Shields and Mills, 2021; Zhao et al., 2023), rather than the sum of silicate and carbonate weathering (Bergman et al., 2004; Lenton et al., 2018; Tostevin and Mills, 2020):

$$mcbTotal_{(\mathrm{C,Ca})} = mcbTotal_{(\mathrm{C,Ca})},0 \cdot \frac{(\Omega - 1.0)^{\eta}}{\Omega,0} \quad (7)$$

where η is the order of the reaction and ~1.7 is suggested from a previous model (Shields and Mills, 2021; Zhao et al., 2023). $\Omega,0$ is the present-day ocean average carbonate saturation state of around 3.0 (Shields and Mills, 2021; Zhao et al., 2023).

The organic C cycle in TAlkEaSy is identical to COPSE (Lenton et al., 2018) and includes the processes of organic carbon degassing ($odeg_{\mathrm{C}}$), oxidative weathering ($oxidw_{\mathrm{C}}$), land (lob_{C}) and marine organic burial (mob_{C}). There are two

https://doi.org/10.5194/egusphere-2026-2949
Preprint. Discussion started: 15 September 2026

updated equations. First, oxidative weathering is updated to be dependent on the isolated atmosphere oxygen normalized reservoir rather than the integrated atmosphere-ocean oxygen reservoir (Eq. (8)).

$$oxidw_{(C,O)} = oxidw_{(C,O),0} \cdot UPLIFT \cdot \frac{\boldsymbol{ORG}}{\boldsymbol{ORG,0}} \cdot \left(\frac{\boldsymbol{AO_2}}{\boldsymbol{AO_2,0}}\right)^{0.5} \quad (8)$$

The other updated equation is the feedback equation to evaluate global vegetation net primary productivity – the OCT (O_2, CO_2, temperature) feedback equation (Table A2) (Lenton et al., 2018). The expression of O_2 is updated to depend on isolated atmosphere oxygen normalized reservoir (Eq. (9)).

$$V_{npp}(O_2) = 1.5 - 0.5 \cdot \left(\frac{\boldsymbol{AO_2}}{\boldsymbol{AO_2,0}}\right) \quad (9)$$

2.4.2 Oxygen

The global oxygen cycle includes the organic C and pyrite cycles. In TAlkEaSy, there are two updates compared to the original COPSE: (i) changing of the stoichiometry between pyrite and oxygen; (ii) splitting of the atmosphere O_2 and ocean O_2 reservoirs. Regarding the first update, COPSE assumes the stoichiometric coefficient ratio between O_2 and reductive S in related pyrite reactions is 2.0 (Bergman et al., 2004; Lenton et al., 2018; Tostevin and Mills, 2020; Mills et al., 2021), but this implies that some other ion like H^+ is needed to maintain charge balance. To maintain alkalinity conservation, we use the precise stoichiometric coefficient of 15/8 in TAlkEaSy (Table 4). About the second update, the separated atmosphere and ocean O_2 reservoirs are connected by air-sea exchange. The related air-sea exchange O_2 flux equations are following the Henry's law and described in Appendix Table A1 and A3.

Besides, the isolation of atmosphere O_2 and ocean O_2 reservoirs changes some variable functional forms. The atmosphere O_2 pressure ($pO_2(atm)$), used to be calculated by an empirical equation in COPSE, is directly determined by atmospheric O_2 size in TAlkEaSy (Eq. (10)):

$$pO_2(atm) = \frac{\boldsymbol{AO_2}}{moles1atm} \quad (10)$$

where $moles1atm$ is the constant of total atmospheric gas moles for 1 atm and is set to be 1.77×10^{20} mol in TAlkEaSy.

This leads to a change in the equation describing wildfire feedback of O_2 on land vegetation ($ignit$) (Eq. (11)):

$$ignit = \min\left(\max(48 \cdot pO_2(atm) - 9.08, 0), 5\right) \quad (11)$$

There is also a change to the equation for anoxic fraction of the ocean ($ANOX$). We keep similar form of that as COPSE but update it by linking it to ocean O_2 normalized size ((Eq. (12)).

$$ANOX = \frac{1}{1+e^{-k_{anox} \cdot (k_u - \frac{newp}{newp,0} - \frac{\boldsymbol{MO_2}}{\boldsymbol{MO_2,0}})}} \quad (12)$$

https://doi.org/10.5194/egusphere-2026-2949
Preprint. Discussion started: 15 September 2026

where k_{anox} and k_u are constant controlling the sharpness of ocean anoxia and they are the same values as COPSE about 12.0 and 0.5, respectively (Lenton et al., 2018).

2.4.3 Nitrogen

The budget of ***N*** is inherited from COPSE. For ***N*** cycle, its main source is nitrogen fixation ($nfix_{\mathrm{N}}$) and its sinks are denitrification ($denit_{\mathrm{N}}$) and marine organic matter burial (mob_{N}). The functional forms of $nfix_{\mathrm{N}}$, $denit_{\mathrm{N}}$ and mob_{N} are the same as COPSE and are listed in Appendix Table A1 (Lenton et al., 2018).

2.4.4 Phosphorus

In TAlkEaSy, following COPSE, the total continental weathering phosphorus flux ($phosw_{\mathrm{P}}$) has contributions from silicate ($silw_{\mathrm{P}}$), carbonate ($carbw_{\mathrm{P}}$) and oxidative ($oxidw_{\mathrm{P}}$) weathering fluxes, and a fraction of it is buried in land vegetation ($pland_{\mathrm{P}}$) (Appendix Table A1) (Bergman et al., 2004; Lenton et al., 2018). Oceanic phosphorus fluxes include the input from continental weathering into the sea ($psea_{\mathrm{P}}$), marine organic burial (mob_{P}), iron-sorbed P burial ($fepb_{\mathrm{P}}$) and calcium-bound P burial ($capb_{\mathrm{P}}$), which are taken from COPSE (Appendix Table A1) (Bergman et al., 2004; Lenton et al., 2018). Two new ocean P sink fluxes are incorporated in TAlkEaSy—high-temperature ($hydhT_{\mathrm{P}}$) and low-temperature hydrothermal phosphorus removal ($hydlT_{\mathrm{P}}$) (Sharoni and Halevy, 2023). $hydhT_{\mathrm{P}}$ is promoted by MOR expansion, approximated by *DEGASS*, and depends on ocean phosphorus normalized reservoir (Eq. (13)):

$$hydhT_{\mathrm{P}} = hydhT_{\mathrm{P},0} \cdot DEGASS \cdot \frac{\boldsymbol{P}}{\boldsymbol{P_{,0}}} \tag{13}$$

Phosphate concentrations in ridge-flanks decline with temperature (Fisher and Wheat, 2010). Here, we assume that phosphorus removal has an approximate linear relationship with the ridge-flank temperature (Fisher and Wheat, 2010). The ridge-flank temperature is 9.0 ℃ higher than the ocean surface temperature according to previous models (Higgins and Schrag, 2015). In TAlkEaSy, the equation of $hydlT_{\mathrm{P}}$ captures the ridge-flank temperature change and ocean phosphorus normalized reservoir (Eq. (14)):

$$hydlT_{\mathrm{P}} = hydlT_{\mathrm{P},0} \cdot \frac{GMST(℃)+9.0}{GMST(℃),0+9.0} \cdot \frac{\boldsymbol{P}}{\boldsymbol{P_{,0}}} \cdot \tag{14}$$

where $GMST(℃)$ is the global mean surface temperature in the unit of ℃ and its equation is listed in Appendix Table A2.

2.4.5 Sulphur

The sulphur system in TAlkEaSy includes an ocean sulphur cycle and sedimentary pyrite and gypsum cycles (Table 4). There are three updates in TAlkEaSy compared to COPSE.

First, we update the equation of marine pyrite burial to include changes in the ocean dissolved O_2 reservoir (Eq. (15)), rather than the integrated atmosphere-ocean O_2 reservoir in COPSE (Lenton et al., 2018).

https://doi.org/10.5194/egusphere-2026-2949
Preprint. Discussion started: 15 September 2026

$$mpb_{(S,O)} = mpb_{(S,O),0} \cdot \frac{mob_C}{mob_{C,0}} \cdot \frac{S}{S,0} \cdot \frac{MO_2,0}{MO_2}, \quad (15)$$

Second, we update the temperature dependency of gypsum runoff (Eq. (16)):

$$gypw_{(S,Ca)} = gypw_{(S,Ca),0} \cdot UPLIFT \cdot PG \cdot \frac{GYP}{GYP,0} \cdot gypsum_{runoff} \cdot f_{biota}, \quad (16)$$

where $gypsum_{runoff}$ is the updated temperature-dependent runoff equation. In COSPE this is the same as for carbonate (Lenton et al., 2018). Here, we apply the value of activation energy for gypsum dissolution, reported to be 41.84 kJ mol^{-1} (Liu and Nancollas, 1971), and derive it following an Arrhenius equation (Mills et al., 2014; Lenton et al., 2018) (Eq. (17)):

$$gypsum_{runoff} = 1 + 0.0606 \cdot \Delta T \quad (17)$$

Third, marine gypsum burial is linked to $[Ca^{2+}]_{sw}$ and its dynamic cycle, rather than using a prescribed concentration (Eq. (18)):

$$mgb_{(S,Ca)} = mgb_{(S,Ca),0} \cdot \frac{Ca}{Ca,0} \cdot \frac{S}{S,0} \quad (18)$$

Other sulphur flux functional forms are the same as COPSE (Appendix Table A1) (Lenton et al., 2018).

2.4.6 Magnesium

The Mg cycle and its budget fluxes have been treated in very different ways over the last thirty years (Fig. 2) (Shalev et al., 2019). Oceanic Mg fluxes include silicate ($silw_{Mg}$) and carbonate weathering ($carbw_{Mg}$), and seafloor weathering (sfw_{Mg}) as sources, and high- ($hydhT_{Mg}$) and low-temperature ($hydlT_{Mg}$) hydrothermal processes, and secondary dolomitization ($dolosec_{Mg}$) as sinks (Table 4).

The functional forms of $silw_{Mg}$, $granw_{Mg}$, $basw_{Mg}$ and $carbw_{Mg}$ are the same as in Eq. (1)-(4). Since basalt is abundant in Mg-rich mafic rocks whereas granite comprises Mg-poor felsic rocks, separating granite and basalt weathering helps to differentiate the lithology contributions in specific geological time intervals. Regarding their δ^{26}Mg compositions, research suggests no noteworthy difference of δ^{26}Mg between granite and basalt, which are around -0.25 ‰ (Teng, 2017). For carbonate δ^{26}Mg we use the reported value of around -2.00 ‰ as in previous research (Higgins and Schrag, 2015; Xia et al., 2024). With our parameterization of $silw_{Mg}$, $granw_{Mg}$, $basw_{Mg}$ and $carbw_{Mg}$ and their isotopes, the mean δ^{26}Mg of riverine is around -1.10 ‰ which is the same as present day observations (Tipper, 2021).

Since few models incorporate complete C, Mg and Ca systems, previous works about seafloor weathering focus on its contribution to the global C cycle. Recently, it has been assumed that the behaviour of Mg in seafloor weathering could be approximated as $hydlT_{Mg}$ (Coogan et al., 2025). However, $hydhT_{Mg}$, $hydlT_{Mg}$ and sfw_{Mg} are different processes. For sfw_{Mg}, its geochemical reactant is Mg-silicate minerals (Ligi et al., 2013), its reaction zones are the ocean floor and its feedbacks should follow the land-like thermodynamic sensitivity rules (Fig. 2) (Eq. (5)) (Mills et al., 2014a, 2014b). sfw_{Mg}

https://doi.org/10.5194/egusphere-2026-2949
Preprint. Discussion started: 15 September 2026

releases Mg^{2+}, compensated by Ca^{2+} to form carbonate precipitation, providing a source of ocean ***Mg*** and a sink for ***Ca*** (Ligi et al., 2013). Regarding the $\delta^{26}Mg$ of sfw_{Mg}, there is a big uncertainty in altered oceanic basalt $\delta^{26}Mg$, ranging from -2.76 to 0.21 ‰ reported by previous research (Teng, 2017). Therefore, we choose to a middle value around -1.10 ‰ to approximate the $\delta^{26}Mg$ of sfw_{Mg}.

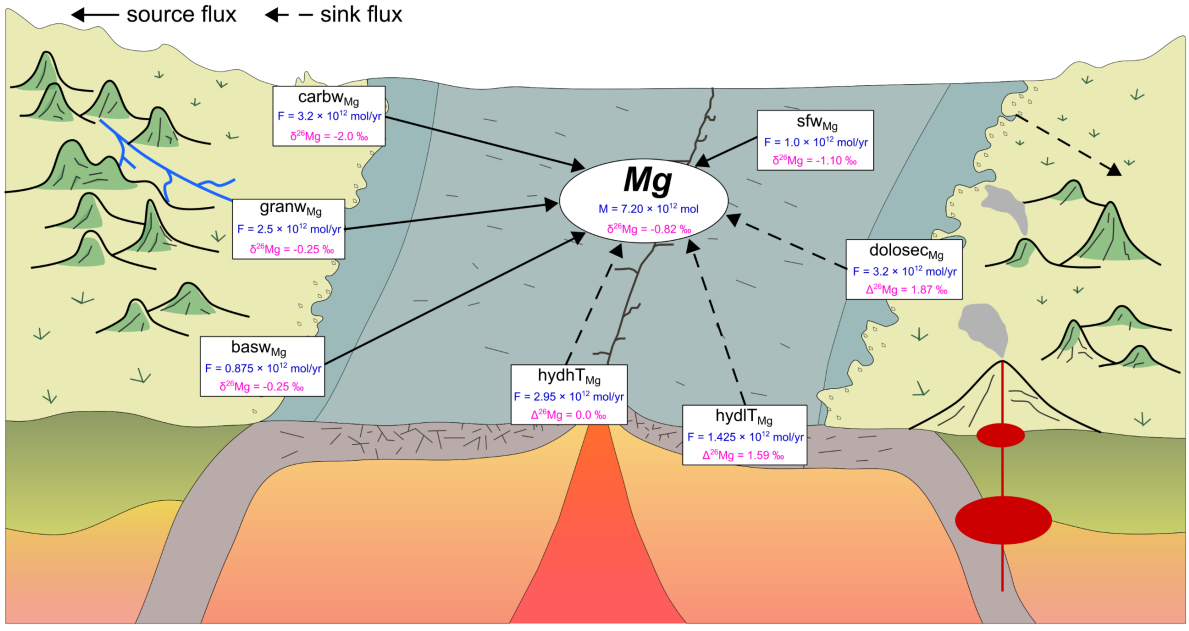

Figure 2: Ocean Mg biogeochemical cycle and isotopic budget.

Hydrothermal processes are important Mg sinks in previous models (Shalev et al., 2019). However, recent works suggest that they not only happen in different zones but are also characterized by different affecting factors, functional forms and $\delta^{26}Mg$ fractionations (Higgins and Schrag, 2015). For the high-temperature hydrothermal process, it is suggested to be driven by MOR expansion approximated by *DEGASS* and $[Mg^{2+}]_{sw}$ (Eq. (19)) (Berner, 2004; Holland, 2005; Ligi et al., 2013):

$$hydhT_{(Mg,Ca)} = hydhT_{\mathrm{Mg}},0 \cdot DEGASS \cdot \frac{\boldsymbol{Mg}}{\boldsymbol{Mg,0}} \quad (19)$$

The $\delta^{26}Mg$ fractionation factor between high-temperature hydrothermal and seawater ($\Delta^{26}Mg_{\mathrm{hydhT-sw}}$) is taken to be 0 ‰ (Eq. (20)) (Higgins and Schrag, 2015; Shalev et al., 2019).

$$\Delta^{26}Mg_{\mathrm{hydhT-sw}} = \delta^{26}Mg_{hydhT} - \delta^{26}Mg_{sw} \quad (20)$$

Low-temperature hydrothermal processing occurs in off-axis regions and its reactant is seawater Mg^{2+} (Shalev et al., 2019). Different from sfw_{Mg} and $hydlT_{\mathrm{Mg}}$, the flux of $hydlT_{\mathrm{Mg}}$ has been suggested to have a near-linear relationship with the ridge-

https://doi.org/10.5194/egusphere-2026-2949
Preprint. Discussion started: 15 September 2026

flank temperature in the range around 20 °C to 60 °C (Fisher and Wheat, 2010; Higgins and Schrag, 2015; Shalev et al., 2019). In TAlkEaSy, the functional form of $hydlT_{\mathrm{Mg}}$ captures the effects of $[Mg^{2+}]_{sw}$ and temperature, assuming ridge-flank temperature 9 °C higher than ocean surface and GMST (Eq. (21)).

$$hydlT_{(Mg,Ca)} = hydlT_{\mathrm{Mg}},0 \cdot \frac{GMST(℃)+9.0}{GMST(℃),0+9.0} \cdot \frac{\boldsymbol{Mg}}{\boldsymbol{Mg,0}}. \quad (21)$$

During the process of $hydlT_{\mathrm{Mg}}$, δ^{26}Mg fractionation is temperature-dependent (Shalev et al., 2019). Here, we adopt the suggested Mg isotopic fractionation equation (Eq. (22)):

$$\Delta^{26}Mg_{hydlT-sw} = 2.71 \cdot \frac{1}{GMST(℃)+9.0+273.15} \cdot 10^3 - 7.81 \quad (22)$$

Whether from Mg budget balance calculation (Holland, 2005; Shalev et al., 2019; Xia et al., 2024) or theoretical atomistic simulations (Kim et al., 2023), secondary dolomitization ($dolosec_{\mathrm{Mg}}$) is inferred to be an important sink in the ocean ***Mg*** budget. In previous models, the diagenetic process $dolosec_{\mathrm{Mg}}$ is affected by geography and carbonate deposition flux (Holland 2005; Halevy and Bachan, 2017; Guo and Korenaga, 2025). However, there are a couple of issues: (1) if $dolosec_{\mathrm{Mg}}$ only depends on marine carbonate burial flux this means that secondary dolomitization only happens to newly precipitated carbonate, but if older carbonate were flooded, dolomitization might happen; (2) the relationship to local environmental state changes like pH and saturation state may be nonlinear but is typically simplified to be linear in previous models. We capture the effects of $[Mg^{2+}]_{sw}$ and the local environmental changes—the forcing of carbonate flooded area with a nonlinear relationship to evaluate $dolosec_{\mathrm{Mg}}$ as Eq. (23).

$$dolosec_{(Mg,Ca)} = dolosec_{(\mathrm{Mg},Ca)} \cdot \frac{\boldsymbol{Mg}}{\boldsymbol{Mg,0}} \cdot \alpha_{carb,flooded}{}^{\beta_{dolosec}} \quad (23)$$

where $\beta_{dolosec}$ is set to be 2.0 in TAlkEaSy and will be discussed further in a separate paper.

The δ^{26}Mg fractionation during secondary dolomitization is reported to be affected by temperature (Li et al., 2015). In TAlkEaSy, we choose to apply the empirical formula linked to GMST (Eq. (24)).

$$\Delta^{26}Mg_{dolosec-sw} = -0.1554 \cdot 10^6 \cdot \frac{1}{(GMST(℃)+273.15)^{2.0}} \quad (24)$$

2.4.7 Calcium

The oceanic Ca cycle is the most complex among the cations because (i) it has input and output fluxes, with some characteristics of typical source-sink balance (Farkaš et al., 2007); (ii) it is indirectly affected by the cation exchange processes with Mg and marine gypsum burial with S (Bergman et al., 2004; Holland, 2005; Krause et al., 2024); (iii) it is controlled by marine carbonate burial which links to the carbon cycle via carbonate saturation state, but also compensates for alkalinity-charge imbalance and affects $[DIC]_{sw}$ and carbonate chemistry (Halevy and Bachan, 2017). In TAlkEaSy, we incorporate Ca biogeochemical processes including silicate weathering ($silw_{Ca}$), carbonate weathering ($carbw_{Ca}$), gypsum weathering

https://doi.org/10.5194/egusphere-2026-2949
Preprint. Discussion started: 15 September 2026

($gypw_{Ca}$), high- ($hydhT_{Ca}$) and low-temperature hydrothermal ($hydlT_{Ca}$) and secondary dolomitization ($dolosec_{Ca}$) as sources, and seafloor weathering (sfw_{Ca}), marine gypsum burial (mgb_{Ca}) and marine total carbonate burial ($mcbTotal_{Ca}$) as sink fluxes (Fig. 3) (Table 4).

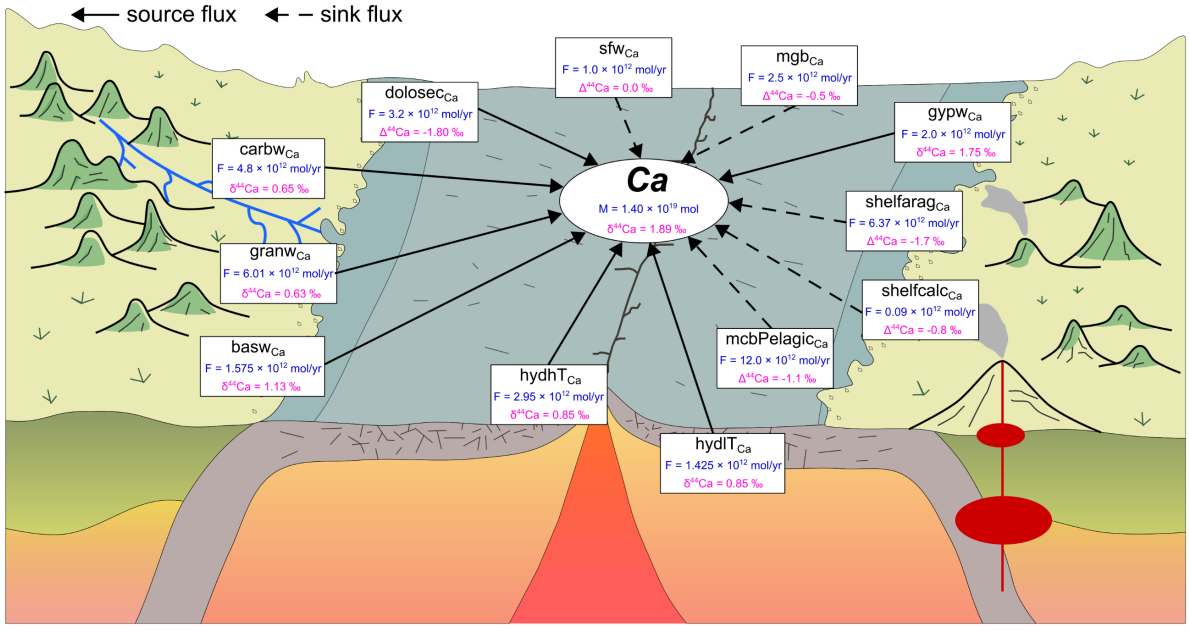

Figure 3: Ocean Ca biogeochemical cycle and isotopic budget.

For the land weathering Ca fluxes, the functional forms are as in Eq. (1)-(4) and Table A1. The $\delta^{44}Ca$ of granite and basalt differ based on data compilation (Antonelli and Simon, 2020). Accordingly, we set the $\delta^{44}Ca$ for $granw_{Ca}$ ($\delta^{44}Ca_{granw}$) and $basw_{Ca}$ ($\delta^{44}Ca_{basw}$) to be around 0.63 ‰, and 1.13 ‰, respectively (Antonelli and Simon, 2020). The weighted average value of $silw_{Ca}$ ($\delta^{44}Ca_{silw}$) is around 0.73 ‰, close to the $\delta^{44}Ca$ of upper continental crust (UCC) (Wang et al., 2019). The $\delta^{44}Ca$ for $carbw_{Ca}$ ($\delta^{44}Ca_{carbw}$) and $gypw_{Ca}$ ($\delta^{44}Ca_{gypw}$) are about 0.65 ‰, and 1.75 ‰, based on previous works (Farkaš et al., 2007; Fantle and Tipper, 2014; Gussone et al., 2020). Riverine $\delta^{44}Ca$ from mixing of $silw_{Ca}$, $carbw_{Ca}$ and $gypw_{Ca}$ is around 0.86 ‰, matching observed data (Fantle and Tipper, 2014).

The hydrothermal fluxes $hydhT_{Ca}$ and $hydlT_{Ca}$ are recognized to be important ocean Ca sources via exchange with Mg^{2+} (Berner, 2004; Holland, 2005; Higgins and Schrag, 2015) and their fluxes are set equal to $hydhT_{Mg}$ and $hydlT_{Mg}$ (Eq. (19), (21)). For the $\delta^{44}Ca$ of $hydhT_{Ca}$ ($\delta^{44}Ca_{hydhT}$) and $hydlT_{Ca}$ ($\delta^{44}Ca_{hydlT}$), we approximate them to be the composition of MORB, which is around 0.85 ‰ (Farkaš et al., 2007; Amini et al., 2008; Blättler et al., 2011).

https://doi.org/10.5194/egusphere-2026-2949
Preprint. Discussion started: 15 September 2026

The flux of $dolosec_{Ca}$ is equal to the Mg flux in the process (Eq. (23)) (Berner, 2004; Holland, 2005). For the Ca isotopic fractionation between $dolosec_{Ca}$ and seawater ($\Delta^{44}Ca_{dolosec-sw}$) (Eq. (25)), we adopt the value of -1.80 ‰ used in previous modelling works (Farkaš et al., 2007).

$$\Delta^{44}Ca_{dolosec-sw} = \delta^{44}Ca_{dolosec} - \delta^{44}Ca_{sw} \quad (25)$$

For sfw_{Ca}, we simplify the process to only involve Mg and Ca, although Na and K might make minor contributions. In TAlkEaSy, the flux of sfw_{Ca} is equal to sfw_{Mg} (Eq. (5)). The Ca isotopic fractionation factor of sfw_{Ca} ($\Delta^{44}Ca_{sfw-sw}$) is assumed to be 0 ‰ (Eq. (26)):

$$\Delta^{44}Ca_{sfw-sw} = \delta^{44}Ca_{sfw} - \delta^{44}Ca_{sw} \quad (26)$$

The marine gypsum burial Ca flux (mgb_{Ca}) is the same as the S flux based on stoichiometry (Table 3). Ca isotopic fractionation in marine gypsum precipitation is affected by precipitation rate, saturation state, and other factors (Harouaka et al., 2014; Gussone et al., 2016). We apply a Ca isotope fractionation factor between gypsum precipitation and seawater ($\Delta^{44}Ca_{mgb-sw}$) of -0.50 ‰ (Eq. (27)), as reported in laboratory experiments under the chemical equilibrium state (Harouaka et al., 2014).

$$\Delta^{44}Ca_{mgb-sw} = \delta^{44}Ca_{mgb} - \delta^{44}Ca_{sw} \quad (27)$$

Marine carbonate burial is the largest ocean Ca sink and is calculated based on the carbonate saturation state (Eq. (7)). The total marine carbonate burial flux ($mcbTotal_{Ca}$) is subdivided into marine pelagic ($mcbPelagic_{Ca}$) and shelf ($mcbShelf_{Ca}$) burial fluxes (Wallmann, 2001) (Eq. (28)):

$$mcbTotal_{Ca} = mcbPelagic_{Ca} + mcbShelf_{Ca} \quad (28)$$

The marine pelagic carbonate burial flux ($mcbPelagic_{Ca}$) has been promoted by pelagic calcification since the Mesozoic (Blättler et al., 2012). Thus, we link the *PELAGIC* forcing factor to $mcbPelagic_{Ca}$ (Eq. (29)):

$$mcbPelagic_{Ca} = mcbPelagic_{Ca},0 \cdot PELAGIC \quad (29)$$

The δ^{44}Ca fractionation between pelagic carbonate and seawater ($\Delta^{44}Ca_{mcbPelagic-sw}$) (Eq. (30)), uses a value of -1.10 ‰ which represents planktonic and benthonic foraminifera, coccolithophorids and echinoderms samples (Blättler et al., 2012).

$$\Delta^{44}Ca_{mcbPelagic-sw} = \delta^{44}Ca_{mcbPelagic} - \delta^{44}Ca_{sw} \quad (30)$$

Marine shelf carbonate burial ($mcbShelf_{Ca}$) is composed of aragonite ($shelfarag_{Ca}$) and calcite ($shelfcalc_{Ca}$) according to the mineralogy (Eq. (31)):

$$mcbShelf_{Ca} = shelfarag_{Ca} + shelfcalc_{Ca} \quad (31)$$

The burial fluxes of shelf aragonite ($shelfarag_{Ca}$) and calcite ($shelfcalc_{Ca}$) are affected by the seawater ratio of Mg to Ca (Stanley, 2006; Porter, 2007). Higher Mg:Ca ratio in the fluid can promote the precipitation of aragonite rather than calcite

https://doi.org/10.5194/egusphere-2026-2949
Preprint. Discussion started: 15 September 2026

because the nucleation barrier for calcite is higher than for aragonite (Sun et al., 2015). Furthermore, during diagenesis, Mg^{2+} in the water column could diffuse into the pore water and promote aragonite formation (Higgins et al., 2018; Hashim et al., 2021). Previous hypotheses suggest that $[Mg/Ca]_{sw}$ might control aragonite-calcite seas with the criterion that if $[Mg/Ca]_{sw}$ >2.0, then aragonite seas; if <2.0, then calcite seas (Hardie, 1996). In TAlkEaSy, we calculate $shelfarag_{Ca}$ according to (Eq. (32)):

$$shelfarag_{Ca} = mcbShelf_{Ca} \cdot \gamma_{Shelfarag} \quad (32)$$

where $\gamma_{Shelfarag}$ is the proportion of aragonite in marine shelf burial flux. The $\gamma_{Shelfarag}$ is linked to $[Mg/Ca]_{sw}$ by a sigmoidal equation considering all the above factors and previous hypotheses (Eq. (33)):

$$\gamma_{shelfarag} = \frac{1}{1+e^{-\beta_{shelfarag}\cdot([Mg/Ca]_{sw}-2.0)}} \quad (33)$$

where $\beta_{shelfarag}$ is an empirical coefficient we set to match the modern steady state at 1.5. Eq. (32)-(33) hypothesize the $[Mg/Ca]_{sw}$ has a first-order comprehensive control on the final abundance between aragonite and calcite in shelf carbonate burial, considering the effects both of authigenesis and diagenesis.

Ca isotope fractionation in carbonate is debated, and influenced by factors including mineralogy, temperature, carbonate saturation state and $[CO_3^{2-}]_{sw}$ (Gussone et al., 2016, 2020; Fantle and Ridgwell, 2020). Nevertheless, laboratory and field studies both found that Ca isotope fractionation between aragonite and calcite has a distinct difference due to their crystalline structure (Gussone et al., 2005, 2020; Higgins et al., 2018). Here, we apply $\delta^{44}Ca$ fractionation factors between aragonite ($\Delta^{44}Ca_{shelfarag-sw}$) and calcite ($\Delta^{44}Ca_{shelfcalc-sw}$) and seawater based on previous research in equilibrium states, which are about -1.70 ‰ and -0.80 ‰, respectively (Eq. (34)-(35)) (Gussone et al., 2005).

$$\Delta^{44}Ca_{shelfarag-sw} = \delta^{44}Ca_{shelfarag} - \delta^{44}Ca_{sw} \quad (34)$$

$$\Delta^{44}Ca_{shelfcalc-sw} = \delta^{44}Ca_{shelfcalc} - \delta^{44}Ca_{sw} \quad (35)$$

2.4.8 Sodium

Previous biogeochemical models have made little consideration of the global sodium cycle (Fig. 4), but it makes an important contribution to ocean alkalinity balance. Silicate weathering and high-temperature hydrothermal processes are important Na fluxes (Demicco et al., 2005; Halevy and Bachan, 2017; Guo and Korenaga, 2025). Halite weathering and burial fluxes may have varied over Earth's history (Halevy and Bachan, 2017). In specific periods, a reverse weathering Na flux might be very important (Isson and Planavsky, 2018). Na cation exchange processes with shallow sea boundary-layer sediments, suspended riverine sediments and deep-sea sediments are all thought to be important (Sun et al., 2016; Halevy and Bachan, 2017; Guo and Korenaga, 2025). In TAlkEaSy, we try to establish a complete, balanced global sodium cycle divided into three parts—Na silicate (Na_2SiO_3), Na halite (NaCl) and Na exchange (Na^+) systems.

The Na-silicate system is composed of silicate weathering ($silw_{Na}$), high-temperature hydrothermal removal ($hydhT_{Na}$) and reverse weathering (rw_{Na}) (Table 4). The functional form of $silw_{Na}$ is the same as Eq. (1)-(3). The different

https://doi.org/10.5194/egusphere-2026-2949
Preprint. Discussion started: 15 September 2026

percentages of Na in granite ($granw_{Na}$) and basalt ($basw_{Na}$) reflect different Na-rich minerals (e.g., albite) content and lithology (Table 5). For $hydhT_{Na}$, previous models have used different chemical equations (Table 3). Some models treat it as the exchange between Na^+ and Ca^{2+}, and others treat it as the precipitation of Na-clay by removing Na^+ (Table 3). Combining the first equation with the chemical equation of marine carbonate burial gives the second equation (Table 3). In theory, the released Ca^{2+} will finally precipitate as carbonate to maintain ocean alkalinity balance. The functional form of $hydhT_{Na}$ captures the influence of ***Na*** and *DEGASS* (Eq. (36)):

$$hydhT_{Na} = hydhT_{\mathrm{Na}},0 \cdot DEGASS \cdot \frac{\boldsymbol{Na}}{\boldsymbol{Na,0}} \quad (36)$$

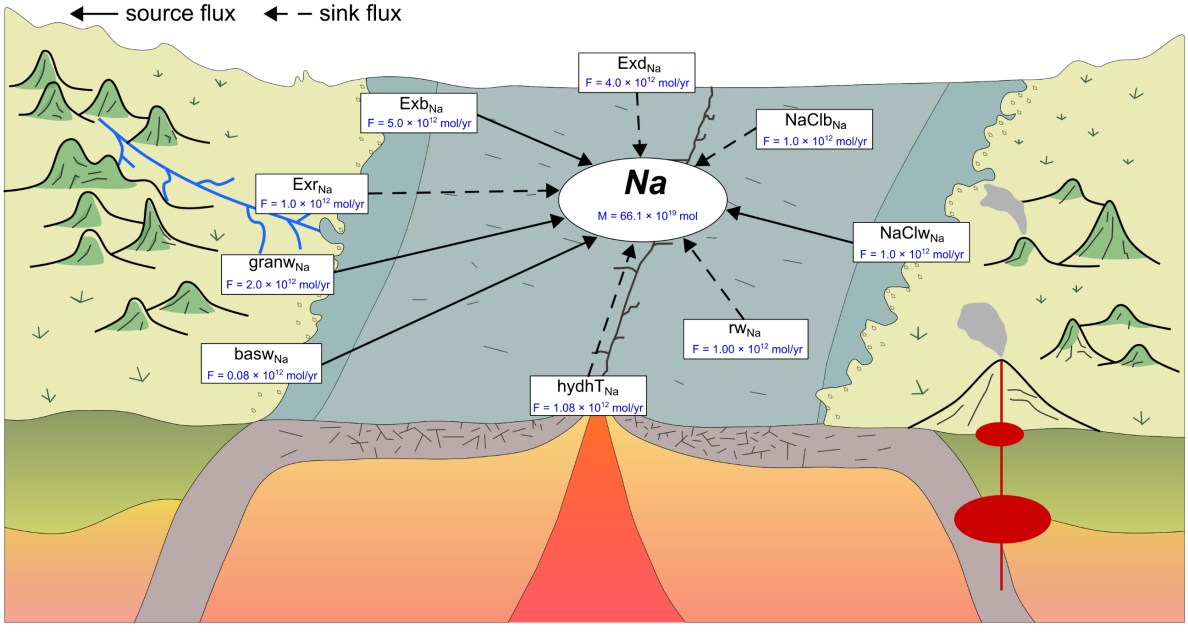

Figure 4: Ocean Na biogeochemical cycle and isotopic budget.

For rw_{Na}, we follow previous modelling works in assigning $[Na^+]_{sw}$ a first-order control on the flux (Arvidson et al., 2006) (Eq. (37)):

$$rw_{Na} = rw_{\mathrm{Na}},0 \cdot \frac{\boldsymbol{Na}}{\boldsymbol{Na,0}}, \quad (37)$$

The Na-halite system in TAlkEaSy includes the fluxes of NaCl weathering ($NaClw_{Na}$) and burial ($NaClb_{Na}$). $NaClw_{Na}$ is affected by *UPLIFT*, *PG*, NaCl reservoir size, runoff and land plant vegetation (Eq. (38)):

$$NaClw_{(Na,Cl)} = NaClw_{(Na,Cl)},0 \cdot UPLIFT \cdot PG \cdot \frac{\boldsymbol{NaCl}}{\boldsymbol{NaCl,0}} \cdot NaCl_{\mathrm{runoff}} \cdot f_{\mathrm{biota}}, \quad (38)$$

https://doi.org/10.5194/egusphere-2026-2949
Preprint. Discussion started: 15 September 2026

where $NaCl_{runoff}$ is the temperature dependency of NaCl weathering and dissolution. The activation energy for NaCl dissolution is reported to be 16 kJ mol^{-1} (Alkattan et al., 1997). We apply this and derive the NaCl temperature-dependent runoff equation by the Arrhenius equation as Eq. (39):

$$NaCl_{runoff} = 1 + 0.0232 \cdot \Delta T \quad (39)$$

For $NaClb_{Na}$, $[Na^+]_{sw}$ and $[Cl^-]_{sw}$ have first-order control on its precipitation and deposition rate (Eq. (40)):

$$NaClb_{(Na,Cl)} = NaClb_{(Na,Cl),0} \cdot \frac{Na}{Na,0} \cdot \frac{Cl}{Cl,0} \quad (40)$$

Na^+ should undergo cation exchange with other major ions like Ca^{2+} and Mg^{2+} (Tipper et al., 2021). However, in biogeochemical models these fluxes are not systematically incorporated in other major ion budgets (Halevy and Bachan, 2017; Guo and Korenaga, 2025) and we follow that treatment.

For the boundary-layer cation exchange Na flux (Exb_{Na}), we follow previous models in assuming it is a constant (Halevy and Bachan, 2017; Guo and Korenaga, 2025) Eq. (41):

$$Exb_{Na} = Exb_{\mathrm{Na},0} \quad (41)$$

Previous models suggest that the deep-sea sediment cation exchange Na flux (Exd_{Na}) is promoted by $[Na^+]_{sw}$ (Halevy and Bachan, 2017; Guo and Korenaga, 2025) (Eq. (42)):

$$Exd_{Na} = Exd_{\mathrm{Na},0} \cdot \frac{Na}{Na,0} \quad (42)$$

The riverine cation exchange Na flux (Exr_{Na}) is only linked to $[Na^+]_{sw}$ in previous models (Halevy and Bachan, 2017; Guo and Korenaga, 2025). However, recent research suggests that continental uplift and erosion intensity could change the suspended materials in the river, which could increase or decrease the reactant of Na cation exchange (Tipper et al., 2021). Hence, we also link *UPLIFT* to Exr_{Na} (Eq. (43)):

$$Exr_{Na} = Exr_{\mathrm{Na},0} \cdot UPLIFT \cdot \frac{Na}{Na,0} \quad (43)$$

2.4.9 Potassium

The potassium cycle is uncertain and methods for calculating $[K^+]_{sw}$ from halite fluid inclusion cast doubts on the authenticity of $[K^+]_{sw}$ trends (Timofeeff et al., 2001; Blättler, 2025). Nevertheless, we still try to incorporate a potassium cycle in TAlkEaSy, with silicate weathering ($silw_K$) and KCl weathering ($KClw_K$) as sources, and high-temperature hydrothermal ($hydhT_K$), reverse weathering (rw_K) and KCl burial ($KClb_K$) as sinks (Fig. 5).

The K fluxes of $silw_K$, $granw_K$ and $basw_K$ are the same as Eq. (1)-(3). $KClw_K$ incorporates the influencing factors of *UPLIFT*, *PG*, KCl reservoir size, runoff and land vegetation biota (Eq. (44)):

https://doi.org/10.5194/egusphere-2026-2949
Preprint. Discussion started: 15 September 2026

$$KClw_{(K,Cl)} = KClw_{(K,Cl),0} \cdot UPLIFT \cdot PG \cdot \frac{\boldsymbol{KCl}}{\boldsymbol{KCl,0}} \cdot KCl_{runoff} \cdot f_{biota} \quad (44)$$

where KCl_{runoff} is the temperature dependency of KCl weathering and dissolution. The activation energy for KCl dissolution is reported to be 8.5 kJ mol^{-1} (Lopes and Farelo, 2006). We derive the KCl temperature-dependent runoff equation by the Arrhenius equation as Eq. (45):

$$KCl_{runoff} = 1 + 0.0123 \cdot \Delta T \quad (45)$$

The equation of KCl burial ($KClb_K$) is assumed to be affected by $[K^+]_{sw}$ and $[Cl^-]_{sw}$ (Eq. (46)):

$$KClb_{(K,Cl)} = KClb_{(K,Cl),0} \cdot \frac{\boldsymbol{K}}{\boldsymbol{K,0}} \cdot \frac{\boldsymbol{Cl}}{\boldsymbol{Cl,0}} \quad (46)$$

The high-temperature hydrothermal K flux ($hydhT_K$) is promoted by *DEGASS* and $[K^+]_{sw}$ (Eq. (47)):

$$hydhT_K = hydhT_{K,0} \cdot DEGASS \cdot \frac{\boldsymbol{K}}{\boldsymbol{K,0}} \quad (47)$$

The reverse weathering K flux (rw_K) is assumed to be promoted by $[K^+]_{sw}$ (Eq. (48)):

$$rw_K = rw_{K,0} \cdot \frac{\boldsymbol{K}}{\boldsymbol{K,0}}, \quad (48)$$

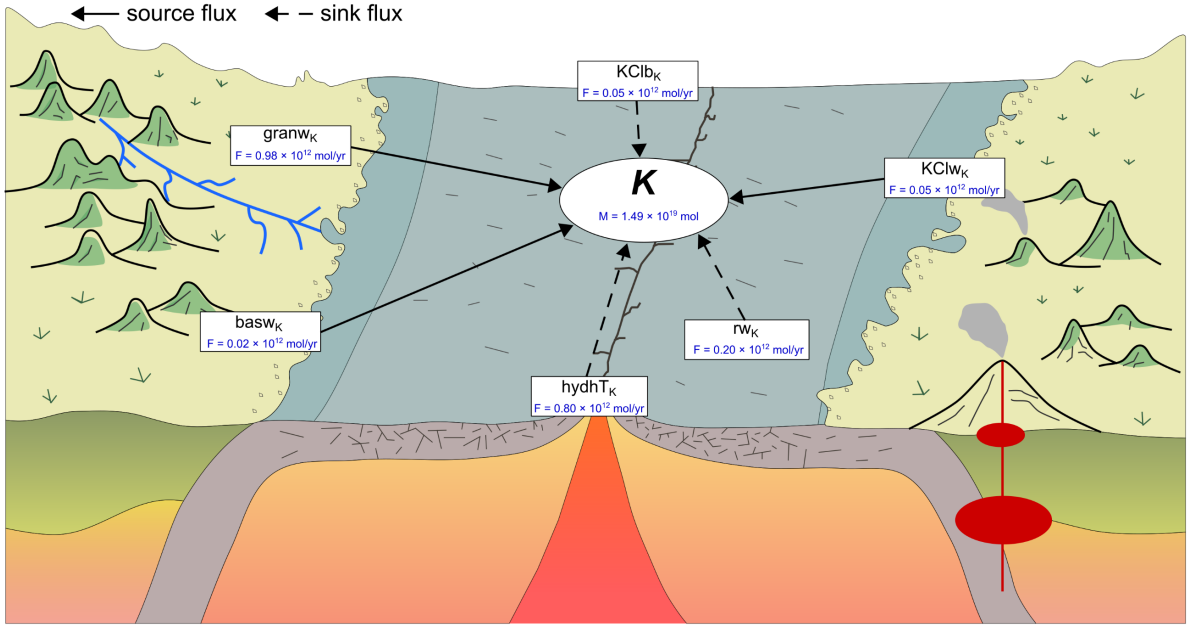

Figure 5: Ocean K biogeochemical cycle and isotopic budget.

https://doi.org/10.5194/egusphere-2026-2949
Preprint. Discussion started: 15 September 2026

2.4.10 Chlorine

The variations of $[Cl^-]_{sw}$ and its biogeochemical controls remain puzzles (Barnum and Coates, 2022). Nevertheless, we introduce a basic modelling framework which is helpful in making predictions on long timescales, incorporating fluxes of NaCl and KCl weathering and burial (Table 4), the magnitude of which are determined by the corresponding Na and K fluxes.

2.5 Passive biogeochemical tracer cycles

Passive biogeochemical tracer cycles refer to those which do not alter Earth system dynamics but can provide tracers of key processes. This means their changes and isotopic proxies could be used to constrain some specific processes. In TAlkEaSy, we incorporate Sr and U cycles in our model. The Sr cycle could help constrain continental weathering and hydrothermal fluxes. The U cycle is sensitive to seafloor anoxic areas.

2.5.1 Strontium

The Sr isotopic system has been widely applied in tracing processes especially continental weathering intensity and hydrothermal processes due to differing compositions of $^{87}Sr/^{86}Sr$ (Pearce et al., 2015). TAlkEaSy incorporates two reservoirs: ocean Sr (***OSr***) and sedimentary Sr (***SSr***) (Table 2). For the reservoir of ***OSr***, its sink fluxes include silicate ($silw_{Sr}$) from granite ($granw_{Sr}$) and basalt ($basw_{Sr}$), and carbonate weathering ($carbw_{Sr}$), high- ($hydhT_{Sr}$) and low-temperature hydrothermal ($hydlT_{Sr}$), and source fluxes are marine carbonate burial ($mcbTotal_{Sr}$) and seafloor weathering (sfw_{Sr}) (Table 5). As for ***SSr***, its source flux is $mcbTotal_{Sr}$ and sink fluxes are $carbw_{Sr}$ and sediment metamorphism ($metam_{Sr}$) (Fig. 6). The Sr continental weathering fluxes follow Eq. (1)-(4). The $^{87}Sr/^{86}Sr$ of granite ($^{87}Sr/^{86}Sr_{granCw}$), basalt ($^{87}Sr/^{86}Sr_{basCw}$) and carbonate ($^{87}Sr/^{86}Sr_{carbCw}$), are 0.714 , 0.705 and 0.708, respectively (Lenton et al., 2018). Different to COPSE, the mantle Sr input is divided into $hydhT_{Sr}$ and $hydlT_{Sr}$ (Table 4).

The high-temperature hydrothermal Sr flux ($hydhT_{Sr}$) has been suggested to be affected by *DEGASS* in previous models (Lenton et al., 2018), and we follow this equation in TAlkEaSy (Eq. (49)).

$$hydhT_{Sr} = hydhT_{Sr},0 \cdot DEGASS \quad (49)$$

The low-temperature hydrothermal Sr flux ($hydlT_{Sr}$) is simplified to have the same functional forms as the high-temperature flux in COPSE and many other models (Lenton et al., 2018; Zhang et al., 2018; Mills et al., 2025). However, some research suggests that the low-temperature hydrothermal Sr flux might have a strong temperature dependency (Coogan and Dosso, 2015). In TAlkEaSy, we consider the temperature effects by applying the Arrhenius equation on this process (Eq. (50)), assuming that the temperature in low-temperature hydrothermal reaction zones is 9 °C higher than global mean surface temperature. The activation energy is 92 ± 7 kJ mol^{-1}, referred from previous research (Coogan and Dosso, 2015).

$$hydlT_{Sr} = hydlT_{Sr},0 \cdot e^{0.125 \cdot \Delta T} \quad (50)$$

https://doi.org/10.5194/egusphere-2026-2949
Preprint. Discussion started: 15 September 2026

The $^{87}Sr/^{86}Sr$ of high- and low-temperature hydrothermal are parameterized to be 0.702 referred from previous works (Pearce et al., 2015). The Sr functional forms and isotopic compositions of marine carbonate burial ($mcbTotal_{Sr}$), seafloor weathering (sfw_{Sr}) and metamorphism ($metam_{Sr}$) are inherited from COPSE (Appendix Table A1) (Lenton et al., 2018).

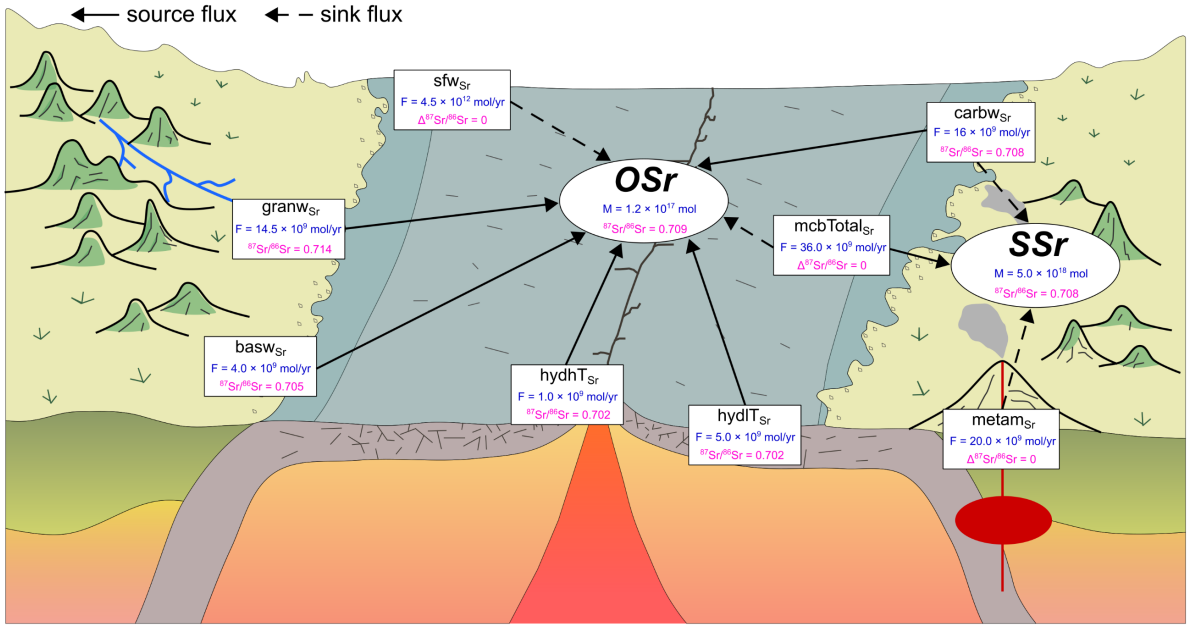

Figure 6: Ocean and sedimentary Sr biogeochemical cycles and isotopic ($^{87}Sr/^{86}Sr$) budget.

2.5.2 Uranium

Recently, the uranium isotopic system has been widely applied to infer deep ocean redox state for specific ocean anoxic and oxygenation events, like the Shuram excursion (Cao et al., 2020; Dodd et al., 2023), the transition during the Ediacaran-Cambrian (Dahl et al., 2014), the Permian-Triassic mass extinction (Zhang et al., 2020b), Oceanic Anoxic Events (OAEs) in the Cretaceous (Clarkson et al., 2018), and the Paleocene Eocene Thermal Maximum (PETM) (Clarkson et al., 2021). TAlkEaSy incorporates an ocean U biogeochemical cycle and its related processes, fluxes and feedbacks. The ocean $\boldsymbol{U}$ reservoir includes silicate weathering ($silw_{Sr}$) as the main source and high- ($hydhT_U$) and low-temperature hydrothermal processes ($hydlT_U$), anoxic ($anoxic_U$) and other non-anoxic sediment removal ($other_U$) as sinks (Fig. 7).

https://doi.org/10.5194/egusphere-2026-2949
Preprint. Discussion started: 15 September 2026

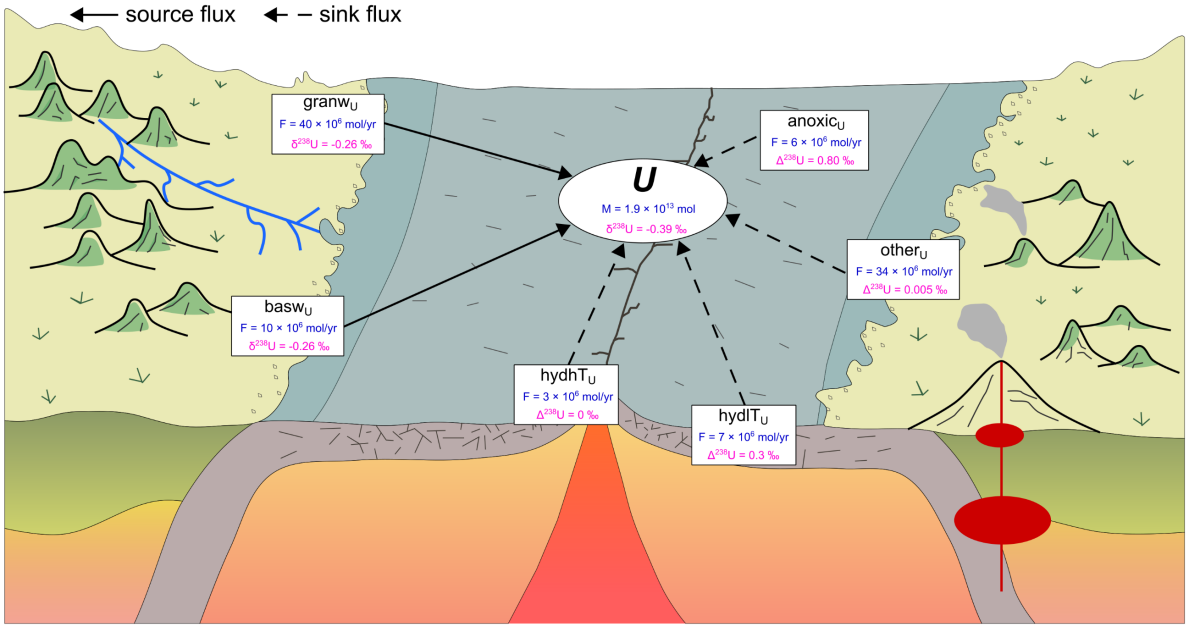

Figure 7: Ocean U biogeochemical cycle and isotopic (δ^{238}U) budget.

The silicate weathering fluxes of U follow the same partitioning into granite ($granw_U$) and basalt ($basw_U$) and functional responses as in Eq. (1)-(3). The δ^{238}U of $granw_U$ and $basw_U$ are set to be -0.26 ‰, near to the value of the bulk continental crust and very close to riverine composition (Lau et al., 2019; Zhang et al., 2020a).

The high-temperature hydrothermal U flux ($hydhT_U$) captures the total high-temperature hydrothermal intensity affected by *DEGASS* and ocean $\boldsymbol{U}$ reservoir size (Eq. (51)):

$$hydhT_U = hydhT_{U,0} \cdot DEGASS \cdot \frac{\boldsymbol{U}}{\boldsymbol{U_{,0}}} \quad (51)$$

The δ^{238}U fractionation factor during high-temperature hydrothermal processes ($\Delta^{238}U_{hydhT-sw}$) is set to be 0 ‰ adopted from a reported value (Eq. (52)) (Clarkson et al., 2021).

$$\Delta^{238}U_{hydhT-sw} = \delta^{238}U_{hydhT} - \delta^{238}U_{sw} \quad (52)$$

The low-temperature hydrothermal U flux is approximated to have a first-order dependency on ocean U reservoir as Eq. (53):

$$hydhlT_U = hydlT_{U,0} \cdot \frac{\boldsymbol{U}}{\boldsymbol{U_{,0}}} \quad (53)$$

The δ^{238}U fractionation factor between low-temperature hydrothermal and seawater ($\Delta^{238}U_{hydlT-sw}$) is around 0.30 ‰ (Eq. (54)) (Zhang et al., 2020a; Clarkson et al., 2021).

$$\Delta^{238}U_{hydlT-sw} = \delta^{238}U_{hydlT} - \delta^{238}U_{sw} \quad (54)$$

https://doi.org/10.5194/egusphere-2026-2949
Preprint. Discussion started: 15 September 2026

Key to the oceanic U isotopic system is its fractionation in anoxic sinks. In TAlkEaSy, the removal flux $anoxic_U$ is promoted by oceanfloor anoxic area ($ANOX$) and the size of $\boldsymbol{U}$ (Eq. (55)), as suggested by previous models (Clarkson et al., 2018, 2021; Zhang et al., 2020a):

$$anoxic_U = anoxic_{U,0} \cdot \frac{\boldsymbol{U}}{\boldsymbol{U_0}} \cdot ANOX \quad (55)$$

The $\delta^{238}U$ fractionation factor between $anoxic_U$ and seawater ($\Delta^{238}U_{anoxic-sw}$) is taken as 0.80 ‰, based on previous research (Eq. (56)) (Clarkson et al., 2018, 2021; Zhang et al., 2020a).

$$\Delta^{238}U_{anoxic-sw} = \delta^{238}U_{anoxic} - \delta^{238}U_{sw} \quad (56)$$

The flux of $other_U$ consists of U removal fluxes in carbonate, suboxic sediments and oxic metals (Clarkson et al., 2018; Zhang et al., 2020a). In TAlkEaSy, $other_U$ is simplified to have a first-order dependence on $\boldsymbol{U}$ (Eq. (57)):

$$other_U = other_{U,0} \cdot \frac{\boldsymbol{U}}{\boldsymbol{U_0}} \quad (57)$$

The fractionation factor of $\delta^{238}U$ in $other_U$ is around 0.005 ‰ (Eq. (58)) (Clarkson et al., 2018; Zhang et al., 2020a).

$$\Delta^{238}U_{other-sw} = \delta^{238}U_{other} - \delta^{238}U_{sw} \quad (58)$$

2.6 Ocean alkalinity-carbonate chemistry systems

The ocean alkalinity-carbonate chemistry system in TAlkEaSy model is based on Eq. (59), which incorporates the dynamic changes from both ocean major ions, carbonic acid species, hydrogen and hydroxyl ions and boron.

$$[TAlk]_{sw} = 2 \cdot [Ca^{2+}]_{sw} + 2 \cdot [Mg^{2+}]_{sw} - 2 \cdot [SO_4^{2-}]_{sw} + [Na^+]_{sw} + [K^+]_{sw} - [Cl^-]_{sw} = [HCO_3^-]_{sw} + 2 \cdot [CO_3^{2-}]_{sw} + [B(OH)_4^-]_{sw} + [OH^-]_{sw} - [H^+]_{sw} \quad (59)$$

The ocean major ion concentrations are controlled by their biogeochemical cycles on varying timescales.

Dissolved inorganic carbon (DIC) is composed of free aqueous carbon dioxide ($[CO_2]_{sw}$), bicarbonate ion ($[HCO_3^-]_{sw}$) and carbonate ion ($[CO_3^{2-}]_{sw}$) (Eq. (60)) (Zeebe, 2012b):

$$[DIC]_{sw} = [CO_2]_{sw} + [HCO_3^-]_{sw} + [CO_3^{2-}]_{sw} \quad (60)$$

The boron system assumes the sum of $[B(OH)_4^-]_{sw}$ and $[B(OH)_3]_{sw}$ is a constant, based on previous modelling (Clarkson et al., 2015). Apportioning between $[B(OH)_4^-]_{sw}$ and $[B(OH)_3]_{sw}$ is affected by ocean pH state (Zeebe and Wolf-Gladrow, 2001; Clarkson et al., 2015).

Equilibria among DIC and boron species concentrations are determined by corresponding equilibrium constants (K_1^*, K_2^*, K_B^*, K_w^*) (Eq. (61)-(65)), which are dependent on temperature, pressure and salinity (Zeebe and Wolf-Gladrow, 2001). In our current configuration, we calculate the stoichiometric equilibrium constants near the present-day conditions (temperature

https://doi.org/10.5194/egusphere-2026-2949
Preprint. Discussion started: 15 September 2026

=15 ℃, pressure =1 atm, salinity =35) to meet reasonable steady states. The values of pK_1^*, pK_2^*, pK_B^*, pK_w^* in TAlkEaSy model are 5.94, 9.13, 8.72, and 13.60 respectively.

$$K_1^* = \frac{[HCO_3^-]_{sw} \cdot [H^+]_{sw}}{[CO_2]_{sw}} \quad (61)$$

$$K_2^* = \frac{[CO_3^{2-}]_{sw} \cdot [H^+]_{sw}}{[HCO_3^-]_{sw}} \quad (62)$$

$$K_B^* = \frac{[B(OH)_4^-]_{sw} \cdot [H^+]_{sw}}{[B(OH)_3]_{sw}} \quad (63)$$

$$K_w^* = [H^+]_{sw} \cdot [OH^-]_{sw} \quad (64)$$

$$pK_X^* = -log_{10}(K_X^*) \quad (65)$$

2.7 Coding language and numerical solver

Our TAlkEaSy is built on our modelling platform named POEM (Platform Of Earth-system Modelling) in Julia. Source code like the numerical solver (Solver.jl) could be imported from the POEM github repository to improve the efficiency of the code but we keep a frozen zip file which includes a solver with the code. For the TAlkEaSy model, the differential equations are solved using a variable-step variable-order implicit routine for stiff systems, making use of the SUite of Nonlinear and DIfferential/Algebraic equation Solvers (SUNDIALS) package.

3 Sensitivity experiments, result and discussion

In this section, we conduct two sensitivity tests of the TAlkEaSy model from the modern steady state to assess the model response: (1) CO_2 pulse, which represents an abrupt perturbation thought to drive some geological events; (2) Increase *DEGASS*, which represents a longer-term change in tectonic forcing. For each, we show and discuss the responses of carbon and oxygen cycles, ocean major ion concentrations, marine carbonate chemistry and seawater isotopes.

3.1 CO_2 pulse

In this scenario, we input an idealised CO_2 pulse into the atmosphere in the modern steady state (Fig. 8a). The CO_2 input rate is 20×10^{12} mol C/yr for 1 Myr, with $\delta^{13}C$ of 0 ‰. This partially represents some driving forcings and hypotheses in extreme geological events.

3.1.1 Carbon and oxygen cycles response

The input of CO_2 into the atmosphere drives an expected increase of CO_2 and global temperature (Fig. 8a, 8b, 8c) with global temperature increasing ~6 ℃ (Fig. 8c).

https://doi.org/10.5194/egusphere-2026-2949
Preprint. Discussion started: 15 September 2026

Atmosphere O_2 is elevated from 21% to >24% by the CO_2 input (Fig. 8d), and ocean anoxic area first increases and then declines (Fig. 8e). The phosphorous cycle is key to these responses. Increased CO_2 and temperature increase continental weathering fluxes, releasing more phosphorus from rocks (Appendix Fig. B1). This drives up land and ocean productivity and organic carbon burial, increasing atmospheric O_2, but also increases demand for O_2 in the ocean. As the ocean P reservoir responds faster than atmosphere O_2, ocean anoxic fraction first rises (Fig. 8e) and then as atmosphere O_2 increases and oxygenates the ocean (Fig. 8d), it declines (Fig. 8e).

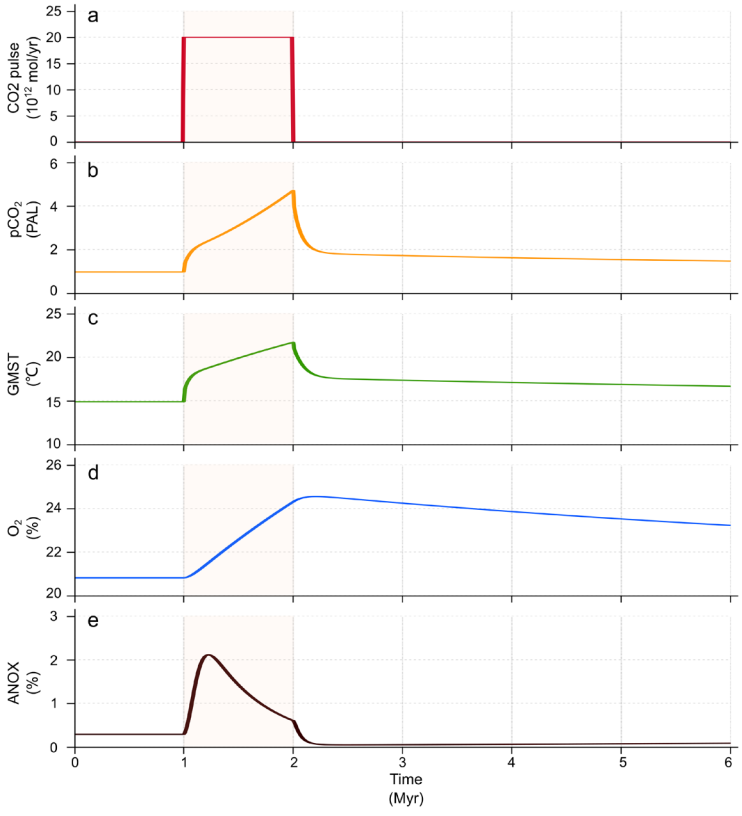

Figure 8: The changes of global carbon and oxygen cycles towards CO_2 pulse. (a) The prescribed CO_2 pulse. (b) The pCO_2 state. (c) The GMST (global mean surface temperature) state. (d) The atmospheric O_2 state. (e) The ANOX (ocean anoxic area percentage) state.

3.1.2 Ocean major ions response

Among ocean major ions, $[Mg^{2+}]_{sw}$ exhibits the most significant rise during the CO_2 pulse (Fig. 9a) because elevated continental weathering fluxes provide Mg sources (Appendix Fig. B2). $[Na^{+}]_{sw}$ and $[K^{+}]_{sw}$ also have slightly rises due to enhanced silicate weathering input (Fig. 9d, 9e). $[Cl^{-}]_{sw}$ has minimal variations as its large reservoir size is not significantly altered by the responses of NaCl and KCl weathering and burial fluxes (Appendix Fig. B5, B6).

https://doi.org/10.5194/egusphere-2026-2949
Preprint. Discussion started: 15 September 2026

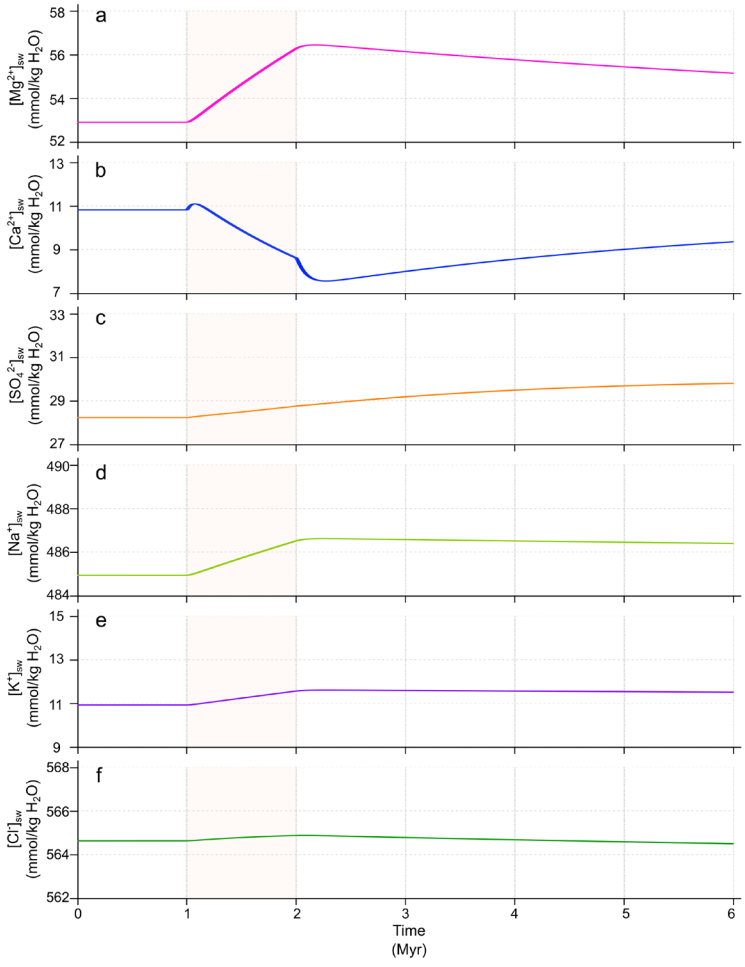

635 **Figure 9: The changes of ocean major ions towards CO_2 pulse.** (a) $[Mg^{2+}]_{sw}$. (b) $[Ca^{2+}]_{sw}$. (c) $[SO_4^{2-}]_{sw}$. (d) $[Na^{+}]_{sw}$. (e) $[K^{+}]_{sw}$. (f) $[Cl^{-}]_{sw}$.

$[Ca^{2+}]_{sw}$ first shows a small increase driven by enhanced weathering inputs but then declines during the CO_2 pulse (Fig. 9b). This is because $[Ca^{2+}]_{sw}$ adjusts to counter the rise in $[TAlk]_{sw}$ (Fig. 10a) driven mostly by increasing $[Mg^{2+}]_{sw}$, tending to maintain ocean charge balance and alkalinity balance (Halevy and Bachan, 2017, Kump, 2026). The relatively small magnitude
640 of $[Ca^{2+}]_{sw}$ variation is consistent with the LOSCAR model response (Komar and Zeebe, 2011), i.e. the carbon cycle perturbation has only a modest effect on $[Ca^{2+}]_{sw}$.

$[SO_4^{2-}]_{sw}$ increases slightly (Fig. 9c) due to increased continental pyrite and gypsum weathering inputs and reduced marine gypsum burial linked to declining $[Ca^{2+}]_{sw}$ (Appendix Fig. B4).

https://doi.org/10.5194/egusphere-2026-2949
Preprint. Discussion started: 15 September 2026

3.1.3 Ocean carbonate chemistry response

The CO_2 pulse increases $[TAlk]_{sw}$ (Fig. 10a) as enhanced continental weathering increases the input of cations to the ocean (Appendix Fig. B1). Dissolved inorganic carbon species all increase as the CO_2 injected into the atmosphere is taken up by the ocean (Fig. 10b, 10c, 10d).

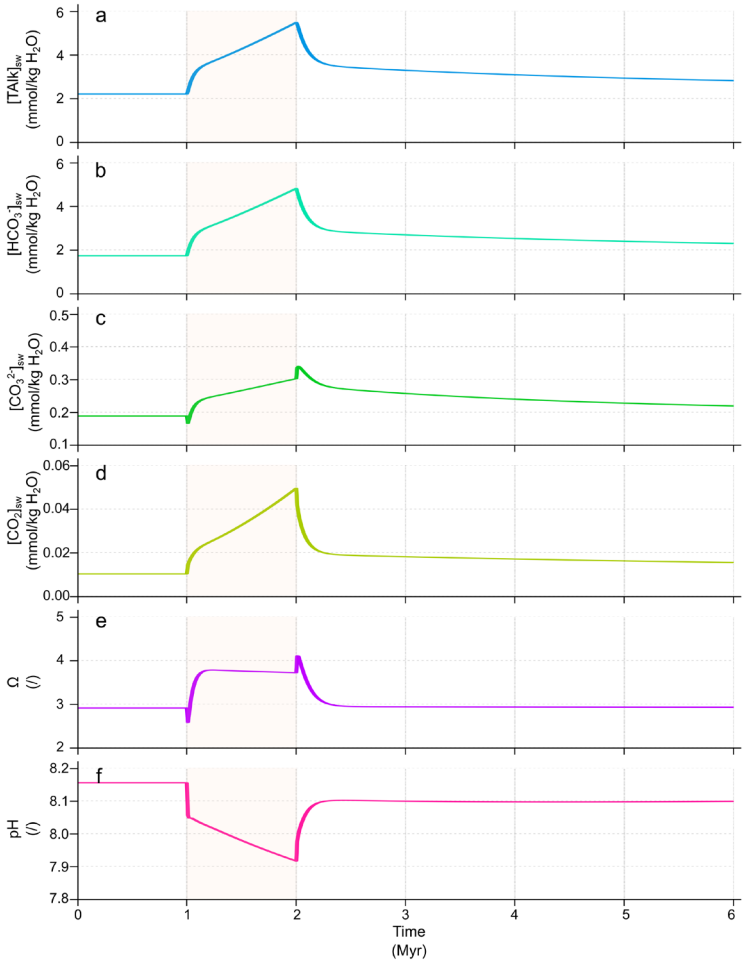

Figure 10: The changes of ocean carbonate chemistry towards CO_2 pulse. (a) $[TAlk]_{sw}$. (b) $[HCO_3^-]_{sw}$. (c) $[CO_3^{2-}]_{sw}$. (d) $[CO_2]_{sw}$. (e) Ω. (f) pH.

Continental weathering cation input to the ocean is balanced by marine carbonate burial (Zeebe, 2012b). The adjustment works via the carbonate saturation state abruptly increasing (Fig. 10e) until this drives sufficient carbonate burial to balance the elevated weathering input (Appendix Fig. B1). The CO_2 injection drives ocean acidification—lowering of pH (Fig. 10f) consistent with other models (Payne et al., 2010).

https://doi.org/10.5194/egusphere-2026-2949
Preprint. Discussion started: 15 September 2026

3.1.4 Isotopic responses

$\delta^{13}C_{sw}$ increases sharply because of the increase of land and marine organic burial in removing light carbon (Fig. 11a and Appendix Fig. B1). $\delta^{34}S_{sw}$ rises slightly during the CO_2 pulse because of elevated pyrite burial, linked to increased organic carbon burial (Fig. 11b and Appendix Fig. B4). $\delta^{238}U$ has a sharp decrease during the CO_2 pulse (Fig. 11c) as the expansion of oceanfloor anoxic area (Fig. 8e and Appendix Fig. B8).

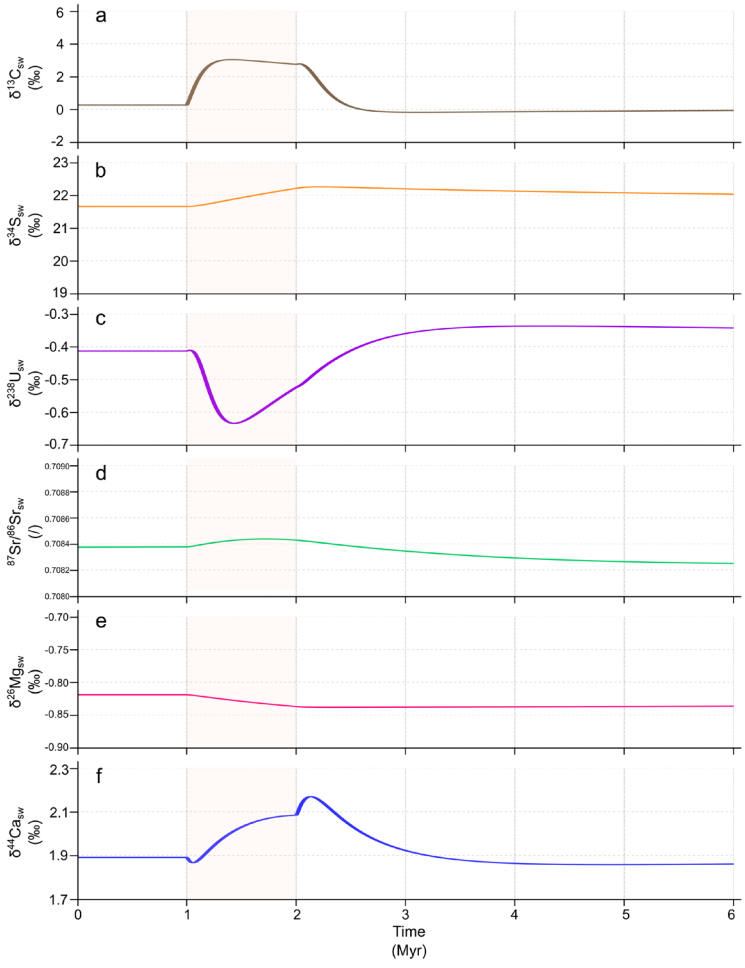

Figure 11: The changes of seawater isotopes towards CO_2 pulse. (a) $\delta^{13}C$ of seawater ($\delta^{13}C_{sw}$). (b) $\delta^{34}S$ of seawater ($\delta^{34}S_{sw}$). (c) $\delta^{238}U$ of seawater ($\delta^{238}U_{sw}$). (d) $^{87}Sr/^{86}Sr$ of seawater ($^{87}Sr/^{86}Sr_{sw}$). (e) $\delta^{26}Mg$ of seawater ($\delta^{26}Mg_{sw}$). (f) $\delta^{44}Ca$ of seawater ($\delta^{44}Ca_{sw}$).

$^{87}Sr/^{86}Sr_{sw}$ increases a little during the CO_2 injection (Fig. 11d) linked to increased granite weathering with high $^{87}Sr/^{86}Sr$ values, outweighing increased basalt weathering with low $^{87}Sr/^{86}Sr$ values (Appendix Fig. B7).

Although $[Mg^{2+}]_{sw}$ shows significant changes in the CO_2 pulse period, $\delta^{26}Mg_{sw}$ has little change (Fig. 11e), because of counteracting effects on Mg isotopic fluxes. Increased granite and basalt weathering fluxes, characterized by high $\delta^{26}Mg$,

https://doi.org/10.5194/egusphere-2026-2949
Preprint. Discussion started: 15 September 2026

are counterbalanced by increased carbonate weathering with very low $\delta^{26}Mg$ values (Appendix Fig. B2). Changes in low-temperature hydrothermal and secondary dolomitization fluxes, make contributions as well (Appendix Fig. B2).

$\delta^{44}Ca_{sw}$ increases during the CO_2 injection interval (Fig. 11f), because the elevated $[Mg/Ca]_{sw}$ promotes more aragonite burial (Appendix Fig. B9), which has a large $\delta^{44}Ca$ fractionation factor. Transient responses of $\delta^{44}Ca_{sw}$ at the start and end of the CO_2 injection interval are related to abrupt shifts in saturation state and carbonate burial flux.

3.2 Increase in degassing

An idealised doubling of *DEGASS* forcing approximates the maximum increase (relative to present) during Phanerozoic time. As well as driving CO_2 variation on million years timescale (Berner, 1991), it is linked to MOR expansion and thus the intensities of high-temperature hydrothermal processes (Berner, 2004; Higgins et al., 2015). In the sensitivity test, we increase the *DEGASS* intensity from the modern steady state to two times higher over 100 million years (Fig. 12a).

3.2.1 Carbon and oxygen cycles response

Doubling *DEGASS* (Fig. 12a) increases pCO_2 to around 7 times higher than the present-day (Fig. 12b) (Appendix Fig. C1), elevating global surface mean temperature by 8 °C (Fig. 12c). Atmosphere O_2 level is predicted to increase to ~30 % (Fig. 12d) driven by increased continental weathering of phosphorus fuelling productivity and organic carbon burial (and Appendix Fig. C1). The ocean anoxic area shrinks accordingly (Fig. 12e).

https://doi.org/10.5194/egusphere-2026-2949
Preprint. Discussion started: 15 September 2026

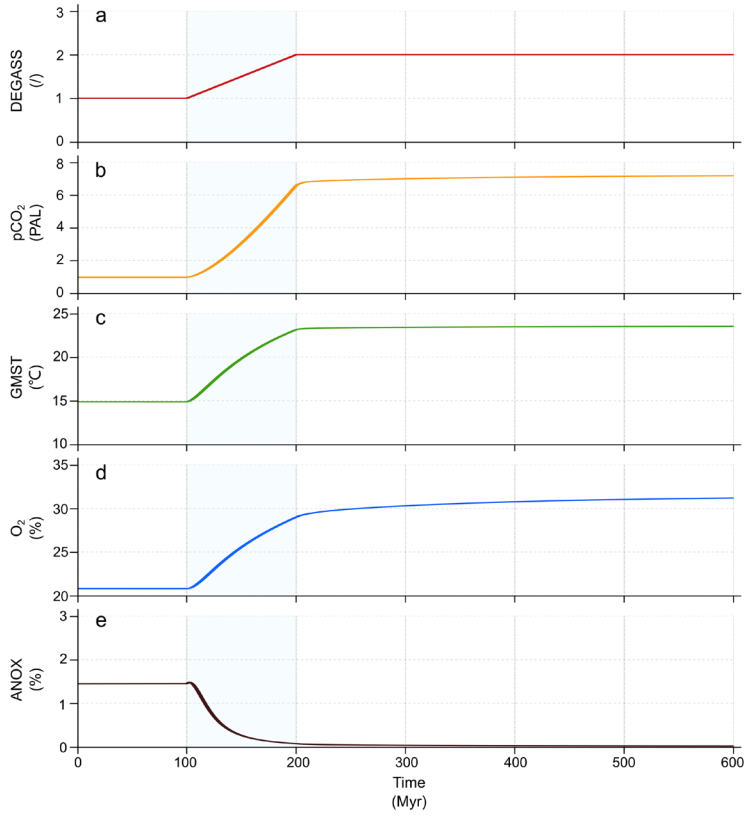

685 **Figure 12: The changes of global carbon and oxygen cycles towards DEGASS elevation.** (a) The prescribed CO_2 pulse. (b) The pCO_2 state. (c) The GMST (global mean surface temperature) state. (d) The atmospheric O_2 state. (e) The ANOX (ocean anoxic area percentage) state.

3.2.2 Ocean major ions response

690 Very different from the short timescale perturbation, long timescale changes in *DEGASS* can greatly affect ocean major ion concentrations. $[Mg^{2+}]_{sw}$ increases by ~15 mmol/kg H_2O (Fig. 13a) due to increases in weathering inputs of Mg exceeding increased high-temperature hydrothermal Mg removal (Appendix Fig. C2). $[Na^{+}]_{sw}$ also increases due to increased input fluxes from silicate weathering overwhelming increases in high-temperature hydrothermal removal fluxes of Na (Fig. 13d and Appendix Fig. C5). On the contrary, $[K^{+}]_{sw}$ decreases because the high-temperature hydrothermal K sink flux overwhelms
695 silicate weathering fluxes (Fig. 13d and Appendix Fig. C6). $[Cl^{-}]_{sw}$ is dependent on Na and K evaporite weathering and burial. Compared to KCl related fluxes, the fluxes of NaCl weathering and burial are much larger (Appendix Fig. C5, C6). The decrease of NaCl weathering causes $[Cl^{-}]_{sw}$ to drop (Fig. 13f and Appendix Fig. C5).

https://doi.org/10.5194/egusphere-2026-2949
Preprint. Discussion started: 15 September 2026

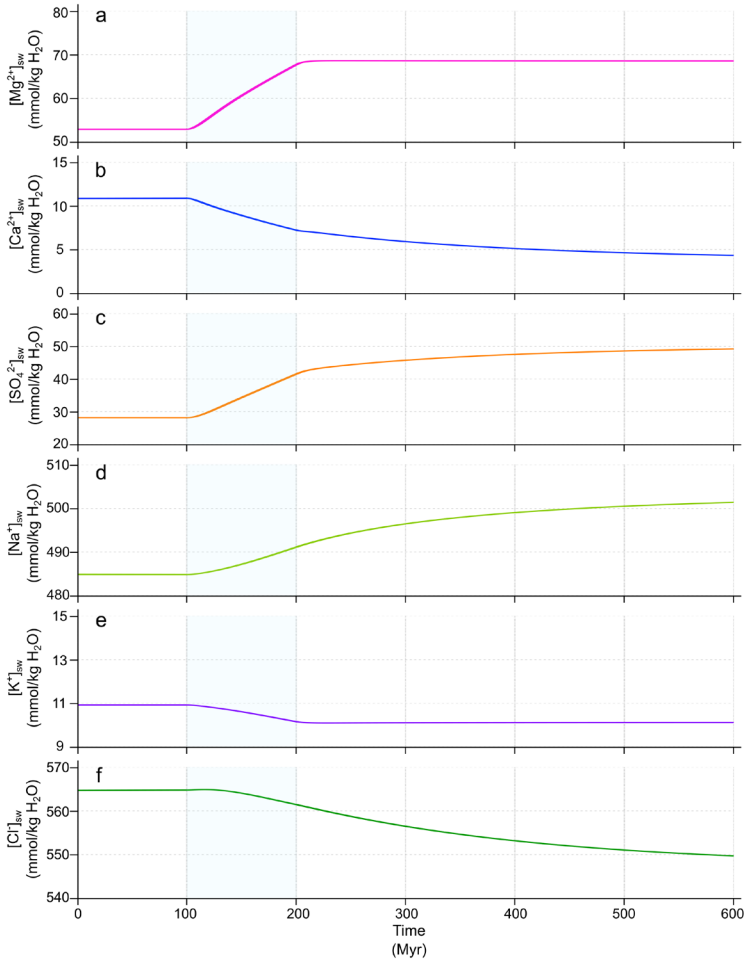

Figure 13: The changes of ocean major ions towards DEGASS elevation. (a) $[Mg^{2+}]_{sw}$. (b) $[Ca^{2+}]_{sw}$. (c) $[SO_4^{2-}]_{sw}$. (d) $[Na^{+}]_{sw}$. (e) $[K^{+}]_{sw}$. (f) $[Cl^{-}]_{sw}$.

The response of $[Ca^{2+}]_{sw}$ opposes changes to $[TAlk]_{sw}$ (Halevy and Bachan, 2017, Kump, 2026). Increased continental weathering cation input increases $[TAlk]_{sw}$ (Fig. 14a and Appendix Fig. C1), and $[Ca^{2+}]_{sw}$ decreases in response (Fig. 13b). $[SO_4^{2-}]_{sw}$ increases due to multiple factors (Fig. 13c). Pyrite and gypsum degassing fluxes are increased (Appendix Fig. C4). Also, the decrease of $[Ca^{2+}]_{sw}$ (Fig. 13b), lowers the burial flux of gypsum (Appendix Fig. C4).

3.2.3 Ocean carbonate chemistry response

The increase of *DEGASS* has a large effect on marine carbonate chemistry of greater magnitude than the transient CO_2 pulse. $[TAlk]_{sw}$ increases considerably (Fig. 14a) due to increased cation input from elevated continental weathering (Appendix Fig. C1). DIC species—$[HCO_3^{-}]_{sw}$, $[CO_3^{2-}]_{sw}$ and $[CO_2]_{sw}$ all increase with the growing atmosphere-ocean carbon reservoir (Fig.

https://doi.org/10.5194/egusphere-2026-2949
Preprint. Discussion started: 15 September 2026

14b, 14c, 14d). Increased cation input is balanced by increased marine carbonate burial, after adjustment of the ocean carbonate saturation state (Fig. 14e and Appendix Fig. C1). Increased CO_2 causes ocean acidification—a drop of pH (Fig. 14f).

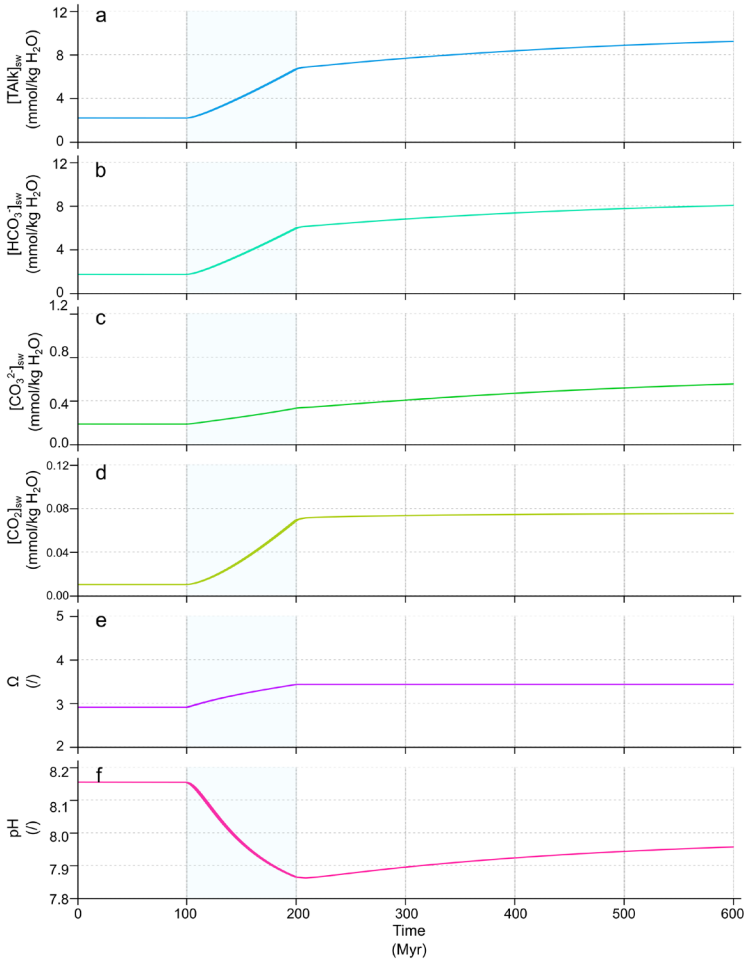

Figure 14: The changes of ocean carbonate chemistry towards DEGASS elevation. (a) $[TAlk]_{sw}$. (b) $[HCO_3^-]_{sw}$. (c) $[CO_3^{2-}]_{sw}$. (d) $[CO_2]_{sw}$. (e) Ω. (f) pH.

3.2.4 Isotopic response

There is little increase in $\delta^{13}C_{sw}$ (Fig. 15a) because only marine organic carbon burial flux is slightly increased (Appendix Fig. C1). $\delta^{34}S_{sw}$ increases significantly (Fig. 15b) because of elevated marine pyrite burial linked to elevated $[SO_4^{2-}]_{sw}$ characterized by large fractionation (Fig. 13c and Appendix Fig. C4). $\delta^{238}U$ is increased as the ocean anoxia area disappears (Fig. 12e, 15c and Appendix Fig. C8).

https://doi.org/10.5194/egusphere-2026-2949
Preprint. Discussion started: 15 September 2026

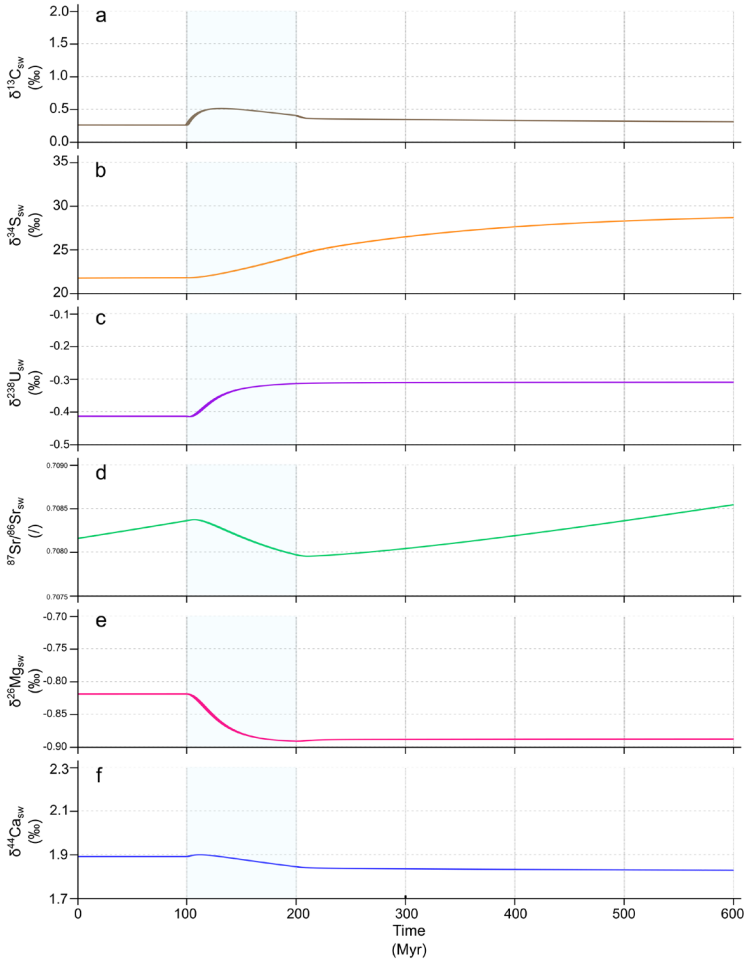

Figure 15: The changes of seawater isotopes towards DEGASS elevation. (a) $\delta^{13}C$ of seawater ($\delta^{13}C_{sw}$). (b) $\delta^{34}S$ of seawater ($\delta^{34}S_{sw}$). (c) $\delta^{238}U$ of seawater ($\delta^{238}U_{sw}$). (d) $^{87}Sr/^{86}Sr$ of seawater ($^{87}Sr/^{86}Sr_{sw}$). (e) $\delta^{26}Mg$ of seawater ($\delta^{26}Mg_{sw}$). (f) $\delta^{44}Ca$ of seawater ($\delta^{44}Ca_{sw}$).

$^{87}Sr/^{86}Sr_{sw}$ shows an ongoing decrease when *DEGASS* is increasing (Fig. 15d), caused by increased hydrothermal inputs which are a light Sr input (Appendix Fig. C7). In the other times, the change of $^{87}Sr/^{86}Sr_{sw}$ is caused by the Rb-Sr decay process rather than the source-sink flux balance (Fig. 15d).

$\delta^{26}Mg_{sw}$ shows negative changes because the fluxes including continental weathering, seafloor weathering and low-temperature hydrothermal are increased by *DEGASS* (Fig. 15e and Appendix Fig. C2). The continental weathering averaged input from silicate and carbonate weathering are characterized by $\delta^{26}Mg$ values lighter than seawater. Seafloor weathering is a Mg source within $\delta^{26}Mg$ lighter than seawater and low-temperature hydrothermal is a Mg sink within a heavier positive $\delta^{26}Mg$ fractionation factor between the reactant and seawater.

Different from the CO_2 pulse test, $\delta^{44}Ca_{sw}$ shows minimal variation (Fig. 15f) because of counterbalancing effects. The increase of $[Mg/Ca]_{sw}$ tends to promote more aragonite burial and increasing $\delta^{44}Ca_{sw}$ (as in the CO_2 pulse experiment)

https://doi.org/10.5194/egusphere-2026-2949
Preprint. Discussion started: 15 September 2026

(Fig. 13a, 13b). However, low $\delta^{44}Ca$ fluxes including granite, basalt and carbonate weathering and high- and low-temperature hydrothermal counterbalance the rise of $\delta^{44}Ca_{sw}$ (Appendix Fig. C3, C9).

4 Future development directions

The TAlkEaSy model is designed and coded in a way that more spatially resolved configurations can be developed. For land settings, the SCION model approach could be adopted to quantify spatially resolved continental weathering since the Neoproterozoic (Mills et al., 2025). Currently, we are developing a TAlkEaSy-SCION model to do this. Adding spatial resolution to the ocean could help to resolve different redox and burial settings, for example, distinguishing organic carbon and phosphorous burial in shelf, slope and deep sea. Currently we are experimenting with using the transport matrix from GENIE as a spatially-resolved ocean. Additional chemical species could also be added to TAlkEaSy. Chemical species like CH_4, Fe^{2+}-Fe^{3+} and H_2S are important in the evolution of CO_2 and O_2 and Earth habitability (Catling and Zahnle, 2020). The Si cycle related to reverse weathering, might be crucial in regulating ocean chemistry (Isson and Planavsky, 2018). The incorporation of some of these chemical species and cycles may be necessary to make accurate Precambrian predictions.

5 Conclusion

The new TAlkEaSy model (v1.0) builds on COPSE and makes significant progress compared to existing biogeochemical models: (1) it is the first forward biogeochemical model which incorporates carbon, oxygen, nutrients, ocean major ions and carbonate chemistry together; (2) it includes an ocean alkalinity system that is both affected by ocean major ions and their dynamic cycle processes and carbonic acid species which are linked to ocean carbonate chemistry; (3) it incorporates classic isotopic proxies of $\delta^{13}C$, $\delta^{34}S$ and $^{87}Sr/^{86}Sr$ with novel stable isotopes of $\delta^{26}Mg$, $\delta^{44}Ca$ and $\delta^{238}U$ and their dynamic fractionation mechanisms. The model response to idealised short-term perturbation and long-term change in forcing of the carbon cycle is reasonable and already reveals interesting responses of major ions and novel isotope systems.

https://doi.org/10.5194/egusphere-2026-2949
Preprint. Discussion started: 15 September 2026

Appendix A: Tables of variables and their functional forms

Table A1. Variables and functional forms of C, N, P and S cycles referred from COPSE model

Label	Equation	No.
Carbon cycle fluxes		
$cdeg_{C}$	$cdeg_{C} = cdeg_{C,0} \cdot \frac{\boldsymbol{CARB}}{\boldsymbol{CARB,0}} \cdot DEGASS \cdot PELAGIC$	A1
$odeg_{(C,O)}$	$odeg_{(C,O)} = odeg_{(C,O),0} \cdot DEGASS \cdot \frac{\boldsymbol{ORG}}{\boldsymbol{ORG,0}}$	A2
$lob_{(C,O)}$	$lob_{(C,O)} = lob_{(C,O),0} \cdot CP_{land} \cdot Rpland$	A3
$mob_{(C,O)}$	$mob_{(C,O)} = mob_{(C,O),0} \cdot \left(\frac{newp}{newp,0}\right)^{2.0}$	A4
Nitrogen cycle fluxes		
$nfix_{N}$	$nfix_{N} = \begin{cases} nfix_{N,0} \cdot \left(\frac{\boldsymbol{P} - \frac{\boldsymbol{N}}{r_{N:P}}}{\boldsymbol{P,0} - \frac{\boldsymbol{N,0}}{r_{N:P}}}\right), & \frac{\boldsymbol{N}}{r_{N:P}} < \boldsymbol{P} \\ 0, & \frac{\boldsymbol{N}}{r_{N:P}} \geq \boldsymbol{P} \end{cases}$	A5
$denit_{N}$	$denit_{N} = denit_{N,0} \cdot \left(1 + \frac{ANOX}{1 - k_{oxic}}\right) \cdot \frac{\boldsymbol{N}}{\boldsymbol{N,0}}$	A6
mob_{N}	$mob_{N} = \frac{mob_{C}}{CN_{sea}}$	A7
Phosphorus cycle fluxes		
$silw_{P}$	$silw_{P} = phosw_{P,0} \cdot r_{silw_P} \cdot \frac{silw_{C}}{silw_{C,0}}$	A8
$carbw_{P}$	$carbw_{P} = phosw_{P,0} \cdot r_{carbw_P} \cdot \frac{carbw_{C}}{carbw_{C,0}}$	A9
$oxidw_{P}$	$oxidw_{P} = phosw_{P,0} \cdot r_{oxidw_P} \cdot \frac{oxidw_{C}}{oxidw_{C,0}}$	A10
$phosw_{P}$	$phosw_{P} = P_{selective} \cdot (silw_{P} + carbw_{P} + oxidw_{P})$	A11
$psea_{P}$	$psea_{P} = phosw_{P} - pland_{P}$	A12
$pland_{P}$	$pland_{P} = k_{plandfrac} \cdot VEG \cdot Burial_{P} \cdot phosw_{P}$	A13
mob_{P}	$mob_{P} = \frac{mob_{P}}{CP_{sea}}$	A14
$fepb_{P}$	$fepb_{P} = fepb_{P,0} \cdot \frac{1-ANOX}{k_{oxic}} \cdot \frac{\boldsymbol{P}}{\boldsymbol{P,0}}$	A15
$capb_{P}$	$capb_{P} = capb_{P,0} \cdot \left(\frac{newp}{newp,0}\right)^{2.0} \cdot \left[0.5 + 0.5 \cdot \frac{1-ANOX}{k_{oxic}}\right]$	A16
Sulphur cycle fluxes		
$pyrw_{S}$	$pyrw_{S} = pyrw_{S,0} \cdot UPLIFT \cdot \frac{\boldsymbol{PYR}}{\boldsymbol{PYR,0}}$	A17
$pyrdeg_{S}$	$pyrdeg_{S} = pyrdeg_{S,0} \cdot DEGASS \cdot \frac{\boldsymbol{PYR}}{\boldsymbol{PYR,0}}$	A18
$gypdeg_{S}$	$gypdeg_{S} = gypdeg_{S,0} \cdot DEGASS \cdot \frac{\boldsymbol{GYP}}{\boldsymbol{GYP,0}}$	A19
Air-sea exchange fluxes		
$airsea_{C}$	$airsea_{C} = vpiston \cdot oceanarea \cdot \left(KCO_{2,0} \cdot \frac{\boldsymbol{CO_2}}{moles1atm} - [CO_2]_{SW}\right)$	A20
$airsea_{O}$	$airsea_{O} = vpiston \cdot oceanarea \cdot \left(KO_{2,0} \cdot \frac{\boldsymbol{AO_2}}{moles1atm} - [O_2]_{SW}\right)$	A21

https://doi.org/10.5194/egusphere-2026-2949
Preprint. Discussion started: 15 September 2026

Table A2. Non-flux variables and functional forms referred from COPSE model

Description	Label	Equation	No.
Global mean surface temperature relative to present (℃)	ΔT	$\Delta T = k_c \cdot lnCO_2 - \frac{k_l \cdot t}{570\ (Ma)}$	A22
Global mean surface temperature (℃)	$GMST$(℃)	$GMST(℃) = 15 + \Delta T$	A23
Temperature kinetic effects on weathering	$f_{T(gran,bas)}$	$f_{T(gran,bas)} = e^{k_T^i \cdot \Delta T}$	A24
Runoff effects on silicate weathering	f_{runoff}	$f_{runoff} = [1 + 0.038 \cdot \Delta T]^{0.65}$	A25
Runoff effects on carbonate weathering	g_{runoff}	$g_{runoff} = 1 + 0.087 \cdot \Delta T$	A26
Land plant effects on terrestrial weathering	f_{biota}	$f_{biota} = (1 - \min(VEG \cdot W, 1)) \cdot k_{plantenhance} \cdot {CO_2}^{0.5} + VEG \cdot W$	A27
Land vegetation normalized biomass	VEG	$VEG = V_{npp} \cdot V_{fire}$	A28
Global vegetation net primary productivity	V_{npp}	$V_{npp} = k_{npp} \cdot EVO \cdot V_T \cdot V_{CO_2} \cdot V_{O_2}$	A29
Temperature effects on land vegetation	V_T	$V_T = 1 - \left(\frac{GMST(℃) - 25}{25}\right)^2$	A30
CO_2 effects on land vegetation	V_{CO_2}	$V_{CO_2} = \frac{pCO_2 - P_{min}}{P_{1/2} + pCO_2 - P_{min}}$	A31
Fire effects on land vegetation	V_{fire}	$V_{fire} = \frac{k_{fire}}{k_{fire} - 1 + ignit}$	A32
Marine new productivity	$newp$	$newp = r_{C:P} \cdot min(30.9 \cdot \frac{\boldsymbol{N}}{\boldsymbol{N,0}} \cdot \frac{1}{r_{N:P}}, 2.2 \cdot \frac{\boldsymbol{P}}{\boldsymbol{P,0}})$	A33
Marine organic burial ratio of C to P	CP_{sea}	$CP_{sea} = \frac{k_{oxic} \cdot k_{anoxic}}{(1 - ANOX) \cdot k_{anoxic} + ANOX \cdot k_{oxic}}$	A34
Environmental effects on phosphorus burial	$Burial_P$	$Burial_P = k_{aq} + [(1 - k_{aq}) \cdot COAL]$	A35

https://doi.org/10.5194/egusphere-2026-2949
Preprint. Discussion started: 15 September 2026

Table A3. Parameters meaning and values in TAlkEaSy model

Description	Label	Values
The sensitivity of climate to CO_2	k_c	4.328
The sensitivity of climate to changing solar luminosity	k_l	7.4
The activation energy about granite weathering rate	k_T^{gran}	0.0724
The activation energy about basalt weathering rate	k_T^{bas}	0.0608
The enhancement of plant on terrestrial weathering	$k_{plantenhance}$	0.15
The fraction of P buried on land	$k_{plandfrac}$	0.0588
The minimum atmospheric pCO_2 that plant could grow	P_{min}	10
The half pCO_2 saturation of vegetation	$P_{1/2}$	183.6
Wildfire effect on vegetation biomass	k_{fire}	3
Redfield ratio of C and P	$r_{C:P}$	117
Redfield ratio of N and P	$r_{N:P}$	16
Marine organic matter burial ratio of C and N	CN_{sea}	37.5
The organic burial ratio of C:P in oxic bottom water	k_{oxic}	250
The organic burial ratio of C:P in anoxic bottom water	k_{anoxic}	4000
The fraction of terrestrial organic matter burial in aquatic settings	k_{aq}	0.85
The fraction of P from silicate weathering	r_{silw_P}	0.88
The fraction of P from carbonate weathering	r_{carbw_P}	0.06
The fraction of P from oxidative weathering	r_{oxidw_P}	0.06
Henry's constant of CO_2 (Temperature = 15℃, pressure = 1 atm, salinity = 35)	$KCO_2, 0$	38.5
Henry's constant of O2 (Temperature = 15℃, pressure = 1 atm, salinity = 35)	$KO_2, 0$	1.25

775

https://doi.org/10.5194/egusphere-2026-2949
Preprint. Discussion started: 15 September 2026

Appendix B: Figures of the related fluxes of CO_2 pulse sensitivity test

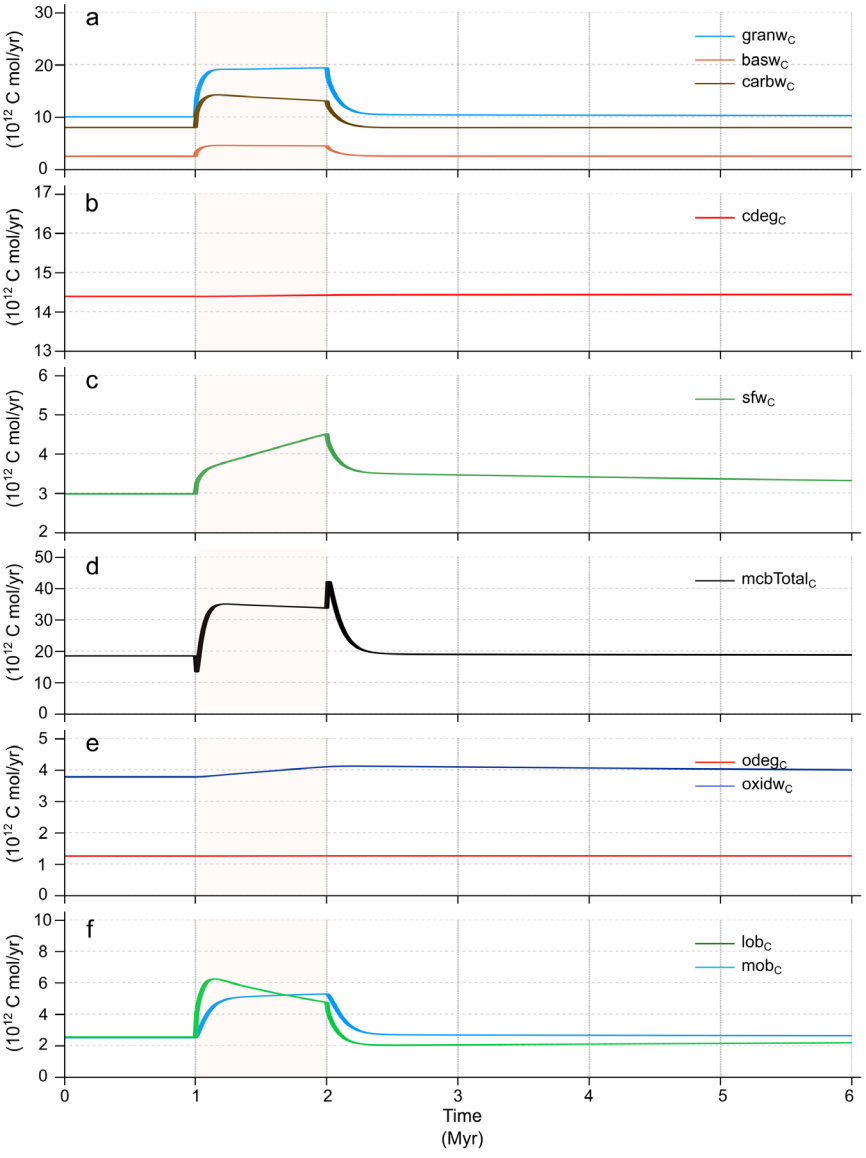

780

Figure B1: The changes of carbon cycle fluxes towards CO_2 pulse. (a) continental weathering (granite, basalt and carbonate) fluxes. (b) carbonate degassing flux. (c) seafloor weathering flux. (d) marine total carbonate burial flux. (e) organic degassing and oxidative weathering fluxes. (f) land and marine organic burial fluxes.

https://doi.org/10.5194/egusphere-2026-2949
Preprint. Discussion started: 15 September 2026

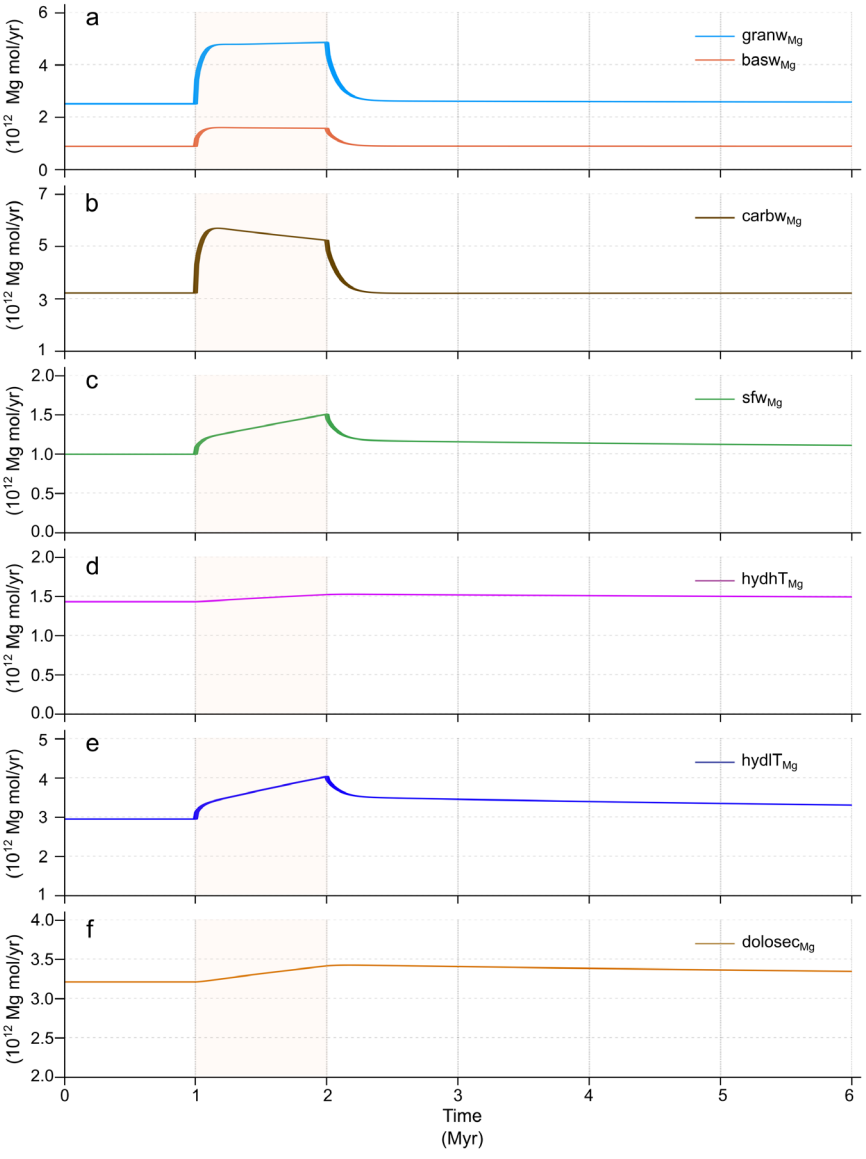

785

Figure B2: The changes of magnesium cycle fluxes towards CO_2 pulse. (a) silicate weathering (granite and basalt) Mg fluxes. (b) carbonate weathering Mg flux. (c) seafloor weathering Mg flux. (d) high-temperature hydrothermal Mg flux. (e) low-temperature hydrothermal Mg flux. (f) secondary dolomitization Mg flux.

https://doi.org/10.5194/egusphere-2026-2949
Preprint. Discussion started: 15 September 2026

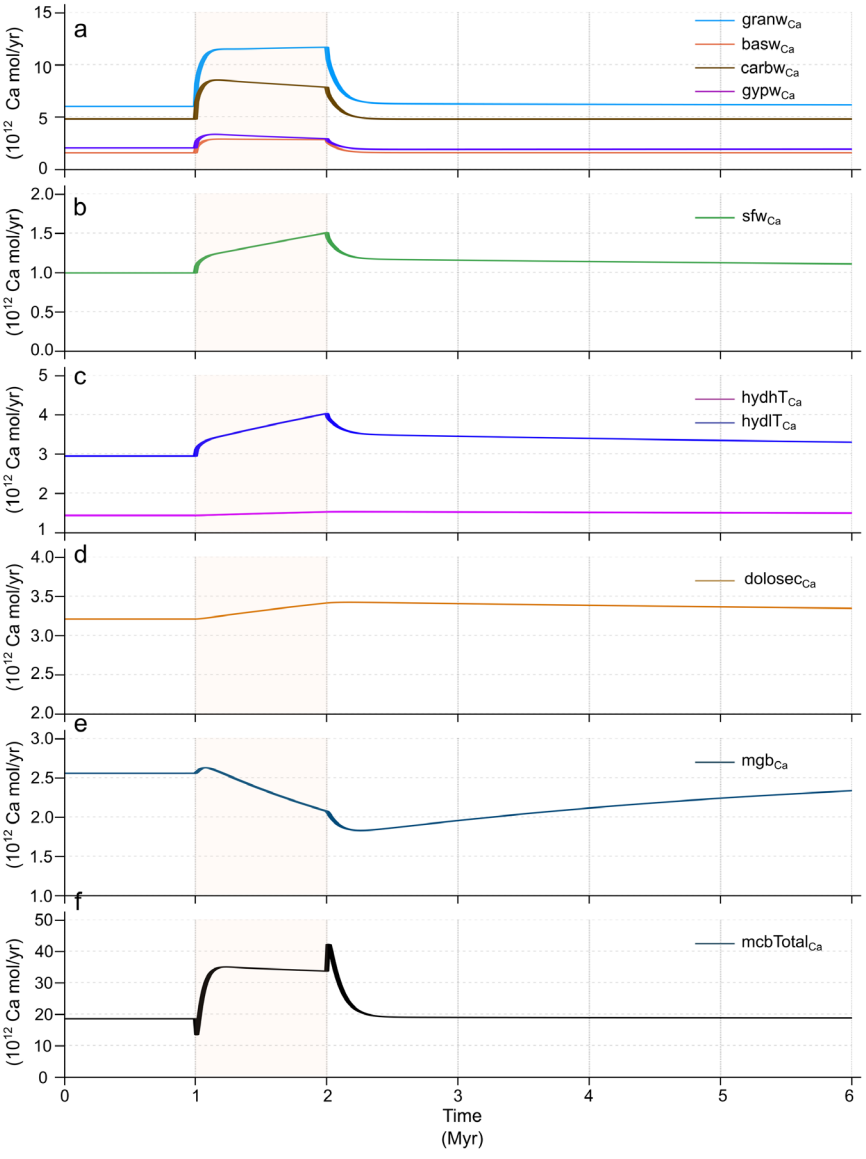

Figure B3: The changes of calcium cycle fluxes towards CO_2 pulse. (a) continental weathering (granite, basalt, carbonate and gypsum) Ca fluxes. (b) seafloor weathering Ca flux. (c) high- and low-temperature hydrothermal Ca fluxes. (d) secondary dolomitization Ca flux. (e) marine gypsum burial Ca flux. (f) marine total carbonate burial Ca flux.

https://doi.org/10.5194/egusphere-2026-2949
Preprint. Discussion started: 15 September 2026

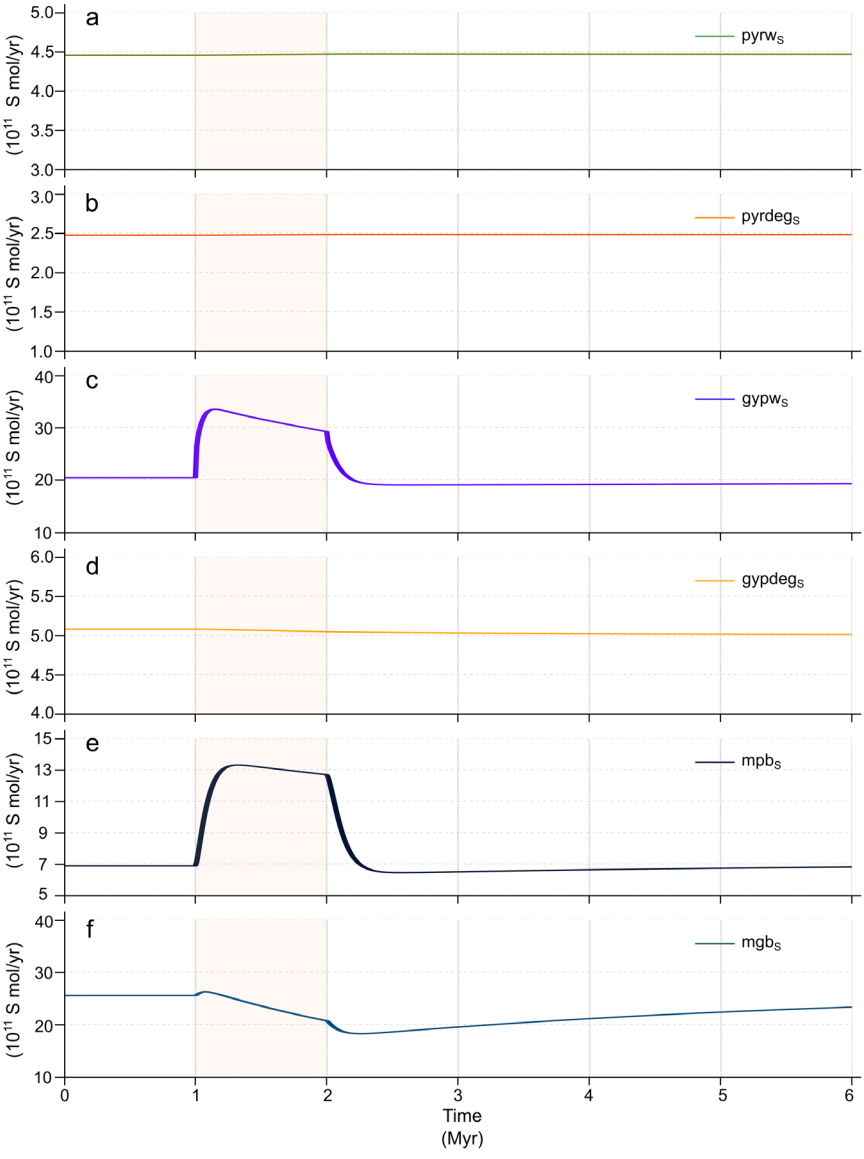

795

Figure B4: The changes of sulphur cycle fluxes towards CO_2 pulse. (a) pyrite weathering S flux. (b) pyrite degassing S flux. (c) gypsum weathering S flux. (d) gypsum degassing S flux. (e) marine pyrite burial S flux. (f) marine gypsum burial S flux.

https://doi.org/10.5194/egusphere-2026-2949
Preprint. Discussion started: 15 September 2026

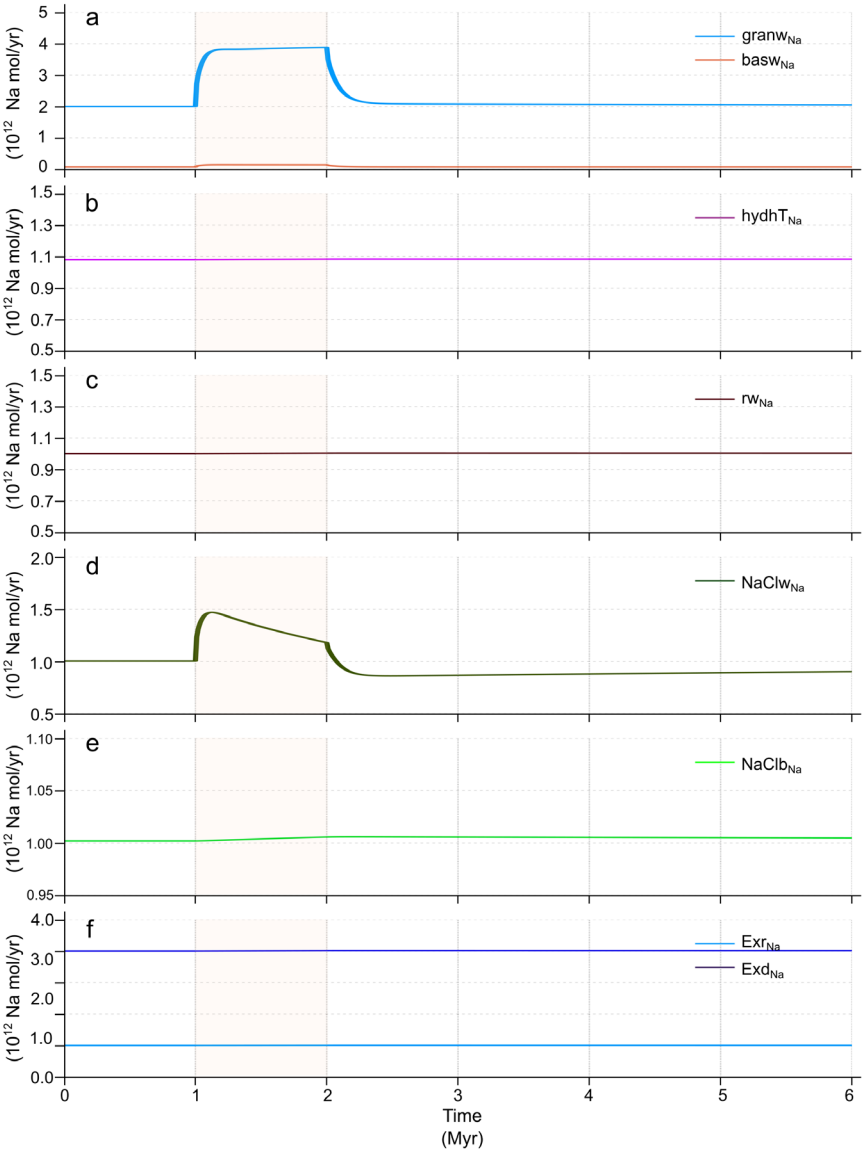

800 **Figure B5: The changes of sodium cycle fluxes towards CO_2 pulse.** (a) silicate weathering (granite and basalt) Na fluxes. (b) high-temperature hydrothermal Na flux. (c) reverse weathering Na flux. (d) NaCl weathering Na flux. (e) NaCl burial Na flux. (f) riverine and deep-sea cation exchange Na fluxes.

https://doi.org/10.5194/egusphere-2026-2949
Preprint. Discussion started: 15 September 2026

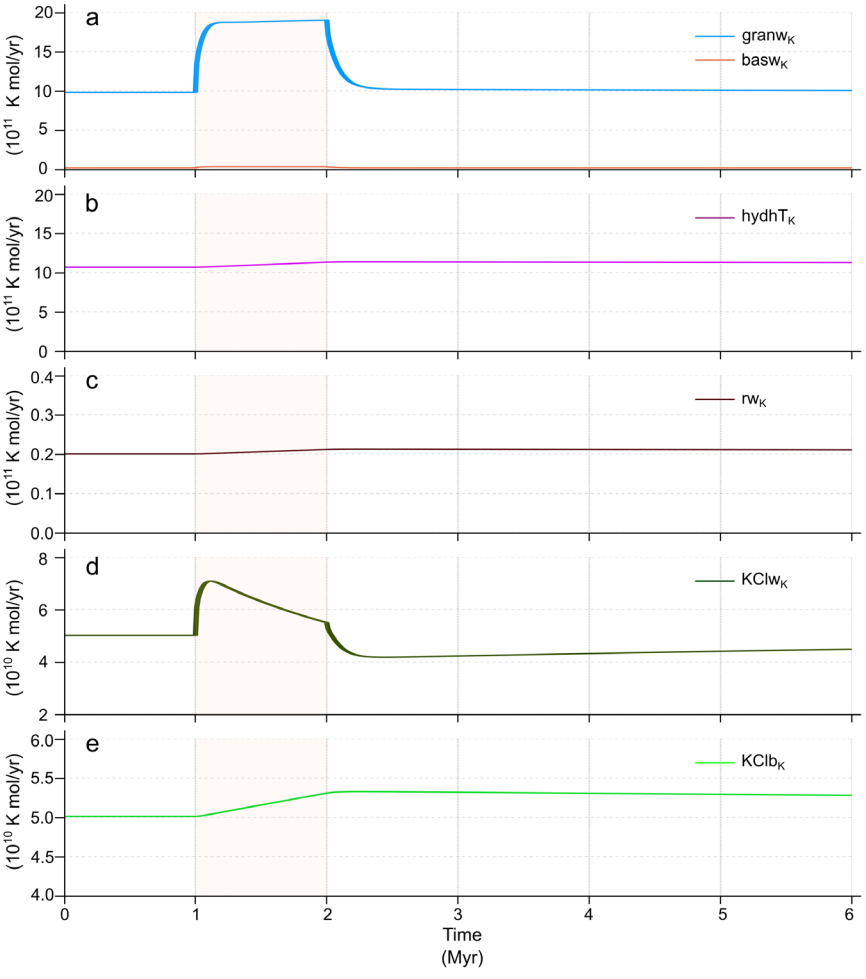

805 **Figure B6: The changes of potassium cycle fluxes towards CO_2 pulse.** (a) silicate weathering (granite and basalt) K fluxes. (b) high-temperature hydrothermal K flux. (c) reverse weathering K flux. (d) KCl weathering K flux. (e) KCl burial K flux.

https://doi.org/10.5194/egusphere-2026-2949
Preprint. Discussion started: 15 September 2026

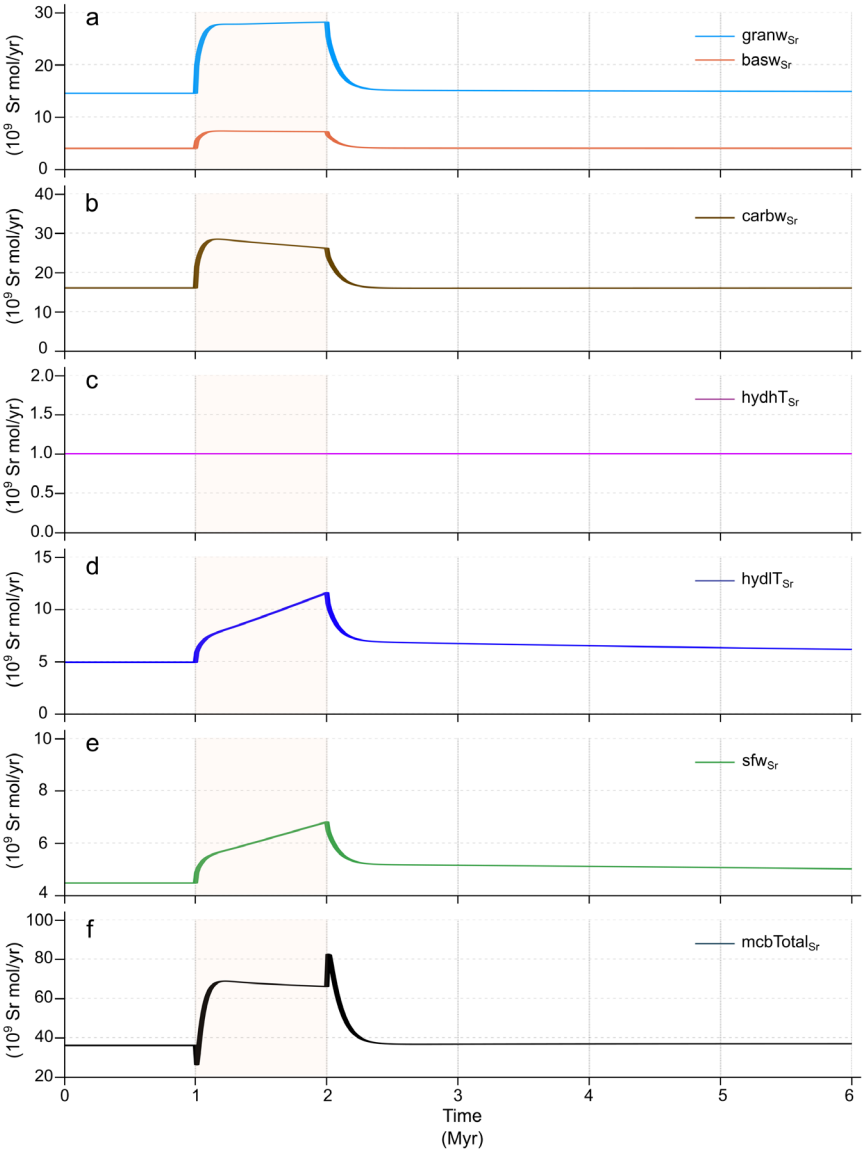

Figure B7: The changes of strontium cycle fluxes towards CO_2 pulse. (a) silicate weathering (granite and basalt) Sr fluxes. (b) carbonate weathering Sr flux. (c) high-temperature hydrothermal Sr flux. (d) low-temperature hydrothermal Sr flux. (e) seafloor weathering Sr flux. (f) marine carbonate burial Sr flux.

https://doi.org/10.5194/egusphere-2026-2949
Preprint. Discussion started: 15 September 2026

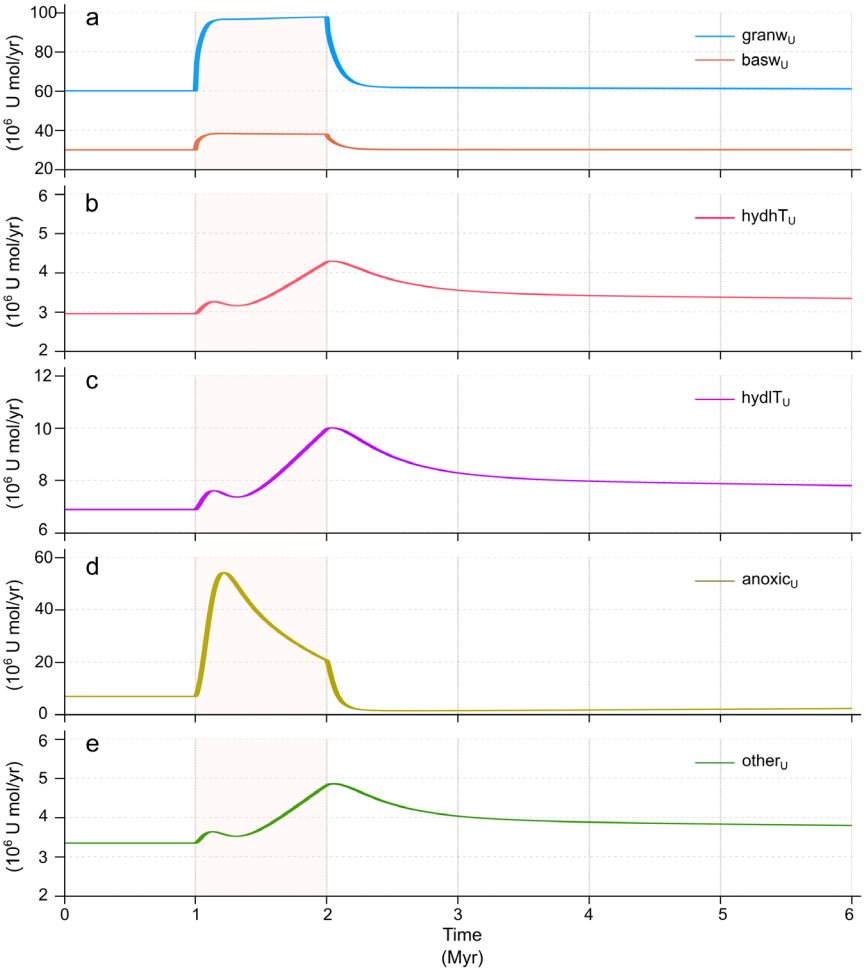

Figure B8: The changes of uranium cycle fluxes towards CO_2 pulse. (a) silicate weathering (granite and basalt) U fluxes. (b) anoxic burial U flux. (c) other burial U flux. (d) high-temperature hydrothermal U flux. (e) low-temperature hydrothermal U flux.

https://doi.org/10.5194/egusphere-2026-2949
Preprint. Discussion started: 15 September 2026

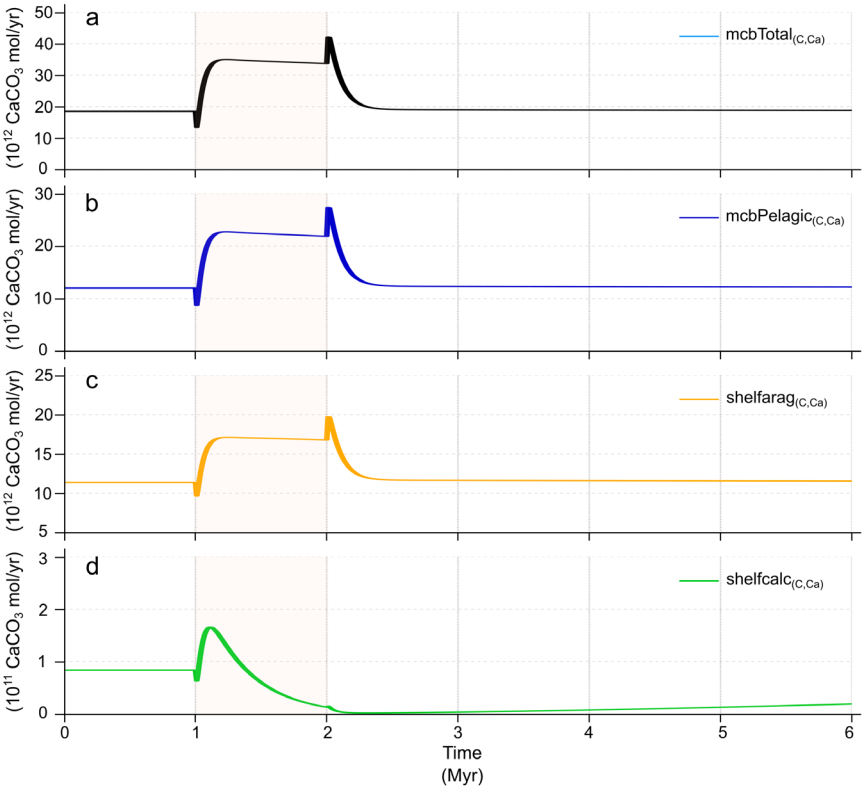

Figure B9: The changes of marine carbonate burial fluxes towards CO_2 pulse. (a) marine total carbonate burial flux. (b) pelagic carbonate burial flux. (c) shelf aragonite burial flux. (d) shelf calcite burial flux.

https://doi.org/10.5194/egusphere-2026-2949
Preprint. Discussion started: 15 September 2026

Appendix C: Figures of the related fluxes of DEGASS elevation sensitivity test

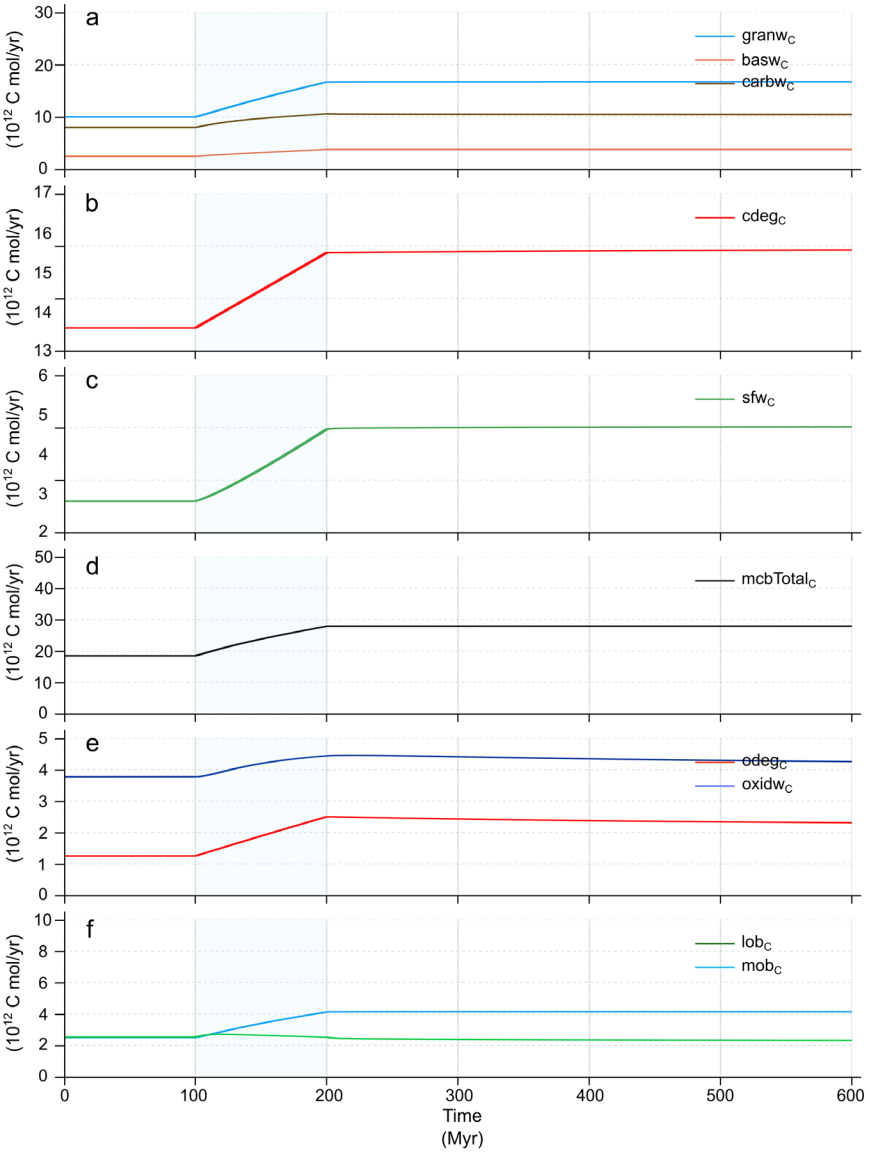

Figure C1: The changes of carbon cycle fluxes towards DEGASS elevation. (a) continental weathering (granite, basalt and carbonate) fluxes. (b) carbonate degassing flux. (c) seafloor weathering flux. (d) marine total carbonate burial flux. (e) organic degassing and oxidative weathering fluxes. (f) land and marine organic burial fluxes.

https://doi.org/10.5194/egusphere-2026-2949
Preprint. Discussion started: 15 September 2026

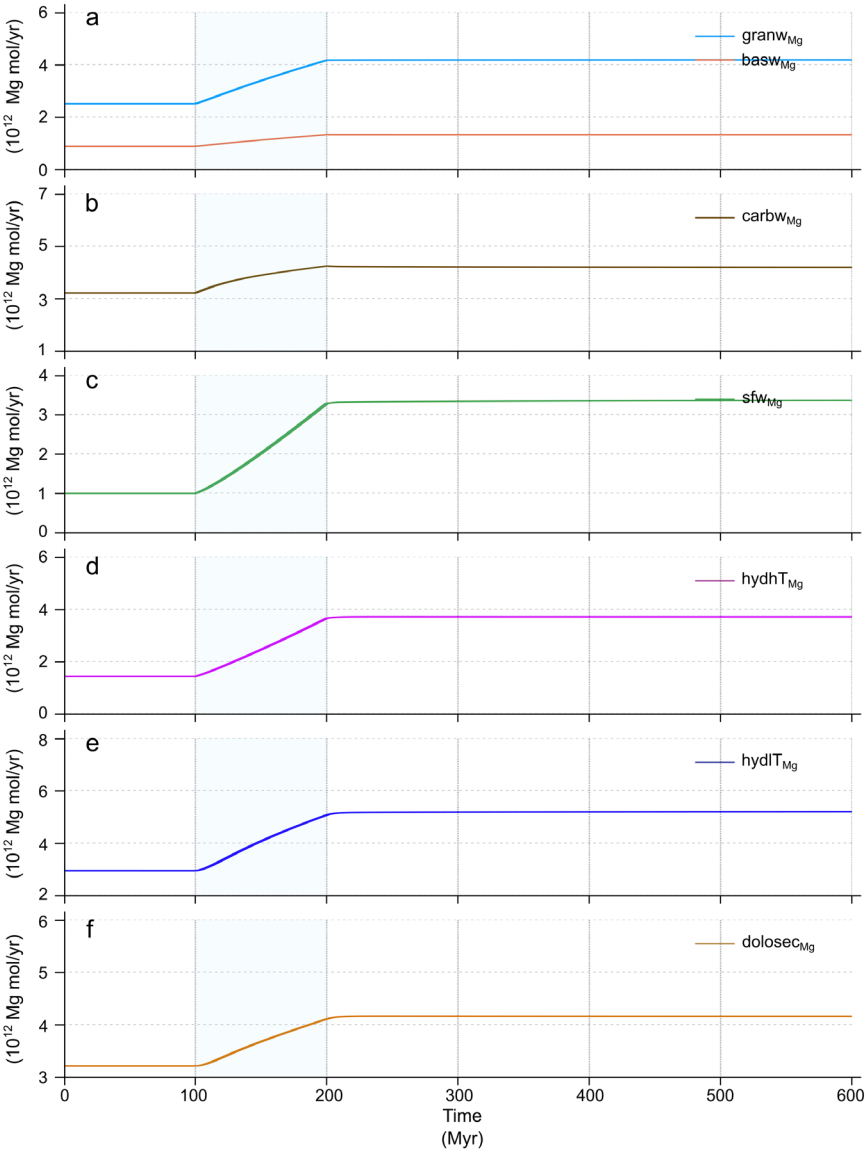

Figure C2: The changes of magnesium cycle fluxes towards DEGASS elevation. (a) silicate weathering (granite and basalt) Mg fluxes. (b) carbonate weathering Mg flux. (c) seafloor weathering Mg flux. (d) high-temperature hydrothermal Mg flux. (e) low-temperature hydrothermal Mg flux. (f) secondary dolomitization Mg flux.

835

https://doi.org/10.5194/egusphere-2026-2949
Preprint. Discussion started: 15 September 2026

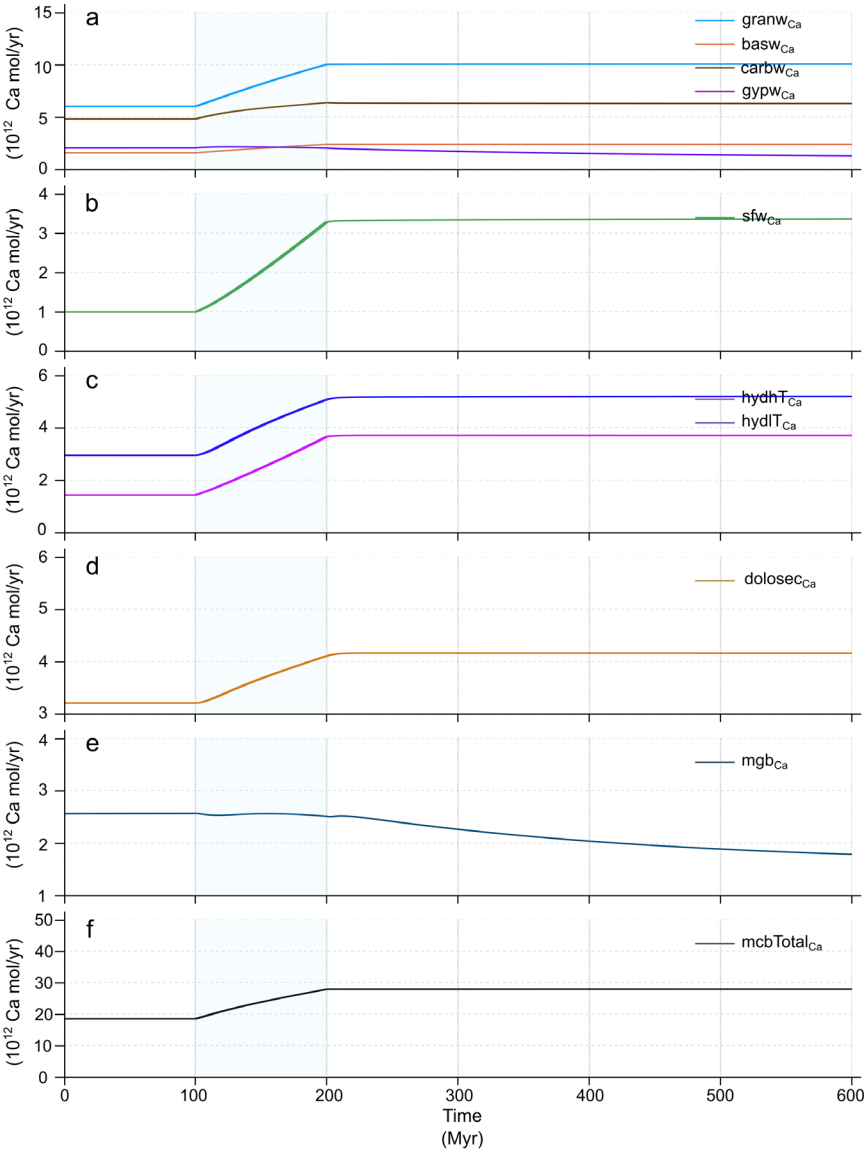

Figure C3: The changes of calcium cycle fluxes towards DEGASS elevation. (a) continental weathering (granite, basalt, carbonate and gypsum) Ca fluxes. (b) seafloor weathering Ca flux. (c) high- and low-temperature hydrothermal Ca fluxes. (d) secondary dolomitization Ca flux. (e) marine gypsum burial Ca flux. (f) marine total carbonate burial Ca flux.

840

https://doi.org/10.5194/egusphere-2026-2949
Preprint. Discussion started: 15 September 2026

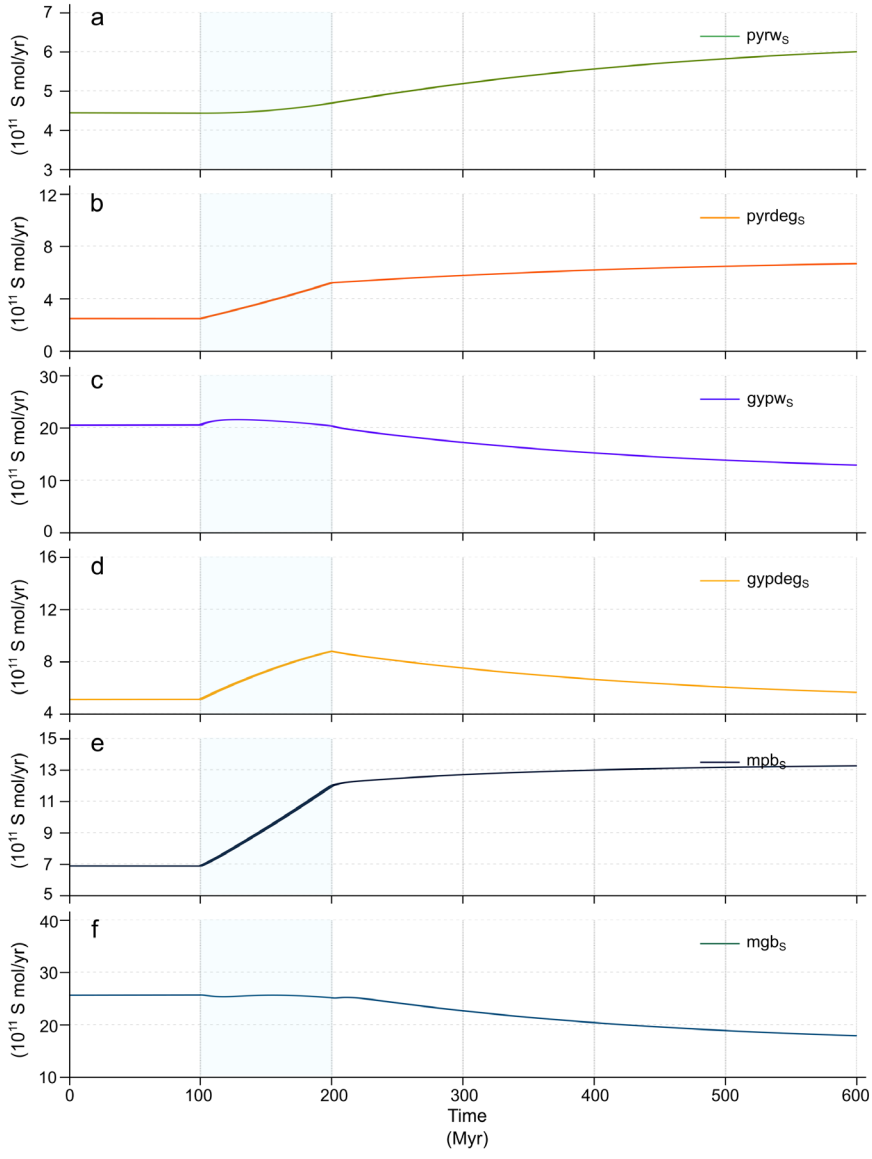

Figure C4: The changes of sulphur cycle fluxes towards DEGASS elevation. (a) pyrite weathering S flux. (b) pyrite degassing S flux. (c) gypsum weathering S flux. (d) gypsum degassing S flux. (e) marine pyrite burial S flux. (f) marine gypsum burial S flux.

845

https://doi.org/10.5194/egusphere-2026-2949
Preprint. Discussion started: 15 September 2026

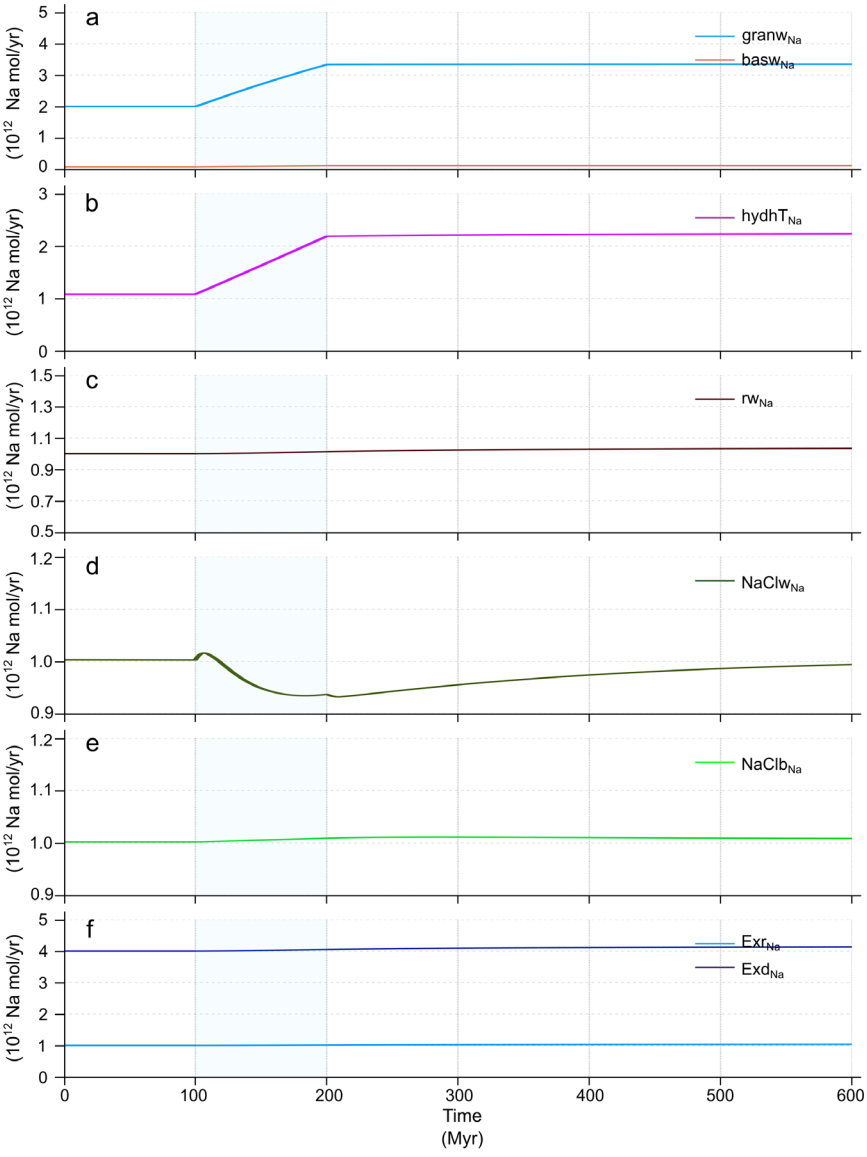

Figure C5: The changes of sodium cycle fluxes towards DEGASS elevation. (a) silicate weathering (granite and basalt) Na fluxes. (b) high-temperature hydrothermal Na flux. (c) reverse weathering Na flux. (d) NaCl weathering Na flux. (e) NaCl burial Na flux. (f) riverine and deep-sea cation exchange Na fluxes.

https://doi.org/10.5194/egusphere-2026-2949
Preprint. Discussion started: 15 September 2026

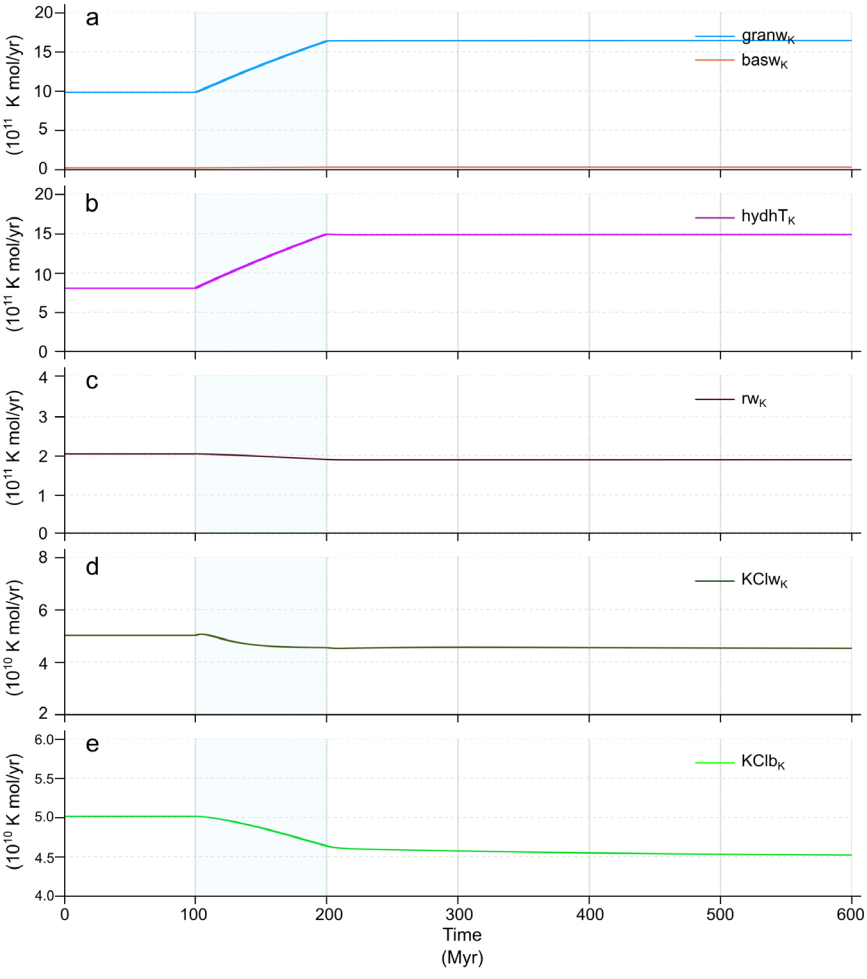

Figure C6: The changes of potassium cycle fluxes towards DEGASS elevation. (a) silicate weathering (granite and basalt) K fluxes. (b) high-temperature hydrothermal K flux. (c) reverse weathering K flux. (d) KCl weathering K flux. (e) KCl burial K flux.

https://doi.org/10.5194/egusphere-2026-2949
Preprint. Discussion started: 15 September 2026

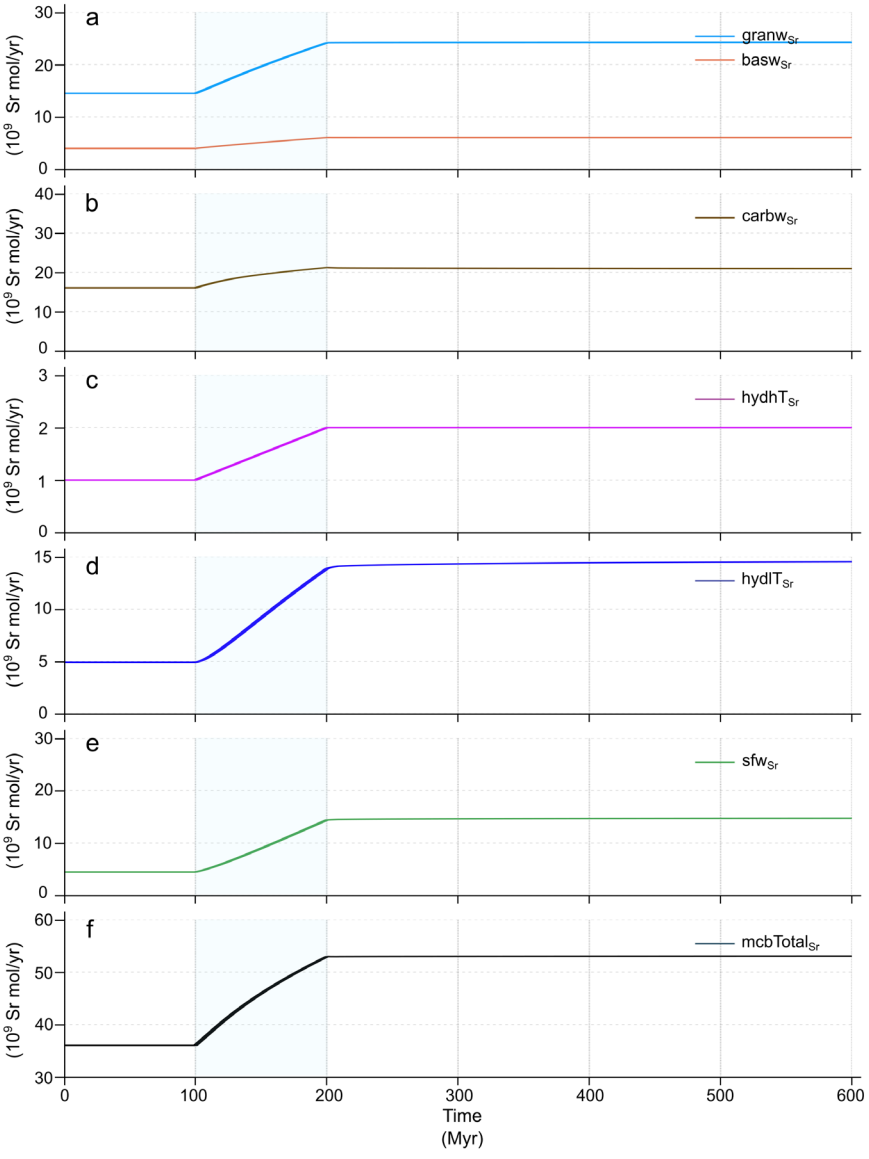

Figure C7: The changes of strontium cycle fluxes towards DEGASS elevation. (a) silicate weathering (granite and basalt) Sr fluxes. (b) carbonate weathering Sr flux. (c) high-temperature hydrothermal Sr flux. (d) low-temperature hydrothermal Sr flux. (e) seafloor weathering Sr flux. (f) marine carbonate burial Sr flux.

https://doi.org/10.5194/egusphere-2026-2949
Preprint. Discussion started: 15 September 2026

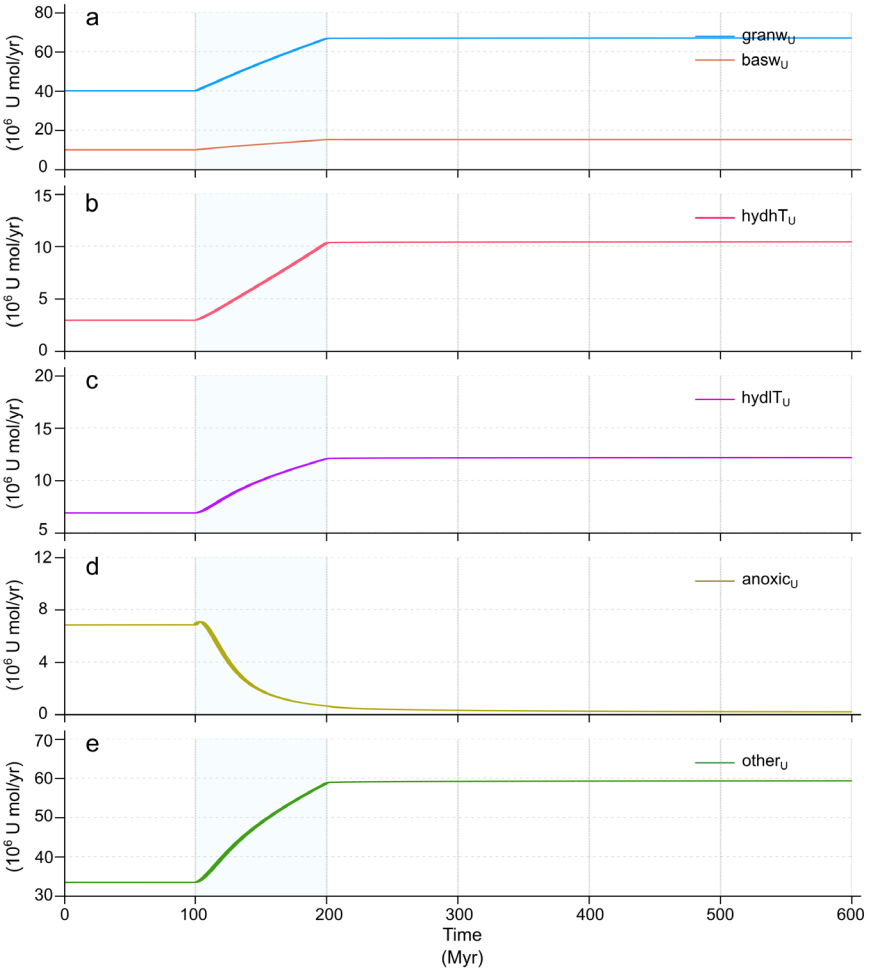

865 **Figure C8: The changes of uranium cycle fluxes towards DEGASS elevation.** (a) silicate weathering (granite and basalt) U fluxes. (b) anoxic burial U flux. (c) other burial U flux. (d) high-temperature hydrothermal U flux. (e) low-temperature hydrothermal U flux.

https://doi.org/10.5194/egusphere-2026-2949
Preprint. Discussion started: 15 September 2026

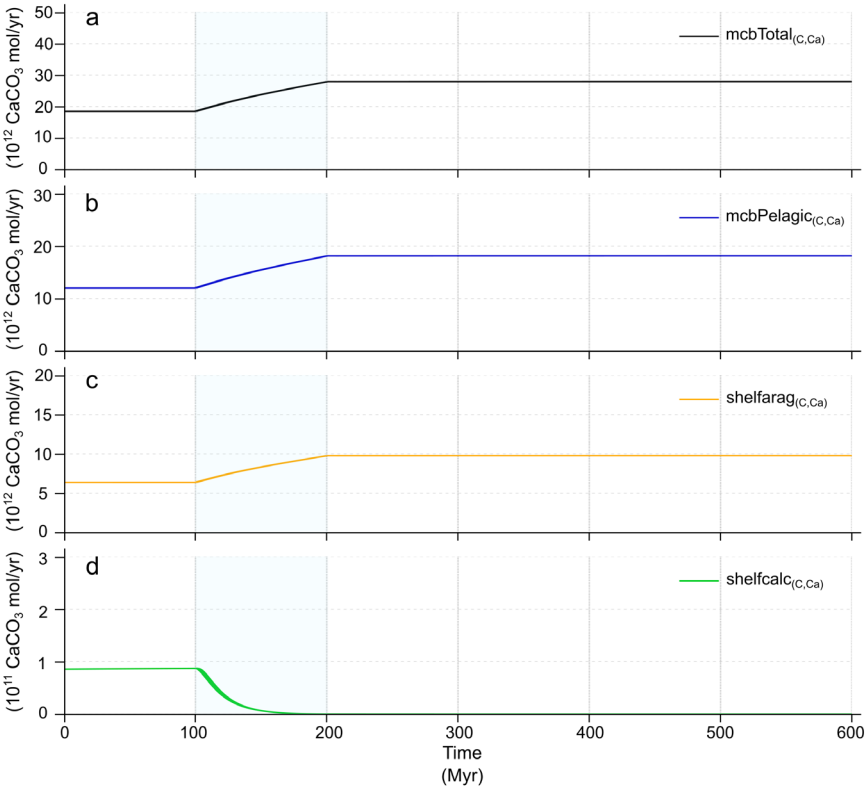

Figure C9: The changes of marine carbonate burial fluxes towards DEGASS elevation. (a) marine total carbonate burial flux. (b) pelagic carbonate burial flux. (c) shelf aragonite burial flux. (d) shelf calcite burial flux.

Code and data availability

The current TAlkEaSy model v1.0 is available from the website https://github.com/Chen-Xiyuan/POEM_TAlkEaSy_v1.0 under the MIT license. The frozen version to produce the results in this paper is archived on Zenodo at https://doi.org/10.5281/zenodo.20208350 (Chen and Lenton, 2026). The repository and files contain all configuration files, parameters, and diagnostic code for the simulations about the sensitivity tests in this paper.

Author contributions

XC developed the TAlkEaSy model from TML's COPSE. TML as 1st supervisor detailly guided Xiyuan's research directions and provided strong academic support and improvement for the paper. All authors contributed to writing this manuscript.

https://doi.org/10.5194/egusphere-2026-2949
Preprint. Discussion started: 15 September 2026

Competing interests

The authors declare no competing interests are present.

Acknowledgements

XC is funded by a China Scholarship Council-University of Exeter Scholarship. XC would like to thank Stuart J. Daines for the teaching of basic coding and box model configuration. The authors used ChatGPT for assistance in code organization and documentation.

Financial support

This research has been supported by the China Scholarship Council-University of Exeter Scholarship.

References

Adloff, M., Ridgwell, A., Monteiro, F. M., Parkinson, I. J., Dickson, A. J., Pogge von Strandmann, P. A. E., Fantle, M. S., and Greene, S. E.: Inclusion of a suite of weathering tracers in the cGENIE Earth system model – muffin release v.0.9.23, Geosci. Model Dev., 14, 4187–4223, https://doi.org/10.5194/gmd-14-4187-2021, 2021.

Alcott, L. J., Mills, B. J. W., and Poulton, S. W.: Stepwise Earth oxygenation is an inherent property of global biogeochemical cycling, Science, 366, 1333–1337, https://doi.org/10.1126/science.aax6459, 2019.

Alcott, L. J., Mills, B. J. W., Bekker, A., and Poulton, S. W.: Earth's Great Oxidation Event facilitated by the rise of sedimentary phosphorus recycling, Nat. Geosci., 15, 210–215, https://doi.org/10.1038/s41561-022-00906-5, 2022.

Alkattan, M., Oelkers, E. H., Dandurand, J.-L., and Schott, J.: Experimental studies of halite dissolution kinetics, 1. The effect of saturation state and the presence of trace metals, Chem. Geol., 137, 201–219, https://doi.org/10.1016/S0009-2541(96)00164-7, 1997.

Amini, M., Eisenhauer, A., Böhm, F., Fietzke, J., Bach, W., Garbe-Schönberg, D., Rosner, M., Bock, B., Lackschewitz, K. S., and Hauff, F.: Calcium isotope ($\delta^{44/40}$Ca) fractionation along hydrothermal pathways, Logatchev field (Mid-Atlantic Ridge, 14° 45′ N), Geochim. Cosmochim. Acta, 72, 4107–4122, https://doi.org/10.1016/j.gca.2008.05.055, 2008.

Antonelli, M. A. and Simon, J. I.: Calcium isotopes in high-temperature terrestrial processes, Chem. Geol., 548, 119651, https://doi.org/10.1016/j.chemgeo.2020.119651, 2020.

Arndt, S., Régnier, P., Goddéris, Y., and Donnadieu, Y.: GEOCLIM reloaded (v 1.0): A new coupled Earth system model for past climate change, Geosci. Model Dev., 4, 451–481, https://doi.org/10.5194/gmd-4-451-2011, 2011.

Arvidson, R., Mackenzie, F., and Guidry, M.: MAGic: A Phanerozoic model for the geochemical cycling of major rock-forming components, Am. J. Sci., 306, 135–190, https://doi.org/10.2475/ajs.306.3.135, 2006.

https://doi.org/10.5194/egusphere-2026-2949
Preprint. Discussion started: 15 September 2026

Arvidson, R. S., Mackenzie, F. T., and Guidry, M. W.: Geologic history of seawater: a MAGic approach to carbon chemistry and ocean ventilation, Chem. Geol., 362, 287–304, https://doi.org/10.1016/j.chemgeo.2013.10.012, 2013.

Barnum, T. P. and Coates, J. D.: The biogeochemical cycling of chlorine, Geobiology, 20, 634–649, https://doi.org/10.1111/gbi.12513, 2022.

Bartdorff, O., Wallmann, K., Latif, M., and Semenov, V.: Phanerozoic evolution of atmospheric methane, Global Biogeochem. Cycles, 22, https://doi.org/10.1029/2007GB002985, 2008.

Bergman, N. M., Lenton, T. M., and Watson, A. J.: COPSE: a new model of biogeochemical cycling over Phanerozoic time, Am. J. Sci., 304, 397–437, https://doi.org/10.2475/ajs.304.5.397, 2004.

Berner, R. A.: Models for carbon and sulfur cycles and atmospheric oxygen; application to Paleozoic geologic history, Am. J. Sci., 287, 177–196, https://doi.org/10.2475/ajs.287.3.177, 1987.

Berner, R. A.: A model for atmospheric CO_2 over Phanerozoic time, Am. J. Sci., 291, 339–376, https://doi.org/10.2475/ajs.291.4.339, 1991.

Berner, R. A.: GEOCARB II: A revised model of atmospheric CO_2 over Phanerozoic time, Am. J. Sci., 294, 56–91, https://doi.org/10.2475/ajs.294.1.56, 1994.

Berner, R. A.: A model for calcium, magnesium and sulfate in seawater over Phanerozoic time, Am. J. Sci., 304, 438–453, https://doi.org/10.2475/ajs.304.5.438, 2004.

Berner, R. A.: GEOCARBSULF: a combined model for Phanerozoic atmospheric O_2 and CO_2, Geochim. Cosmochim. Acta, 70, 5653–5664, https://doi.org/10.1016/j.gca.2005.11.032, 2006a.

Berner, R. A.: Inclusion of the weathering of volcanic rocks in the GEOCARBSULF model, Am. J. Sci., 306, 295–302, https://doi.org/10.2475/05.2006.01, 2006b.

Berner, R. A.: Phanerozoic atmospheric oxygen: New results using the GEOCARBSULF model, Am. J. Sci., 309, 603–606, https://doi.org/10.2475/07.2009.03, 2009.

Berner, R. A. and Kothavala, Z.: GEOCARB III: a revised model of atmospheric CO_2 over Phanerozoic time, Am. J. Sci., 301, 182–204, https://doi.org/10.2475/ajs.301.2.182, 2001.

Berner, R. A., Lasaga, A. C., and Garrels, R. M.: The carbonate-silicate geochemical cycle and its effect on atmospheric carbon dioxide over the past 100 million years, Am. J. Sci., 283, 641–683, https://doi.org/10.2475/ajs.283.7.641, 1983.

Blättler, C. L.: Examining uncertainties in major-ion reconstructions of seawater from halite fluid inclusions, Earth-Sci. Rev., 105142, https://doi.org/10.1016/j.earscirev.2025.105142, 2025.

Blättler, C. L., Jenkyns, H. C., Reynard, L. M., and Henderson, G. M.: Significant increases in global weathering during Oceanic Anoxic Events 1a and 2 indicated by calcium isotopes, Earth Planet. Sci. Lett., 309, 77–88, https://doi.org/10.1016/j.epsl.2011.06.029, 2011.

Blättler, C. L., Henderson, G. M., and Jenkyns, H. C.: Explaining the Phanerozoic Ca isotope history of seawater, Geology, 40, 843–846, https://doi.org/10.1130/G33191.1, 2012.

https://doi.org/10.5194/egusphere-2026-2949
Preprint. Discussion started: 15 September 2026

Cao, M., Daines, S. J., Lenton, T. M., Cui, H., Algeo, T. J., Dahl, T. W., Shi, W., Chen, Z.-Q., Anbar, A., and Zhou, Y.-Q.: Comparison of Ediacaran platform and slope $\delta^{238}U$ records in South China: Implications for global-ocean oxygenation and the origin of the Shuram Excursion, Geochim. Cosmochim. Acta, 287, 111–124, https://doi.org/10.1016/j.gca.2020.04.035, 2020.

Catling, D. C. and Zahnle, K. J.: The Archean atmosphere, Sci. Adv., 6, eaax1420, https://doi.org/10.1126/sciadv.aax1420, 2020.

Chen, X., Halloran, P. R., and Lenton, T. M.: Controls on the major ion composition and alkalinity of the ocean through the Phanerozoic, in preparation, 2026.

Chen, X. and Lenton, T. M.: POEM-TAlkEaSy v1.0: source code and input files for Chen and Lenton model description paper, Zenodo [code], https://doi.org/10.5281/zenodo.20208350, 2026.

Clarkson, M. O., Kasemann, S. A., Wood, R. A., Lenton, T. M., Daines, S. J., Richoz, S., Ohnemüller, F., Meixner, A., Poulton, S. W., and Tipper, E. T.: Ocean acidification and the Permo-Triassic mass extinction, Science, 348, 229–232, https://doi.org/10.1126/science.aaa0193, 2015.

Clarkson, M. O., Stirling, C. H., Jenkyns, H. C., Dickson, A. J., Porcelli, D., Moy, C. M., Pogge von Strandmann, P. A. E., Cooke, I. R., and Lenton, T. M.: Uranium isotope evidence for two episodes of deoxygenation during Oceanic Anoxic Event 2, Proc. Natl. Acad. Sci., 115, 2918–2923, https://doi.org/10.1073/pnas.1715278115, 2018.

Clarkson, M. O., Lenton, T. M., Andersen, M. B., Bagard, M.-L., Dickson, A. J., and Vance, D.: Upper limits on the extent of seafloor anoxia during the PETM from uranium isotopes, Nat. Commun., 12, 399, https://doi.org/10.1038/s41467-020-20486-5, 2021.

Coogan, L. A. and Dosso, S. E.: Alteration of ocean crust provides a strong temperature dependent feedback on the geological carbon cycle and is a primary driver of the Sr-isotopic composition of seawater, Earth Planet. Sci. Lett., 415, 38–46, https://doi.org/10.1016/j.epsl.2015.01.027, 2015.

Coogan, L. A., Turchyn, A. V., Dunlea, A. G., and Bach, W.: A brief introduction to potential links and feedbacks between hydrothermal processes and seawater chemistry, in: Hydrothermal Circulation and Seawater Chemistry: Links and Feedbacks, 1–18, https://doi.org/10.1002/9781394229185.ch1, 2025.

Dahl, T. W., Boyle, R. A., Canfield, D. E., Connelly, J. N., Gill, B. C., Lenton, T. M., and Bizzarro, M.: Uranium isotopes distinguish two geochemically distinct stages during the later Cambrian SPICE event, Earth Planet. Sci. Lett., 401, 313–326, https://doi.org/10.1016/j.epsl.2014.05.043, 2014.

Demicco, R. V., Lowenstein, T. K., Hardie, L. A., and Spencer, R. J.: Model of seawater composition for the Phanerozoic, Geology, 33, 877–880, https://doi.org/10.1130/G21945.1, 2005.

Dodd, M. S., Shi, W., Li, C., Zhang, Z., Cheng, M., Chen, H., Hardisty, D. S., Loyd, S. J., Wallace, M. W., Hood, A. v. S., Lamothe, K., Mills, B. J. W., Poulton, S. W., and Lyons, T. W.: Uncovering the Ediacaran phosphorus cycle, Nature, 618, 974–980, https://doi.org/10.1038/s41586-023-06077-6, 2023.

Donnadieu, Y., Goddéris, Y., Ramstein, G., Nédélec, A., and Meert, J.: A 'snowball Earth' climate triggered by continental break-up through changes in runoff, Nature, 428, 303–306, https://doi.org/10.1038/nature02408, 2004.

https://doi.org/10.5194/egusphere-2026-2949
Preprint. Discussion started: 15 September 2026

Evans, D., Rosenthal, Y., Erez, J., Hauzer, H., Cotton, L. J., Zhou, X., Nambiar, R., Stassen, P., Pearson, P. N., Renema, W., Saraswati, P. K., Todd, J. A., Müller, W., and Affek, H. P.: The major ion chemistry of seawater was closely coupled to the long-term carbon cycle during the Cenozoic, Proc. Natl. Acad. Sci., 123, e2511781122, https://doi.org/10.1073/pnas.2511781122, 2026.

Fakhraee, M., Bauer, K. W., Planavsky, N. J., Reinhard, C. T., and Crowe, S. A.: Climate stabilization by alkalinity production from pyrite burial during oceanic anoxia, Nat. Geosci., 18, 495–502, https://doi.org/10.1038/s41561-025-01698-0, 2025.

Fantle, M. S. and Ridgwell, A.: Towards an understanding of the Ca isotopic signal related to ocean acidification and alkalinity overshoots in the rock record, Chem. Geol., 547, 119672, https://doi.org/10.1016/j.chemgeo.2020.119672, 2020.

Fantle, M. S. and Tipper, E. T.: Calcium isotopes in the global biogeochemical Ca cycle: Implications for development of a Ca isotope proxy, Earth-Sci. Rev., 129, 148–177, https://doi.org/10.1016/j.earscirev.2013.10.004, 2014.

Farkaš, J., Böhm, F., Wallmann, K., Blenkinsop, J., Eisenhauer, A., Van Geldern, R., Munnecke, A., Voigt, S., and Veizer, J.: Calcium isotope record of Phanerozoic oceans: Implications for chemical evolution of seawater and its causative mechanisms, Geochim. Cosmochim. Acta, 71, 5117–5134, https://doi.org/10.1016/j.gca.2007.09.004, 2007.

Fisher, A. T. and Wheat, C. G.: Seamounts as conduits for massive fluid, heat, and solute fluxes on ridge flanks, Oceanography, 23, 74–87, https://doi.org/10.5670/oceanog.2010.63, 2010.

Foster, G. L., Royer, D. L., and Lunt, D. J.: Future climate forcing potentially without precedent in the last 420 million years, Nat. Commun., 8, 14845, https://doi.org/10.1038/ncomms14845, 2017.

Garrels, R. M. and Lerman, A.: Phanerozoic cycles of sedimentary carbon and sulfur, Proc. Natl. Acad. Sci., 78, 4652–4656, https://doi.org/10.1073/pnas.78.8.4652, 1981.

Garrels, R. M. and Lerman, A.: Coupling of the sedimentary sulfur and carbon cycles; an improved model, Am. J. Sci., 284, 989–1007, https://doi.org/10.2475/ajs.284.9.989, 1984.

Goddéris, Y., Donnadieu, Y., Le Hir, G., Lefebvre, V., and Nardin, E.: The role of palaeogeography in the Phanerozoic history of atmospheric CO2 and climate, Earth-Sci. Rev., 128, 122–138, https://doi.org/10.1016/j.earscirev.2013.11.004, 2014.

Goddéris, Y., Donnadieu, Y., Carretier, S., Aretz, M., Dera, G., Macouin, M., and Regard, V.: Onset and ending of the late Palaeozoic ice age triggered by tectonically paced rock weathering, Nat. Geosci., 10, 382–386, https://doi.org/10.1038/ngeo2931, 2017.

Guo, M. and Korenaga, J.: Rapid rise of early ocean pH under elevated weathering rates, Nat. Geosci., https://doi.org/10.1038/s41561-025-01649-9, 2025.

Gurung, K., Field, K. J., Batterman, S. A., Goddéris, Y., Donnadieu, Y., Porada, P., Taylor, L. L., and Mills, B. J. W.: Climate windows of opportunity for plant expansion during the Phanerozoic, Nat. Commun., 13, 4530, https://doi.org/10.1038/s41467-022-32077-7, 2022.

Gussone, N., Böhm, F., Eisenhauer, A., Dietzel, M., Heuser, A., Teichert, B. M., Reitner, J., Wörheide, G., and Dullo, W.-C.: Calcium isotope fractionation in calcite and aragonite, Geochim. Cosmochim. Acta, 69, 4485–4494, https://doi.org/10.1016/j.gca.2005.06.003, 2005.

https://doi.org/10.5194/egusphere-2026-2949
Preprint. Discussion started: 15 September 2026

Gussone, N., Schmitt, A.-D., Heuser, A., Wombacher, F., Dietzel, M., Tipper, E., Schiller, M., and Böhm, F.: Calcium stable isotope geochemistry, Springer, Berlin, Heidelberg, https://doi.org/10.1007/978-3-540-68953-9, 2016.

Gussone, N., Ahm, A.-S. C., Lau, K. V., and Bradbury, H. J.: Calcium isotopes in deep time: potential and limitations, Chem. Geol., 544, 119601, https://doi.org/10.1016/j.chemgeo.2020.119601, 2020.

Halevy, I. and Bachan, A.: The geologic history of seawater pH, Science, 355, 1069–1071, https://doi.org/10.1126/science.aal4151, 2017.

Handoh, I. C. and Lenton, T. M.: Periodic mid-Cretaceous oceanic anoxic events linked by oscillations of the phosphorus and oxygen biogeochemical cycles, Global Biogeochem. Cycles, 17, https://doi.org/10.1029/2003GB002039, 2003.

Hansen, K. W. and Wallmann, K.: Cretaceous and Cenozoic evolution of seawater composition, atmospheric O2 and CO2: a model perspective, Am. J. Sci., 303, 94–148, https://doi.org/10.2475/ajs.303.2.94, 2003.

Hardie, L. A.: Secular variation in seawater chemistry: An explanation for the coupled secular variation in the mineralogies of marine limestones and potash evaporites over the past 600 m.y., Geology, 24, 279–283, https://doi.org/10.1130/0091-7613(1996)024<0279:SVISCA>2.3.CO;2, 1996.

Harouaka, K., Eisenhauer, A., and Fantle, M. S.: Experimental investigation of Ca isotopic fractionation during abiotic gypsum precipitation, Geochim. Cosmochim. Acta, 129, 157–176, https://doi.org/10.1016/j.gca.2013.12.004, 2014.

Hashim, M. S. and Kaczmarek, S. E.: The transformation of aragonite to calcite in the presence of magnesium: Implications for marine diagenesis, Earth Planet. Sci. Lett., 574, 117166, https://doi.org/10.1016/j.epsl.2021.117166, 2021.

Higgins, J. A. and Schrag, D. P.: The Mg isotopic composition of Cenozoic seawater–evidence for a link between Mg-clays, seawater Mg/Ca, and climate, Earth Planet. Sci. Lett., 416, 73–81, https://doi.org/10.1016/j.epsl.2015.01.003, 2015.

Higgins, J. A., Blättler, C. L., Lundstrom, E., Santiago-Ramos, D., Akhtar, A., Ahm, A.-S. C., Bialik, O., Holmden, C., Bradbury, H., Murray, S. T., and Swart, P. K.: Mineralogy, early marine diagenesis, and the chemistry of shallow-water carbonate sediments, Geochim. Cosmochim. Acta, 220, 512–534, https://doi.org/10.1016/j.gca.2017.09.046, 2018.

Holden, P. B., Edwards, N. R., Müller, S. A., Oliver, K. I. C., Death, R. M., and Ridgwell, A.: Controls on the spatial distribution of oceanic δ13CDIC, Biogeosciences, 10, 1815–1833, https://doi.org/10.5194/bg-10-1815-2013, 2013.

Holland, H. D.: Sea level, sediments and the composition of seawater, Am. J. Sci., 305, 220–239, https://doi.org/10.2475/ajs.305.3.220, 2005.

Horne, J. and Goldblatt, C.: EONS: A new biogeochemical model of Earth's oxygen, carbon, phosphorus, and nitrogen systems from the Archean to the present, Geochem. Geophys. Geosyst., 25, e2023GC011252, https://doi.org/10.1029/2023GC011252, 2024.

Isson, T. T. and Planavsky, N. J.: Reverse weathering as a long-term stabilizer of marine pH and planetary climate, Nature, 560, 471–475, https://doi.org/10.1038/s41586-018-0408-4, 2018.

Kemeny, P. C., Krause, A. J., and Kump, L. R.: A historical perspective on long-term global biogeochemical box models, in: Hydrothermal Circulation and Seawater Chemistry: Links and Feedbacks, 263–295, https://doi.org/10.1002/9781394229185.ch12, 2025.

https://doi.org/10.5194/egusphere-2026-2949
Preprint. Discussion started: 15 September 2026

Kim, J., Kimura, Y., Puchala, B., Yamazaki, T., Becker, U., and Sun, W.: Dissolution enables dolomite crystal growth near ambient conditions, Science, 382, 915–920, https://doi.org/10.1126/science.adi3690, 2023.

Komar, N. and Zeebe, R. E.: Oceanic calcium changes from enhanced weathering during the Paleocene-Eocene thermal maximum: No effect on calcium-based proxies, Paleoceanography, 26, https://doi.org/10.1029/2010PA001979, 2011.

Komar, N. and Zeebe, R. E.: Calcium and calcium isotope changes during carbon cycle perturbations at the end-Permian, Paleoceanography, 31, 115–130, https://doi.org/10.1002/2015PA002834, 2016.

Krause, A. J., Mills, B. J. W., Zhang, S., Planavsky, N. J., Lenton, T. M., and Poulton, S. W.: Stepwise oxygenation of the Paleozoic atmosphere, Nat. Commun., 9, 4081, https://doi.org/10.1038/s41467-018-06383-y, 2018.

Krause, A. J., Mills, B. J. W., Merdith, A. S., Lenton, T. M., and Poulton, S. W.: Extreme variability in atmospheric oxygen levels in the late Precambrian, Sci. Adv., 8, eabm8191, https://doi.org/10.1126/sciadv.abm8191, 2022.

Krause, A. J., Shields, G. A., Newton, R. J., and Mills, B. J. W.: Modelling sulfate concentrations in the global ocean through Phanerozoic time, J. Geol. Soc., 181, https://doi.org/10.1144/jgs2023-184, 2024.

Krissansen-Totton, J., Arney, G. N., and Catling, D. C.: Constraining the climate and ocean pH of the early Earth with a geological carbon cycle model, Proc. Natl. Acad. Sci., 115, 4105–4110, https://doi.org/10.1073/pnas.1721296115, 2018.

Kump, L. R.: Alternative modeling approaches to the geochemical cycles of carbon, sulfur, and strontium isotopes, Am. J. Sci., 289, 390–410, https://doi.org/10.2475/ajs.289.4.390, 1989.

Kump, L. R.: Revising the textbook on the geologic carbon cycle and climate regulation, Elements, 22, 64–65, https://doi.org/10.2138/gselements.22.1.64, 2026.

Kump, L. R. and Garrels, R. M.: Modeling atmospheric O_2 in the global sedimentary redox cycle, Am. J. Sci., 286, 337–360, https://doi.org/10.2475/ajs.286.5.337, 1986.

Lafay, R., Baumgartner, L. P., Stephane, S., Suzanne, P., German, M.-H., and Torsten, V.: Petrologic and stable isotopic studies of a fossil hydrothermal system in ultramafic environment (Chenaillet ophicalcites, Western Alps, France): Processes of carbonate cementation, Lithos 294–295, 319–338, https://doi.org/10.1016/j.lithos.2017.10.006, 2017.

Lasaga, A. C., Berner, R. A., and Garrels, R. M.: An improved geochemical model of atmospheric CO_2 fluctuations over the past 100 million years, in: The Carbon Cycle and Atmospheric CO_2: Natural Variations Archean to Present, Geophysical Monograph Series, pp. 397–411, https://doi.org/10.1029/GM032p0397, 1985.

Lau, K. V., Romaniello, S. J., and Zhang, F.: The Uranium Isotope Paleoredox Proxy, Cambridge University Press, Cambridge, https://doi.org/10.1017/9781108584142, 2019.

Lenton, T. M. and Watson, A. J.: Redfield revisited: 1. Regulation of nitrate, phosphate, and oxygen in the ocean, Global Biogeochem. Cycles, 14, 225–248, https://doi.org/10.1029/1999GB900065, 2000a.

Lenton, T. M. and Watson, A. J.: Redfield revisited: 2. What regulates the oxygen content of the atmosphere?, Global Biogeochem. Cycles, 14, 249–268, https://doi.org/10.1029/1999GB900076, 2000b.

https://doi.org/10.5194/egusphere-2026-2949
Preprint. Discussion started: 15 September 2026

Lenton, T. M., Dahl, T. W., Daines, S. J., Mills, B. J. W., Ozaki, K., Saltzman, M. R., and Porada, P.: Earliest land plants created modern levels of atmospheric oxygen, Proc. Natl. Acad. Sci., 113, 9704–9709, https://doi.org/10.1073/pnas.1604787113, 2016.

Lenton, T. M., Daines, S. J., and Mills, B. J. W.: COPSE reloaded: an improved model of biogeochemical cycling over Phanerozoic time, Earth-Sci. Rev., 178, 1–28, https://doi.org/10.1016/j.earscirev.2017.12.004, 2018.

Li, W., Beard, B. L., Li, C., Xu, H., and Johnson, C. M.: Experimental calibration of Mg isotope fractionation between dolomite and aqueous solution and its geological implications, Geochim. Cosmochim. Acta, 157, 164–181, https://doi.org/10.1016/j.gca.2015.02.024, 2015.

Li, Z.-H., Lenton, T. M., Zhang, F.-F., Chen, Z.-Q., and Daines, S. J.: Earth system instability amplified biogeochemical oscillations following the end-Permian mass extinction, Nat. Commun., 16, 3703, https://doi.org/10.1038/s41467-025-59038-0, 2025.

Li, Z.-H., Chen, Z.-Q., Daines, S. J., Zhang, F., and Lenton, T. M.: Periodic ocean oxygenation events during the mid-Ediacaran, Nat. Geosci., 19, 216–222, https://doi.org/10.1038/s41561-025-01883-1, 2026.

Ligi, M., Bonatti, E., Cuffaro, M., and Brunelli, D.: Post-Mesozoic rapid increase of seawater Mg/Ca due to enhanced mantle-seawater interaction, Sci. Rep., 3, 2752, https://doi.org/10.1038/srep02752, 2013.

Liu, S.-T. and Nancollas, G. H.: The kinetics of dissolution of calcium sulfate dihydrate, J. Inorg. Nucl. Chem., 33, 2311–2316, https://doi.org/10.1016/0022-1902(71)80205-1, 1971.

Lopes, A. and Farelo, F.: Growth kinetics of potassium chloride—I: Pure aqueous solutions, J. Cryst. Growth, 290, 213–219, https://doi.org/10.1016/j.jcrysgro.2006.01.016, 2006.

Maffre, P., Goddéris, Y., Le Hir, G., Nardin, É., Sarr, A.-C., and Donnadieu, Y.: GEOCLIM7, an Earth system model for multi-million-year evolution of the geochemical cycles and climate, Geosci. Model Dev., 18, 6367–6413, https://doi.org/10.5194/gmd-18-6367-2025, 2025.

Merdith, A. S., Gernon, T. M., Maffre, P., Donnadieu, Y., Goddéris, Y., Longman, J., Müller, R. D., and Mills, B. J. W.: Phanerozoic icehouse climates as the result of multiple solid-Earth cooling mechanisms, Sci. Adv., 11, eadm9798, https://doi.org/10.1126/sciadv.adm9798, 2025.

Mills, B. J. W., Daines, S. J., and Lenton, T. M.: Changing tectonic controls on the long-term carbon cycle from Mesozoic to present, Geochem. Geophys. Geosyst., 15, 4866–4884, https://doi.org/10.1002/2014GC005530, 2014a.

Mills, B. J. W., Lenton, T. M., and Watson, A. J.: Proterozoic oxygen rise linked to shifting balance between seafloor and terrestrial weathering, Proc. Natl. Acad. Sci., 111, 9073–9078, https://doi.org/10.1073/pnas.1321679111, 2014b.

Mills, B. J. W., Scotese, C. R., Walding, N. G., Shields, G. A., and Lenton, T. M.: Elevated CO_2 degassing rates prevented the return of Snowball Earth during the Phanerozoic, Nat. Commun., 8, 1110, https://doi.org/10.1038/s41467-017-01456-w, 2017.

Mills, B. J. W., Donnadieu, Y., and Goddéris, Y.: Spatial continuous integration of Phanerozoic global biogeochemistry and climate, Gondwana Res., 100, 73–86, https://doi.org/10.1016/j.gr.2021.02.011, 2021.

https://doi.org/10.5194/egusphere-2026-2949
Preprint. Discussion started: 15 September 2026

Mills, B. J. W., Krause, A. J., Jarvis, I., and Cramer, B. D.: Evolution of atmospheric O_2 through the Phanerozoic, revisited, Annu. Rev. Earth Planet. Sci., 51, 253–276, https://doi.org/10.1146/annurev-earth-032320-095425, 2023.

Mills, B. J. W., Le Hir, G., Merdith, A., Gurung, K., Bowyer, F. T., Krause, A. J., Sanchez-Baracaldo, P., Hunter, S. J., and Zhang, Y.: Exploring Neoproterozoic climate and biogeochemical evolution in the SCION model, Glob. Planet. Change, 104791, https://doi.org/10.1016/j.gloplacha.2025.104791, 2025.

Ozaki, K., Tajima, S., and Tajika, E.: Conditions required for oceanic anoxia/euxinia: Constraints from a one-dimensional ocean biogeochemical cycle model, Earth Planet. Sci. Lett., 304, 270–279, https://doi.org/10.1016/j.epsl.2011.02.011, 2011.

Ozaki, K., Reinhard, C. T., and Tajika, E.: A sluggish mid-Proterozoic biosphere and its effect on Earth's redox balance, Geobiology, 17, 3–11, https://doi.org/10.1111/gbi.12317, 2019.

Ozaki, K., Cole, D. B., Reinhard, C. T., and Tajika, E.: CANOPS-GRB v1.0: a new Earth system model for simulating the evolution of ocean–atmosphere chemistry over geologic timescales, Geosci. Model Dev., 15, 7593–7639, https://doi.org/10.5194/gmd-15-7593-2022, 2022.

Payne, J. L., Turchyn, A. V., Paytan, A., DePaolo, D. J., Lehrmann, D. J., Yu, M., and Wei, J.: Calcium isotope constraints on the end-Permian mass extinction, Proc. Natl. Acad. Sci., 107, 8543–8548, https://doi.org/10.1073/pnas.0914065107, 2010.

Pearce, C. R., Parkinson, I. J., Gaillardet, J., Charlier, B. L. A., Mokadem, F., and Burton, K. W.: Reassessing the stable (δ88/86Sr) and radiogenic (87Sr/86Sr) strontium isotopic composition of marine inputs, Geochim. Cosmochim. Acta, 157, 125–146, https://doi.org/10.1016/j.gca.2015.02.029, 2015.

Porter, S. M.: Seawater chemistry and early carbonate biomineralization, Science, 316, 1302, https://doi.org/10.1126/science.1137284, 2007.

Ridgwell, A., Hargreaves, J. C., Edwards, N. R., Annan, J. D., Lenton, T. M., Marsh, R., Yool, A., and Watson, A.: Marine geochemical data assimilation in an efficient Earth System Model of global biogeochemical cycling, Biogeosciences, 4, 87–104, https://doi.org/10.5194/bg-4-87-2007, 2007.

Royer, D. L., Donnadieu, Y., Park, J., Kowalczyk, J., and Goddéris, Y.: Error analysis of CO_2 and O_2 estimates from the long-term geochemical model GEOCARBSULF, Am. J. Sci., 314, 1259–1283, https://doi.org/10.2475/09.2014.01, 2014.

Shalev, N., Bontognali, T. R., Wheat, C. G., and Vance, D.: New isotope constraints on the Mg oceanic budget point to cryptic modern dolomite formation, Nat. Commun., 10, 5646, https://doi.org/10.1038/s41467-019-13514-6, 2019.

Sharoni, S. and Halevy, I.: Rates of seafloor and continental weathering govern Phanerozoic marine phosphate levels, Nat. Geosci., 16, 75–81, https://doi.org/10.1038/s41561-022-01075-1, 2023.

Shields, G. A. and Mills, B. J. W.: Evaporite weathering and deposition as a long-term climate forcing mechanism, Geology, 49, 299–303, https://doi.org/10.1130/G48146.1, 2021.

Shields, G. A., Mills, B. J. W., Zhu, M., Raub, T. D., Daines, S. J., and Lenton, T. M.: Unique Neoproterozoic carbon isotope excursions sustained by coupled evaporite dissolution and pyrite burial, Nat. Geosci., 12, 823–827, https://doi.org/10.1038/s41561-019-0434-3, 2019.

https://doi.org/10.5194/egusphere-2026-2949
Preprint. Discussion started: 15 September 2026

Stanley, S. M.: Influence of seawater chemistry on biomineralization throughout Phanerozoic time: Paleontological and experimental evidence, Palaeogeogr. Palaeoclimatol. Palaeoecol., 232, 214–236, https://doi.org/10.1016/j.palaeo.2005.12.010, 2006.

Sun, W., Jayaraman, S., Chen, W., Persson, K. A., and Ceder, G.: Nucleation of metastable aragonite $CaCO_3$ in seawater, Proc. Natl. Acad. Sci., 112, 3199–3204, https://doi.org/10.1073/pnas.1423898112, 2015.

Sun, X., Higgins, J., and Turchyn, A. V.: Diffusive cation fluxes in deep-sea sediments and insight into the global geochemical cycles of calcium, magnesium, sodium and potassium, Mar. Geol., 373, 64–77, https://doi.org/10.1016/j.margeo.2015.12.011, 2016.

Teng, F.-Z.: Magnesium isotope geochemistry, Rev. Mineral. Geochem., 82, 219–287, https://doi.org/10.2138/rmg.2017.82.7, 2017.

Timofeeff, M. N., Lowenstein, T. K., Brennan, S. T., Demicco, R. V., Zimmermann, H., Horita, J., and von Borstel, L. E.: Evaluating seawater chemistry from fluid inclusions in halite: examples from modern marine and nonmarine environments, Geochim. Cosmochim. Acta, 65, 2293–2300, https://doi.org/10.1016/S0016-7037(01)00591-9, 2001.

Tipper, E. T., Stevenson, E. I., Alcock, V., Knight, A. C., Baronas, J. J., Hilton, R. G., Bickle, M. J., Larkin, C. S., Feng, L., and Relph, K. E.: Global silicate weathering flux overestimated because of sediment–water cation exchange, Proc. Natl. Acad. Sci., 118, e2016430118, https://doi.org/10.1073/pnas.2016430118, 2021.

Tostevin, R. and Mills, B. J. W.: Reconciling proxy records and models of Earth's oxygenation during the Neoproterozoic and Palaeozoic, Interface Focus, 10, 20190137, https://doi.org/10.1098/rsfs.2019.0137, 2020.

Turchyn, A. V. and DePaolo, D. J.: Seawater chemistry through Phanerozoic time, Annu. Rev. Earth Planet. Sci., 47, 197–224, https://doi.org/10.1146/annurev-earth-082517-010305, 2019.

van de Velde, S. J., Hülse, D., Reinhard, C. T., and Ridgwell, A.: Iron and sulfur cycling in the cGENIE.muffin Earth system model (v0.9.21), Geosci. Model Dev., 14, 2713–2745, https://doi.org/10.5194/gmd-14-2713-2021, 2021.

Wallmann, K.: Controls on the Cretaceous and Cenozoic evolution of seawater composition, atmospheric CO_2 and climate, Geochim. Cosmochim. Acta, 65, 3005–3025, https://doi.org/10.1016/S0016-7037(01)00638-X, 2001.

Wang, Y., He, Y., Wu, H., Zhu, C., Huang, S., and Huang, J.: Calcium isotope fractionation during crustal melting and magma differentiation: Granitoid and mineral-pair perspectives, Geochim. Cosmochim. Acta, 259, 37–52, https://doi.org/10.1016/j.gca.2019.05.030, 2019.

Witkowski, C. R., Weijers, J. W. H., Blais, B., Schouten, S., and Sinninghe Damsté, J. S.: Molecular fossils from phytoplankton reveal secular PCO2 trend over the Phanerozoic, Sci. Adv., 4, eaat4556, https://doi.org/10.1126/sciadv.aat4556, 2018.

Xia, Z., Li, S., Hu, Z., Bialik, O., Chen, T., Weldeghebriel, M. F., Fan, Q., Fan, J., Wang, X., and An, S.: The evolution of Earth's surficial Mg cycle over the past 2 billion years, Sci. Adv., 10, eadj5474, https://doi.org/10.1126/sciadv.adj5474, 2024.

Zeebe, R. E.: LOSCAR: Long-term ocean-atmosphere-sediment carbon cycle reservoir model v2.0.4, Geosci. Model Dev., 5, 149–166, https://doi.org/10.5194/gmd-5-149-2012, 2012a.

https://doi.org/10.5194/egusphere-2026-2949
Preprint. Discussion started: 15 September 2026

Zeebe, R. E.: History of seawater carbonate chemistry, atmospheric CO_2, and ocean acidification, Annu. Rev. Earth Planet. Sci., 40, 141–165, https://doi.org/10.1146/annurev-earth-042711-105521, 2012b.

Zeebe, R. E. and Wolf-Gladrow, D.: CO_2 in seawater: equilibrium, kinetics, isotopes, Elsevier Oceanography Series, 65, Elsevier, Amsterdam, 2001.

Zhang, S., Planavsky, N. J., Krause, A. J., Bolton, E. W., and Mills, B. J. W.: Model based Paleozoic atmospheric oxygen estimates: a revisit to GEOCARBSULF, Am. J. Sci., 318, 557–589, https://doi.org/10.2475/05.2018.05, 2018.

Zhang, F., Lenton, T. M., del Rey, Á., Romaniello, S. J., Chen, X., Planavsky, N. J., Clarkson, M. O., Dahl, T. W., Lau, K. V., and Wang, W.: Uranium isotopes in marine carbonates as a global ocean paleoredox proxy: a critical review, Geochim. Cosmochim. Acta, 287, 27–49, https://doi.org/10.1016/j.gca.2020.05.011, 2020a.

Zhang, F., Shen, S., Cui, Y., Lenton, T. M., Dahl, T. W., Zhang, H., Zheng, Q., Wang, W., Krainer, K., and Anbar, A. D.: Two distinct episodes of marine anoxia during the Permian-Triassic crisis evidenced by uranium isotopes in marine dolostones, Geochim. Cosmochim. Acta, 287, 165–179, https://doi.org/10.1016/j.gca.2020.01.032, 2020b.

Zhao, M., Mills, B. J. W., Homoky, W. B., and Peacock, C. L.: Oxygenation of the Earth aided by mineral–organic carbon preservation, Nat. Geosci., 16, 262–267, https://doi.org/10.1038/s41561-023-01133-2, 2023.

Zhao, M., Mills, B. J. W., Poulton, S. W., Wan, B., Xiao, K.-Q., Guo, L., and Guo, Z.: Drivers of the global phosphorus cycle over geological time, Nat. Rev. Earth Environ., 5, 873–889, https://doi.org/10.1038/s43017-024-00603-4, 2024.

Zhong, Y., Li, Z., Shi, X., Isson, T., Yu, J., Kender, S., Liang, Z., Swann, G. E., Pullen, A., Weber, M. E., Du, J., Larrasoaña, J., Zhang, J., Song, Y., González, F. J., Kaboth-Bahr, S., Li, H., Zhang, Q., Zhao, D., Cao, W., Zhao, M., and Liu, Q.: Enhanced phosphorus weathering contributed to Late Miocene cooling, Nat. Commun., 16, 1124, https://doi.org/10.1038/s41467-025-56477-7, 2025.